

**University of Alberta**

Fabrication of Large Area Resonator Arrays using Nanoimprint  
Lithography

by

Alexander Ryan Janzen

A thesis submitted to the Faculty of Graduate Studies and Research  
in partial fulfillment of the requirements for the degree of

Master of Science

in

Micro-Electromechanical Systems (MEMS) and Nanosystems

Department of Electrical and Computer Engineering

©Alexander Ryan Janzen

Fall 2011

Edmonton, Alberta

Permission is hereby granted to the University of Alberta Libraries to reproduce single copies of this thesis and to lend or sell such copies for private, scholarly or scientific research purposes only. Where the thesis is converted to, or otherwise made available in digital form, the University of Alberta will advise potential users of the thesis of these terms.

The author reserves all other publication and other rights in association with the copyright in the thesis and, except as herein before provided, neither the thesis nor any substantial portion thereof may be printed or otherwise reproduced in any material form whatsoever without the author's prior written permission.

*To Tom and Bev, for their encouragement and support*

# Abstract

This work investigates the use of nanoimprint lithography for creating nanoscale resonator devices for applications in mass sensing. A bilayer resist consisting of PMMA 495/LOR 3A allowed the ideal imprint yield for resonators with widths ranging from 300 nm down to 120 nm. Resonators with widths of 300 nm, lengths of 14  $\mu\text{m}$ , and thicknesses of 40 nm and 70 nm were fabricated with a yield approaching 100%. These devices were assayed, with resonant frequencies approaching 16.4 MHz and 21.6 MHz for the 40 and 70 nm thick devices respectively. Biotin-streptavidin was adsorbed onto the resonators, and the mass-per-area detected for the streptavidin protein was 0.78  $\text{mg}/\text{m}^2$  for the 40 nm thick beams, corresponding to 1 molecule per 128  $\text{nm}^2$ . The mass-per-area for the 70 nm thick beams was determined to be 3.57  $\text{mg}/\text{m}^2$ , corresponding to 1 protein per 21  $\text{nm}^2$ .

# Acknowledgements

I would like to thank my supervisor, Dr. Stéphane Evoy who introduced me to this project. He was very helpful over the course of the two years working here. I would also like to thank the staff at the Nanofab, particularly Scott Munro and Les Schowalter, for providing training and for helping me in my fabrication process. I want to thank everyone in Dr. Evoy's group for their kindness and expertise in the field of NEMS/MEMS, who helped me in all aspects of my project. In particular, I want to thank Csaba Guthy, Nathan Nelson-Fitzpatrick, and Nilufar Poshtiban for introducing me to the lab and for helping me with any particular problems I encountered. Their help and expertise were very valuable, and I am very appreciative for their patience and understanding. I wish to thank Amit Singh for introducing me to the world of chemistry and surface functionalization, and for answering any questions regarding my process. Finally, I want to thank all my friends for their continuing support during this project.

# Contents

<b>1</b>	<b>Introduction to MEMS/NEMS</b>	<b>1</b>
1.1	Beginnings of Nanotechnology . . . . .	1
1.2	Microelectromechanical Systems . . . . .	2
1.2.1	Microcantilever Devices . . . . .	2
1.3	Nanoelectromechanical Systems . . . . .	5
1.4	Need for Large Arrays . . . . .	7
1.5	Thesis Rationale . . . . .	9
1.5.1	Nanoimprint Process Parameters . . . . .	10
1.5.2	Resonance Measurements . . . . .	10
<b>2</b>	<b>Nanoimprint Lithography</b>	<b>12</b>
2.1	Introduction to Nanoimprint Lithography . . . . .	12
2.2	NIL Processes . . . . .	13
2.2.1	Thermal NIL . . . . .	13
2.2.2	UV NIL . . . . .	14
2.2.3	Roller NIL . . . . .	16
2.3	Imprint Stamp Production . . . . .	16

2.3.1	Materials for Stamp . . . . .	17
2.3.2	Lithography Processes for Stamp . . . . .	18
2.4	Structure Layout . . . . .	20
2.4.1	Structure Height . . . . .	20
2.4.2	Structure Density . . . . .	21
2.4.3	Anti-sticking Layer . . . . .	21
2.5	Process Parameters . . . . .	22
2.5.1	Polymer Resist . . . . .	23
2.5.2	Imprint Parameters . . . . .	24
2.6	Imprint Behaviour . . . . .	26
2.7	Summary . . . . .	27
<b>3</b>	<b>Nanomechanical Resonators</b>	<b>29</b>
3.1	Introduction . . . . .	29
3.2	Mass Detection Capabilities . . . . .	29
3.2.1	Magnetomotive Detection . . . . .	30
3.2.2	Piezoresistive Detection . . . . .	31
3.2.3	Interferometry . . . . .	32
3.3	Mass Sensing . . . . .	33
3.3.1	Mass Sensitivity . . . . .	34
3.3.2	Quality Factor . . . . .	37
3.4	Review of NEMS - Biosensing . . . . .	39
3.4.1	Chemical and Biological Sensing . . . . .	40
3.5	Summary . . . . .	41

<b>4</b>	<b>Nanomechanical Resonator Imprints</b>	<b>43</b>
4.1	Introduction . . . . .	43
4.2	Mask Fabrication for Imprinting . . . . .	44
4.2.1	Mask Degradation . . . . .	46
4.3	Resonator Imprint Process . . . . .	47
4.4	Experiments . . . . .	50
4.4.1	Bilayer Resist Imprints . . . . .	53
4.5	Sub-300 nm Wide Imprint Experiments . . . . .	57
4.6	Conclusions . . . . .	61
<b>5</b>	<b>Resonance Measurements</b>	<b>62</b>
5.1	Introduction . . . . .	62
5.2	Surface Functionalization . . . . .	63
5.2.1	Self-Assembled Monolayers . . . . .	64
5.2.2	Binding Agents . . . . .	66
5.3	Experiment . . . . .	66
5.4	Results . . . . .	68
5.4.1	Resonance of 40 nm Thick Beams . . . . .	68
5.4.2	Resonance of 70 nm Thick Beams . . . . .	72
5.4.3	Streptavidin Mass Measurements . . . . .	74
5.4.4	70 nm Thick Mass Measurements . . . . .	78
5.5	Multiple Experiments per Sample . . . . .	81
5.6	Conclusions . . . . .	83

<b>6</b>	<b>Conclusions</b>	<b>84</b>
6.1	Summary . . . . .	84
6.2	Recommended Work . . . . .	86
	<b>Bibliography</b>	<b>87</b>

# List of Tables

2.1	Glass transition temperatures for some common polymers. . .	13
2.2	Relationships between various imprint parameters. . . . .	23
3.1	Process Steps for PECVD SiCN Deposition . . . . .	30
5.1	Material Properties of Silicon Carbonitride . . . . .	70
5.2	Mass Sensitivity for 40 nm Thick Resonators . . . . .	76
5.3	Mass Sensitivity for 70 nm Thick Resonators . . . . .	79

# List of Figures

1.1	Basic configuration for an atomic force microscope. . . . .	3
2.1	Process used for thermal nanoimprint lithography. After the imprint is completed, there is always a small layer of resist left which needs to be etched away. . . . .	14
2.2	Process flow for UV nanoimprint lithography. . . . .	15
2.3	Pillar formation occurring due to nucleation sites on the substrate. Due to polymer displacement from the structures, the pillars did not form on top or near the imprinted resonators. .	26
2.4	Viscous fingering on the substrate, which is caused by rapidly expanding trapped air. . . . .	27
3.1	Schematic diagram showing a magnetomotive detection system.	31
3.2	Resonance spectrum for a 50 nm thick, 14 $\mu m$ long and 300 nm wide resonator. The Q factor is obtained by the peak resonant frequency divided by the bandwidth of the overall spectrum. .	38
4.1	Process flow for the fabrication of a silicon mask for NIL. . . .	45
4.2	A completed resonator pattern on the silicon mask, with a width of approximately 220 nm. . . . .	46
4.3	Structures on the imprint mask after over 6 months of use and several dozen imprints. Some of the devices become damaged, as shown on the image on the left, while others have resist sticking where the beams meet the anchor pads, as shown on the right image. . . . .	47

4.4	Process flow for the imprint and subsequent release of the resonator devices. . . . .	49
4.5	A completed resonator device which has been fabricated using nanoimprint lithography. This particular device has a width of approximately 300 nm. . . . .	50
4.6	Relative imprint yield for different substrates using different resists. Each bar represents separate imprints for each resist. The 300 nm thick PMMA 495/LOR 3A bilayer shows the greatest yield, with the mr-I 8030 E resist showing great yields as well. . . . .	51
4.7	Resonator imprints using PMMA 495 as the resist layer. The beam structures remained intact for the imprints, although the anchor pads do not retain their shape. . . . .	52
4.8	Comparison images between PMMA 495 imprints on the left, and imprints using PMMA 495/LOR 3A on the right. Both images were taken after the chrome deposition step during fabrication. . . . .	53
4.9	This is a released resonator created using the 300 nm thick bilayer resist of PMMA 495/LOR 3A. The resonators produced for this sample have a width between 300 nm and 320 nm. . . . .	54
4.10	Microscope images comparing the imprints of a thicker LOR 3A layer (left) with a thinner layer (right). . . . .	55
4.11	Resonator imprints using mr-I 8030 E as the resist layer. . . . .	57
4.12	This is a resonator used for the imprint mask to create devices with beam widths of less than 300 nm. This particular structure has a beam width of approximately 60 nm. . . . .	58
4.13	SEM images of the smallest resonator beam to be imprinted, with a width of approximately 120 nm. These images were taken after the chrome deposition step during fabrication. . . . .	58
4.14	These images compare the mr-I 8030 E resist imprints (top) with the corresponding mask devices (bottom). The imprinted structures were imaged after the chrome deposition step. . . . .	60
5.1	A generic diagram of a SAM molecule. The head group attaches itself to the substrate, while the functional group is attached to the binding agent for biodetection. . . . .	65

5.2	A diagram showing the process, from left to right, of functionalization of APTES to the surface, binding biotin to the monolayer, and the attachment of streptavidin to biotin. . . . .	67
5.3	Schematic diagram of the interferometry setup for resonance-assaying measurements. . . . .	68
5.4	The fundamental resonant frequencies for a number of resonators on two arrays are measured. These devices are 40 nm thick, 300 nm wide, and 14 $\mu\text{m}$ long. . . . .	69
5.5	The Q factor is calculated for 5 resonators on one array of a sample for the 40 nm thick resonators. . . . .	71
5.6	The resonant frequency for 70 nm thick beams are measured for an entire array of devices. These devices are 300 nm wide, and 14 $\mu\text{m}$ long. . . . .	73
5.7	The Q factor is calculated for several resonators on one array of a sample for the 70 nm thick resonators. . . . .	74
5.8	Frequency comparisons showing the differences between the bare SiCN resonators, functionalized surface, and streptavidin binding. . . . .	75
5.9	A graph showing the frequencies of the 40 nm thick resonators before and after adsorbing the streptavidin with blocked binding sites. . . . .	77
5.10	A plot showing the frequencies of 70 nm thick resonator devices before and after streptavidin adsorption. . . . .	78
5.11	Frequency spectra for the 70 nm thick (top) and 50 nm thick (bottom) resonators. . . . .	80
5.12	Frequency plot showing the positive, normal concentration exposure (top) and the controlled saturation exposure (bottom). . . . .	82

# List of Abbreviations

DNA	Deoxyribonucleic acid
EBL	Electron beam lithography
MEMS	Microelectromechanical systems
AFM	Atomic force microscopy
NEMS	Nanoelectromechanical systems
Da	Dalton, $1.6605 \times 10^{-27}$ kg
SiCN	Silicon carbonitride
GaAs	Germanium arsenide
PMMA	Polymethylmethacrylate
HSQ	Hydrogen silsesquioxane
DPN	Dip pen nanolithography
NIL	Nanoimprint lithography
LOR	Lift-off resist
KOH	Potassium hydroxide
LED	Light-emitting diode

DLC	Diamond-like carbon
UVL	Ultraviolet lithography
RIE	Reactive ion etching
MBE	Molecular beam epitaxy
PTFE	Polytetrafluoroethylene
SAM	Self-assembled monolayer
PMGI	Polydimethylglutarimide
PECVD	Plasma-enhanced chemical vapor deposition
sccm	Standard cubic centimetre per minute
RF	Radio frequency
EMF	Electromotive force
MESFET	Metal semiconductor field effect transistor
TED	Thermoelastic dissipation
MIBK	Methyl isobutyl ketone
IPA	Isopropyl alcohol
psi	Pound per square inch
SEM	Scanning electron microscope
QCM	Quartz crystal microbalance
SPR	Surface plasmon resonance
APTES	Aminopropyltriethoxy silane

---

---

# CHAPTER 1

---

## Introduction to MEMS/NEMS

### 1.1 Beginnings of Nanotechnology

The field of nanotechnology was first proposed to the scientific community at large when Richard Feynman gave a talk in 1959 titled “There is Plenty of Room at the Bottom” to the American Physics Society at Caltech (1). He outlined how the fields of physics, chemistry, and biology can greatly benefit from nanotechnology through better electron microscopes to observe the structures of DNA and other molecular compounds. He also discussed the possibilities of miniaturizing certain technologies like computers. He gave out examples of how to construct these small components, such as using electron beam microscopes to create small details on a substrate. He also discussed the potential uses of using light from an optical microscope to etch designs onto a substrate. This idea led to the optical lithography systems seen in laboratories today, which has some similarities to his initial idea. Technologies were soon developed to make these ideas from his talk come to fruition. This led to the first microelectromechanical systems (MEMS) that are now widely spread.

## 1.2 Microelectromechanical Systems

Microelectromechanical systems, or MEMS, refers to any device or groups of devices which can perform functions within an area of less than  $1 \text{ mm}^2$ . MEMS generally involve both electronic and non-electronic components which are capable of performing many different functions, such as signal processing or acquisition (sensing), displays, and control (2). These devices work together, or are integrated, onto a common substrate which is usually made of silicon. The most common applications for MEMS include integrated circuits in computers, accelerometers in automobiles, and cell phones, to name a few. MEMS devices can also be categorized as sensors or actuators. Sensing microdevices consist of one or more elements which can detect an external stimulus such as pressure or acceleration. This stimulus is converted into an electrical signal for processing to extract additional information. Actuating devices take an electrical stimulus and translates it into a mechanical force for movement, such as manipulation or transporting materials. MEMS have recently been used in devices which do not include moving parts. Some examples include thermal, magnetic, and optical devices (2).

MEMS have since moved from the developmental research stage to the marketplace, with many devices now available for commercialization. More devices can be fabricated at a decreased cost due to advancements in fabrication techniques. These devices include accelerometers for vehicles, such as the ADXL312 accelerometer designed by Analog Devices (3). Other devices which have become commercially viable include pressure sensors (4; 5) and temperature sensors (6). These devices demonstrate the versatility of MEMS and how they can be used for a multitude of purposes.

### 1.2.1 Microcantilever Devices

We have mentioned earlier that one of the most important uses for MEMS is sensing. Very fine measurements can be made with pinpoint precision due to

the small scale nature of MEMS devices. One such device which makes use of this fact is the microcantilever. One of the first microcantilever devices used was for atomic force microscopy (AFM) (7). AFM is a type of scanning probe microscopy which is able to measure samples with very high resolution. It is capable of measuring the surface of a sample on the nanoscale by using a microcantilever, called the probe. The microcantilever has a sharp tip on its point, which is usually made of silicon. The cantilever is brought into close proximity with the sample surface. This causes the cantilever to be deflected by atomic forces acting between the tip and the sample. This kind of imaging is called contact mode, which is one of the modes of operation for the AFM. This deflection is measured by a laser shining onto the cantilever. The reflected light is collected into an array of photodiodes which measures the amount of deflection on the cantilever as seen in Figure 1.1 (8). This information then provides us with the surface topography of the sample.

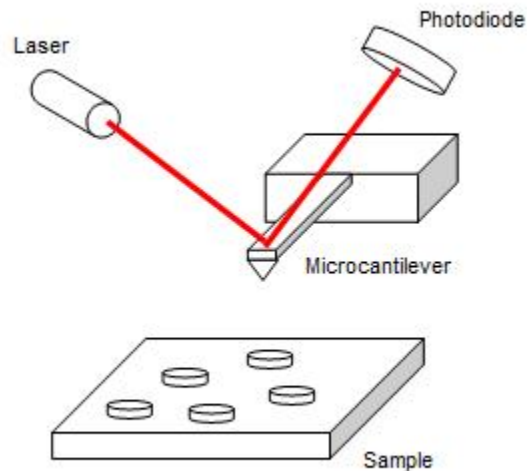


Figure 1.1: Basic configuration for an atomic force microscope.

There are two other modes of imaging for use by the AFM other than contact

mode. One mode is called non-contact AFM imaging. The cantilever tip for this mode of imaging does not interact with the surface of the sample. The tip oscillates at some frequency several nanometres above the sample. This oscillation is only slightly higher than its normal resonant frequency, resulting in an amplitude of oscillation of less than 10 nm. The frequency is modified by interactions which occur at the tip-surface boundary. This frequency shift is used to create an image of the surface. Non-contact mode is useful when measuring soft samples, or samples with an adsorbed layer of liquid which can't be measured by traditional contact mode imaging (9). Van der Waals forces or any other attractive forces interact with the cantilever near the surface of the sample to slightly decrease the resonant frequency of the cantilever. The resonant frequency of the cantilever is governed by Hooke's law, where the natural frequency of the cantilever is shown in Equation 1.1:

$$f = \frac{1}{2\pi} \sqrt{\frac{k}{m^*}} \quad (1.1)$$

where  $f$  is the frequency of the cantilever,  $k$  is the spring constant, and  $m^*$  is the effective mass of the cantilever or oscillator. A change in load on the cantilever occurs when the attractive atomic forces act upon the oscillator during non-contact mode. This will cause the resonant frequency of the device to shift, which is then detected by the laser and photodiode setup. The approximate distance between the cantilever tip and the sample can be calculated giving a map of the topography of the surface.

The third imaging mode for the AFM is called tapping mode. The cantilever is driven to oscillate at its resonant frequency usually by a piezoelectric element, much like non-contact mode. The amplitude of oscillation in this mode is usually greater than 100 nm, rather than the sub-10 nm amplitude for non-contact mode. A variety of forces will act upon the cantilever when it approaches the surface. Some of these forces include van der Waals or electrostatic forces. This will cause the amplitude of oscillation to decline which will decrease the resonant frequency of the cantilever (10). This method of imaging ensures

that the cantilever tip will not become lodged on the sample, decreasing the risk of damage to the tip. This method is preferable from non-contact mode when imaging a sample which has a liquid meniscus layer. The tip will not become stuck due to the lower amplitude oscillations and the layer will not be disrupted and deformed (11).

The usefulness of the cantilever can also be applied elsewhere. The resonant frequency of the cantilever will decrease whenever extra mass is added onto the oscillator. This means that cantilevers or any other oscillating device can be used for mass sensing purposes. These sensors are able to detect various chemical or biological compounds with very small masses. It is possible to attach or attract various materials to the surface of the oscillator by adding surface treatments to the surface. This will allow the oscillator to measure shifts in resonant frequency. Cantilevers can be made from several different materials such as silicon (12) and silicon nitride (13). Arrays of cantilevers can be fabricated with each array detecting different biological or chemical agents. The applications of these types of oscillators are robust, such as explosives detection (14) or for diagnosing diseases for lab-on-a-chip technologies (15).

### 1.3 Nanoelectromechanical Systems

Microcantilevers are able to interact with and detect masses of very small materials on the molecular scale. However, if one were to decrease the dimensions of the oscillator, would it be possible to detect even smaller masses such as viruses or individual atoms? Microcantilevers are perfectly capable of detecting the masses of certain biological and chemical agents like bacteria (16). Ilic *et al.* showed that microcantilevers are able to achieve femtogram ( $10^{-15}$  g) sensitivity (17). This shows that microcantilevers are perfectly able to detect any kind of bacterium since bacteria weigh up to hundreds of femtograms. Microcantilevers are not sensitive enough to detect smaller masses such as viruses which have magnitudes smaller than a typical bacterium. A typical virus has a mass of a few hundred attograms ( $10^{-18}$  g). The detection

of pathogens would be extremely beneficial to determine if a certain harmful virus is within the environment.

Nanoelectromechanical systems, or NEMS, are capable of a much greater degree of sensitivity than MEMS. NEMS are an offshoot of MEMS, with the dimensions approaching several nanometers, instead of several micrometers. This significant decrease in dimensions can allow for greater sensitivity to masses, allowing for detection into the attogram and zeptogram ( $10^{-21}$  g) regime. While NEMS is still in the developmental and research stage, it has already been shown by Ekinici *et al.* that attogram sensitivity is possible by adsorbing gold atoms onto a nanomechanical resonator (18). Proteins have also been detected within the femtogram range by Fischer *et al.* using nanomechanical resonators (19). Zeptogram resolution has also been achieved, down to about 7 zg by Yang *et al.* (20). It will be possible to achieve single Dalton sensitivity ( $1 \text{ Da} = 1.6605 \times 10^{-27} \text{ kg}$ ) with further advancements in sensing technology. This has been theorized to be the ultimate limit to mass sensitivity (21).

There are various possible materials which can be used to achieve the highest possible mass sensitivity for nanomechanical oscillators. NEMS can be fabricated using thin films which can provide different fabrication opportunities. This will also allow for more studies into the effects of different materials for their use as mass sensors. Some of these materials include silicon nitride (22), silicon carbide (23), as well as nanocrystalline diamond thin films (24). These materials each have their own advantages and disadvantages for mass sensing. One material which has been demonstrated to yield narrow beams and is able to detect very small masses is silicon carbonitride (SiCN). This material has many advantages over others used for nanomechanical resonators. One example of a material which has been used for MEMS repeatedly is silicon. Silicon is a well-understood material and it has been studied in depth for strength distributions for MEMS (25). There are some problems with using this material for nanoscale oscillating devices. Carr *et al.* have been able to fabricate silicon resonators at widths of approximately 45 nm (26). The yield for these

devices was very low at lengths exceeding more than a few micrometers (27). Resonators which have been fabricated using silicon oxide are susceptible to cracking due to moisture (28; 29; 30). It has been shown by Sekaric *et al.* that a high yield of about 98% has been achieved for nanomechanical resonators with widths approaching 50 nm using silicon nitride (31). Fischer *et al.* developed silicon carbonitride which allows for lower intrinsic stresses than other materials (32). SiCN has also been shown to be easy to deposit using PECVD (plasma enhanced chemical vapor deposition) (33). It was for this reason that SiCN was chosen for the devices created in this thesis.

## 1.4 Need for Large Arrays

There must be fabrication facilities capable of producing dozens or hundreds of NEMS devices easily and affordably for them to be readily commercialized. It is much more time consuming and expensive to produce the devices needed due to the small feature sizes necessary. The best way to produce NEMS currently is by electron beam lithography, or EBL. This method of lithography involves scanning a beam of electrons in a pattern controlled by a computer over a substrate covered in photoresist. The exposed photoresist is then developed, revealing the pattern on the substrate. EBL is capable of very small linewidths depending upon the substrate and resist used. Craighead *et al.* produced 10 nm linewidths on a single layer of polymethylmethacrylate (PMMA) on a GaAs substrate (34). Baek *et al.* recently used hydrogen silsesquioxane (HSQ) photoresist to achieve sub-10 nm feature sizes (35). These feature sizes make it ideal for using EBL to produce nanomechanical oscillators with thin widths which can allow for higher mass sensitivities.

EBL is not ideal for mass production of nanoscale devices. The equipment needed for EBL is very expensive, reaching into the millions of dollars for commercial applications. Most of the systems today only allow one substrate to be exposed by the system at a time. This makes the process very slow if hundreds of substrates are needed. The time it takes for one substrate to be

scanned is approximately three hours or more depending upon the complexity of the pattern. There are some systems using multi-column EBL allowing for a much higher throughput. Systems such as these are currently under development by Multibeam Corporation (36). The cost of these systems will be in the millions of dollars, with maintenance costs high as well.

Another option for production of NEMS is dip pen nanolithography, or DPN. This method of lithography involves transporting a chemically reactive material such as alkanethiols or silanes from an AFM cantilever tip to a substrate (37). The cantilever tip drags over the surface of the substrate, and the material transfers from the tip to the substrate via a water meniscus which forms between the tip and the substrate. It is possible to write features as small as 10 nm which makes it ideal for producing nanomechanical resonators. There have been some advances using DPN allowing for parallel patterning so that multiple substrates can be patterned at the same time (38). This technique can be very powerful to use for mass production. It can become quite expensive as well as time consuming because each pattern needs to be drawn out instead of printing the pattern all at once.

One other lithography technique which can allow for the desired pattern to be printed all at once is nanoimprint lithography, or NIL. This technique involves pressing two substrates together; one substrate contains the desired structures to be imprinted (mask), and the other substrate is coated with a photoresist. The features from the mask substrate are copied onto the resist-coated substrate when the two substrates are pressed together under heat and high pressure (39). A metal deposition process and subsequent resist liftoff follows which will make the mask and imprint substrates identical to one another. It is possible to imprint feature sizes down to approximately 10 nm, with the potential to go even lower (40). The primary advantage that this method of fabrication has over the other methods is that it takes a very short amount of time to perform each imprint. It is possible to do an imprint in as little as ten minutes instead of several hours for EBL. This means that it is very feasible to use NIL for mass production purposes. The

costs for using NIL are substantially reduced to approximately several hundred thousand dollars since the system does not need high-energy radiation sources or optical components. This makes NIL economically feasible compared to the multi-million dollar systems used for EBL. The only disadvantage of this technology is that a separate fabrication process such as EBL is necessary to produce the mask needed for imprinting. Only one mask is needed in order to produce potentially hundreds of substrates identical to the mask.

NIL has already been put into use for creating NEMS like cantilever arrays (41) and resonator devices (42) with widths as small as 80 nm. The ability for NIL to imprint feature sizes as small as 10 nm (43) in a very short amount of time compared with other fabrication techniques presents a great opportunity to mass produce these sensing devices. NIL is currently being primarily used for research purposes. It will be possible eventually to use this fabrication technique for commercial applications.

## 1.5 Thesis Rationale

This project will explore the possibilities of using nanoimprint lithography to produce large arrays of resonator devices made of silicon carbonitride to determine if mass production capabilities are possible. We will explore the various parameters used to ensure high imprint yields, such as resists used, imprint temperatures and times, and the lift-off process of the resist. The testing of the devices after imprinting will also be explored, showing how well the devices worked and their mass sensitivities compared with those devices in literature. A proof-of-concept sensor is also explored which involves multiple experiments being performed upon individual arrays on a single 1 cm<sup>2</sup> sample instead of one experiment per sample.

### 1.5.1 Nanoimprint Process Parameters

There are various kinds of resists such as PMMA and HSQ which can be used in nanoimprint lithography. Various resists have been used for this project to determine which resists will have the desired effects and give the best imprint yields. The resists used ranged from SU 8, PMMA, and lift-off resist (LOR), as well as combinations of PMMA/LOR in varying concentrations. It was found that a bilayer resist of PMMA/LOR 3A gave the best imprint yields for specific widths of resonators. Various other parameters were also experimented with on the imprint process itself, such as the imprint temperature, pressure, and time. Varying any of these parameters will affect the results of the imprints. Better resolution on feature sizes is achieved by increasing the length of time during imprinting and very little imprinting occurred when the temperature was lowered during the imprint process.

It was found after imprinting that there was a small layer of resist remaining where the structures from the mask imprinted onto the substrate. This resulted in further experimentation to find the best way to remove this layer of resist without widening any of the feature sizes. A quick isotropic plasma etch was found to work for structures with feature sizes as large as 300 nm. It was found that resonator beams with widths smaller than 100 nm widened significantly, up to 100 nm or more. Other etch possibilities were explored, like wet etches for bilayer resists where the top layer was removed using a plasma etch and the bottom layer was removed with a developer.

### 1.5.2 Resonance Measurements

The imprinted resonators were released using a potassium hydroxide (KOH) etch. These released resonators were measured using an interferometry setup to determine the resonance frequencies for the imprinted devices. The resonators were functionalized with biotin and measured again. The biotin is used for binding of certain biomaterials such as streptavidin. Streptavidin was

used for this project due to its high binding affinity to biotin. There was a decrease in resonance frequency after the biotin was adsorbed onto the resonators. Streptavidin was then adsorbed to the biotin, and the devices were measured again. It was found that there was a decrease in resonance frequency, and from this change in frequency, it was possible to determine the mass sensitivity of the imprinted resonators. It was confirmed experimentally that the change in frequency is due to the streptavidin binding to the resonator devices instead of from non-specific adsorption.

---

---

## CHAPTER 2

---

### Nanoimprint Lithography

#### 2.1 Introduction to Nanoimprint Lithography

Nanoimprint lithography, or NIL, is a relatively new fabrication process to produce nanoscale devices. The first use of NIL started in 1995 by Stephen Chou *et al.* (44). They successfully managed to imprint dots and lines with a minimum feature size of 25 nm. There are now numerous groups that are using NIL for their fabrication processes. The minimum feature sizes of imprints has been reduced to below 10 nm (40; 45). These groups use different kinds of NIL to fabricate their devices, with each process having their own benefits. The two most common processes are thermal NIL and ultraviolet light (UV) NIL. Thermal NIL uses heat and pressure to imprint the devices while UV NIL uses a UV light to expose the resist on the substrate while under pressure. There is another process called roller NIL which involves a rolling cylinder with the imprint mask surrounding it to imprint the substrates which roll underneath it. The process used for this thesis is thermal NIL.

## 2.2 NIL Processes

### 2.2.1 Thermal NIL

Thermal nanoimprint lithography is the most common form of NIL. This process involves pressing the imprint mask into the resist-coated substrate at high temperature and pressures at 200 psi or higher. A diagram which shows this process is shown in Figure 2.1. The temperature must be higher than the glass transition temperature ( $T_g$ ) of the photoresist. This is the temperature at which the resist will begin to flow. The resist will flow around the structures on the imprint mask when the photoresist is under pressure at temperatures higher than  $T_g$ . Table 2.1 shows the approximate values of  $T_g$  for some common resists. The resist hardens as the temperature cools while a high pressure is maintained until a temperature setpoint is reached. This setpoint is usually between 40°C and 50°C (46). The two substrates are separated from one another after the pressure is released to reveal the newly imprinted structures. The polymer resist which is primarily used for this thesis is PMMA due to its low value of  $T_g$  of approximately 105°C. Variations of this temperature occur depending upon the molecular weight of the resist (39). It is beneficial to use polymers with a low viscosity to ensure that the resist will flow. Resists with lower viscosity will also lower the glass transition temperature, making it easier and faster to complete the imprint process (47).

There are many examples of thermal NIL which have worked for very small

Table 2.1: Glass transition temperatures for some common polymers.

<b>Polymer</b>	<b><math>T_g</math> (°C)</b>
Polystyrene	100
PMMA 495/950	95 - 106
PMGI/LOR	190
SU 8	230

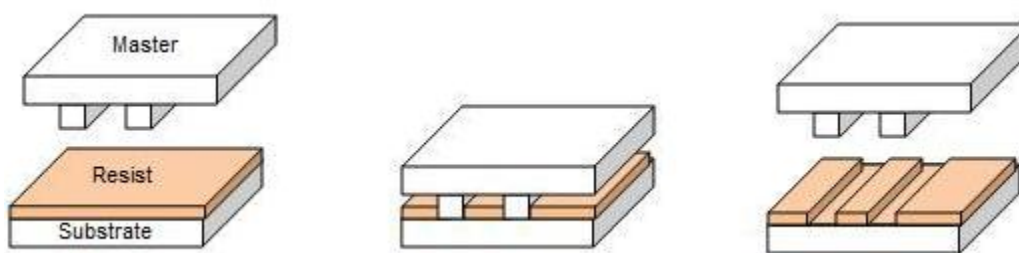


Figure 2.1: Process used for thermal nanoimprint lithography. After the imprint is completed, there is always a small layer of resist left which needs to be etched away.

feature sizes. Gourgo and Chaix *et al.* used thermal NIL to produce 50 nm feature sizes using a silicon stamp using various types of resists (48). MEMS devices have also been fabricated using thermal NIL. GuoYong *et al.* have produced suspended structures such as cantilevers and resonators with widths as low as 200 nm (49). There are also biological applications for thermal NIL, such as nerve guiding to control the growth of neurons along set paths. Carlberg *et al.* used NIL to fabricate the channels needed for this process using a silicon stamp and PMMA for the resist-coated substrate (50). The reason why thermal NIL is primarily used is due to the wide range of polymer resists available with low  $T_g$ . There are also a large variety of materials which can be used for the mask. The only disadvantage with this process is that the time it takes to imprint is a little longer than other nanoimprint processes like UV NIL (50).

### 2.2.2 UV NIL

UV NIL is a process which is similar to that of thermal NIL, except an ultraviolet light source is applied to the stamp rather than heat while under high pressures. The polymers chosen for imprinting can be the same ones used for thermal NIL. The UV light will initiate cross-polymerization of the photoresist once the mask comes into contact with the imprint substrate. The

cross-polymerization allows the resist to retain its shape after separation. This process is shown in Figure 2.2.

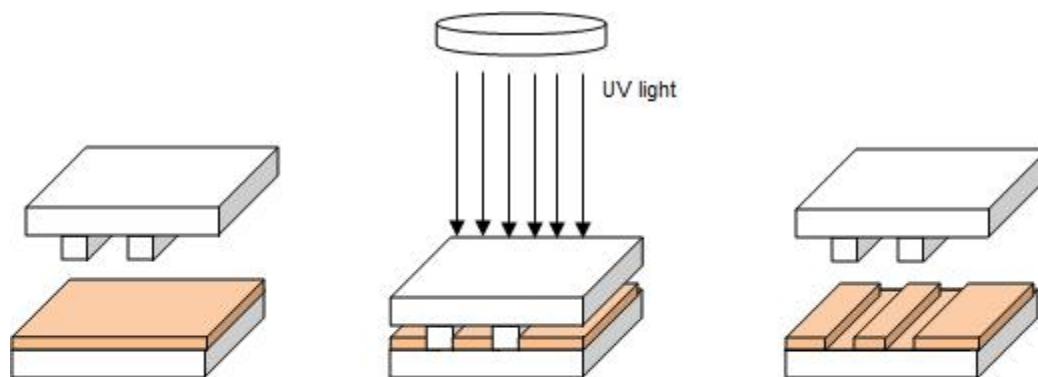


Figure 2.2: Process flow for UV nanoimprint lithography.

The major drawbacks with using UV NIL is that the imprint mask must be transparent to UV light. This means that there are limited materials which can be used to make the mask. The resist used for imprinting must also have a low viscosity to ensure that the resist will flow around the structures on the mask once exposed to UV light (50). There are some advantages of UV NIL over thermal NIL which include high throughput and greater resolution. It is possible to get higher accuracy in shape transfer from the mask to the substrate since there is no thermal cycle required for this process (51). The time required to do each imprint is reduced which allows for a higher throughput than thermal NIL.

There are a large variety of nanoscale structures which can be produced using UV NIL. Some examples of such devices include magnetic dots and light emitting diodes (LEDs) (51). Gilles *et al.* has demonstrated that it is possible to achieve sub 100 nm resolution using UV NIL (52). UV NIL is primarily being used for research purposes with most publications being largely on the development and future prospects of using UV NIL (53; 54).

### 2.2.3 Roller NIL

Roller NIL is the last form of nanoimprint lithography we will discuss. This process can involve bending the imprint mask into a cylindrical shape and attaching it to a metal tube (55). Alternatively, the imprint mask can also lie flat on the sample allowing the roller to press down on both substrates. For either method involved, the roller rotates around a fixed axis while a platform containing the sample slides underneath the roller. The temperature of the roller is set higher than the  $T_g$  of the polymer while the temperature of the platform is below  $T_g$ . This ensures that only the area in contact with the sample is heated above  $T_g$ , rather than the entire sample simultaneously being heated to  $T_g$  for conventional thermal NIL.

There are also designs which involve using a UV source to cure the resist which makes the process more similar to UV NIL (56). The polymers used for this technique must have a low viscosity to deform under high pressures while remaining at room temperature. The UV will cross-link the resist ensuring that the resist will remain in its position after imprinting. The main advantage for this technique is that it is possible to have a very high throughput and still be able to get feature sizes below 100 nm (55). This method of nanoimprint lithography is primarily being used for research purposes.

## 2.3 Imprint Stamp Production

The imprint stamp is the most important consideration for nanoimprint lithography. There are three important factors to consider when producing the stamp for imprinting. These factors include the materials which make the stamp, the lithographic processes to produce the structures on the stamp, and the anti-sticking layer to ensure that no photoresist will remain on the stamp once it is removed from the sample.

### 2.3.1 Materials for Stamp

The most commonly used material to produce the stamp is silicon. Silicon is inexpensive, widely available and it can work well for almost any patterning method. Silicon has a high conductivity which makes it the best material to use when patterning with electron beam lithography. The dry etching processes for silicon are also well known and developed. This makes processing very simple for the imprint mask when using silicon. The only major disadvantage is potential surface roughness when using deep silicon etching (50).

Another common material for use as an imprint mask is silicon dioxide ( $\text{SiO}_2$ ). A layer of  $\text{SiO}_2$  is deposited upon pure silicon wafers to create the base of the mask. Silicon dioxide has been observed to have nearly identical properties to silicon (50). This makes patterning the mask very simple since the process parameters will be similar to that used for silicon.  $\text{SiO}_2$  is a good candidate for UV NIL since it is relatively easy to use for optical alignment and it is transparent (57). Polymers can also be used for nanoimprint stamps. These polymers are usually negative photoresists. EBL or ultraviolet lithography is usually used for initial cross-polymerization. The polymer is fully cross-polymerized after a heat treatment and can then be developed. The resist which was not exposed to the EBL or UV process will wash away to leave the cross-linked polymer structures behind. One disadvantage of patterning negative photoresists is that the resolution is much lower than that of positive photoresists. This means that the minimum feature sizes one can get with negative resists will be much higher. It was shown by Pfeiffer *et al.* that it is possible to get patterns with feature sizes as small as 70 nm by using an e-beam sensitive photoresist called mr L 6000 XP (58).

There are some other materials which can be used as nanoimprint masks. Nickel has previously been used successfully for imprint stamps, however there must be a different anti-sticking layer used than those used for silicon stamps (59). This is due to the lack of an oxide layer which is normally present on silicon substrates. Other options used for UV NIL include diamond-like carbon

(DLC) films deposited onto  $\text{SiO}_2$  templates (60). These films also serve as an anti-sticking layer, which can be more effective than traditional chemistries used for silicon stamps. Stamps can also be made directly out of DLC which can be a benefit for alignment and mass production purposes due to its high hardness (61).

### 2.3.2 Lithography Processes for Stamp

The next step after selecting the material to use is to create the structures needed for imprinting. The usual method of choice is electron beam lithography because of its high precision and its ability to produce complex patterns. EBL involves using an electron beam directed onto a photo-sensitive resist to create patterns. Some common resists used for EBL include PMMA and HSQ. The electrons which interact with the resist break the bonds within the polymer chain, enabling it to be removed using a developer. A metal is then deposited after development to create the devices. It is possible to produce structures with very small feature sizes as small as 20 nm or under (62; 35). The size of the substrate when using EBL can vary from small chips of about 1  $\text{cm}^2$  to wafers 6 inches in diameter or larger. The size of the sample being used depends upon the system specifications. The only disadvantage with EBL is that it can take a long time to produce the desired structures, particularly if the pattern being exposed is complicated. Only one mask is needed to produce hundreds of imprints. The resulting imprints can also be used again for a substitute mask if needed.

Another process which can be used to produce masks for nanoimprinting is optical lithography, otherwise known as ultraviolet lithography (UVL). This process involves shining a UV light through a patterned mask usually made out of fused silica ( $\text{SiO}_2$ ) to expose resist on a substrate directly underneath the mask. This method of UVL is called contact photolithography. The exposed resist becomes cross-linked and can be developed leaving the desired pattern upon the substrate. This process is very fast with a typical expo-

sure on the order of around 10 seconds or less. The patterned mask must be made in a mask writer on a transparent substrate which can take several hours to produce. The resulting feature sizes on the pattern are much larger than those developed using EBL. The lowest resolution achievable using conventional UVL is less than 500 nm using i-line light from a mercury lamp, which has a wavelength of 365 nm (63). Another form of UVL called extreme ultraviolet lithography (EVL) can work using wavelengths of 13.4 nm (64). It is possible to achieve feature sizes of approximately 32 nm or less using this technique (65). UVL is a great way to create imprint stamps due to the high throughput of the system. The only disadvantage is that the limits of resolution prevent any small structures from appearing on the mask.

There are a number of other lithographic processes which can also be used to create the stamp for NIL. Some of these processes include AFM lithography. This is a process which involves applying a voltage between the cantilever tip and the surface of the substrate, which can induce oxidation (50). The resulting patterned silicon dioxide can then be used for stamping in NIL. This process is very slow and only conductive substrates can be used, although the resolution can go low as approximately 10 nm (50). Other lithographic processes include nanosphere lithography for fabricating large-area stamps. This process involves self-assembly using polystyrene nanobeads followed by reactive ion etching (RIE) to get the correct size for the beads to form the structures (66). This process can only create nanopillar structures in various formations. It has been shown by Kuo *et al.* that sub-50 nm structures can be obtained using this technique (67). Molecular beam epitaxy (MBE) can also be used in an unconventional method to create imprint masks with very small feature sizes. Austin *et al.* used MBE to create masks with 6 nm half-pitch lines for use in NIL by growing GaAs/Al<sub>0.7</sub>Ga<sub>0.3</sub>As superlattices on a GaAs substrate. A wet etch is used on parts of the superlattice to create periodic gratings (68).

## 2.4 Structure Layout

The patterned structures on the stamp must be laid out in a way to optimize polymer flow during the imprint process. The separation between the structures will alter the way the resist flows around them. Structures that are too close together will not allow enough room for the polymer to flow resulting in a partial or failed imprint. There are several factors which can affect the polymer flow during the imprint process. The most important factors include the structure height, the density of the structures, and the anti-sticking layer on the stamp.

### 2.4.1 Structure Height

The structure height on the mask will vary according to the applications needed for the imprint. The height of the structures can be as low as several nanometers (68) and as high as several micrometers. The structure height on the mask must be taken into consideration when compared with the height of the polymer resist during the imprint process. The ratio of structure height to polymer height will affect the polymer flow during imprinting. This can affect the probability of a good imprint yield. There will be very few polymer flow related problems when the structure height is less than the height of the polymer. This allows for a large amount of space between the substrates so that the polymer will flow around the structures. There will be some issues related to polymer flow when the structure height is roughly equal to the height of the resist. These defects take the form of capillary bridges between the stamp and the imprint sample (69). This kind of defect can lead to resist peeling away from the substrate and onto the stamp. Formations of resist may also be left behind which can affect the imprint yield.

There are also some defects which can arise if the structure height is much higher than the resist height. This is due to the limited amount of room for the polymer to flow around the structures. It then is best if the structure

height to be less than the resist height to ensure that there are no polymer flow problems. The structure height used in this thesis was approximately equal to the resist height. This did lead to some problems on the substrate such as deformations or pillar formations due to polymer flow, although the devices for the most part remained unaffected.

### 2.4.2 Structure Density

Another important factor when creating the stamp is the pattern density and area of structures. It is more difficult to imprint large areas like contact pads due to the amount of resist which must be displaced. Stamps with a high density of structures must use a resist with a low enough viscosity to ensure the polymer will flow around the structures evenly. The viscosity of the resist is regulated by the temperature during imprint, the pressure being applied, and by the molecular weight of the resist being used. Lowering the molecular weight of the resist will lower the viscosity, so the resist must be carefully chosen to ensure good polymer flow. The imprint time used for dense structures is important to ensure homogenous flow around all the structures to get a uniform pattern (70). Homogenous flow ensures that the residual resist layer remaining after imprinting will be uniform everywhere making the removal of this layer easier.

### 2.4.3 Anti-sticking Layer

There must be an anti-sticking layer deposited on top of the mask once fabrication is complete. This will ensure that none of the resist will peel off the imprint substrate and stick to the mask which can ruin the resulting imprint. The mechanisms of the polymers sticking to the imprint mask are well-understood (71). The polymer bonds are primarily due to physical adhesion and chemical bonding between the stamp and the polymer. There are many different kinds of anti-sticking layers which can be used. Examples include teflon-like layers

like polytetrafluoroethylene (PTFE) (71) and silane materials (39). This layer must be hydrophobic to repel any resist which may peel off the substrate, thus ensuring the stamp will remain clean.

The most commonly used anti-sticking layers are self assembled monolayers (SAMs). There are a number of well-developed processes which can be used for silicon stamps. The SAM which is used for this thesis is tridecafluoro-(1,1,2,2)-tetrahydrooctyl trichlorosilane (F13-TCS). This material is deposited via vapor phase deposition under a vacuum for approximately 30 minutes. Silanes are very effective to use and there is minimal rip-off occurring after SAM deposition. Any resist which has been ripped off and deposited on the stamp will be re-deposited on to the imprint substrate on a subsequent imprint. This demonstrates a self-cleaning property of the thermal imprint process (72).

## 2.5 Process Parameters

The next important step of NIL after the imprint mask is fabricated is choosing the various process parameters to ensure a successful imprint. The most important parameter to choose is the resist to use for the imprint substrate. The resist must have a low viscosity to ensure that the polymer will flow well around all the structures, so a low molecular weight is desired. Other process parameters which will affect the imprint process are the imprint temperature, imprint time and the pressure used during thermal imprint. The temperature must be higher than the glass transition temperature of the resist to ensure a low viscosity. The imprint time needs to be long enough to ensure that enough resist is displaced to ensure a smooth imprint with good yield and minimal defects. The pressure being applied will also affect the polymer flow. The amount of pressure used is primarily determined by the viscosity of the resist being used. All of these parameters will also affect how the other parameters perform. Lowering the viscosity will mean the imprint time should be longer to reduce defects and ensure the polymer will flow evenly around the structures. Table 2.2 shows the relationships between these parameters, and they

will be discussed further on in this chapter.

Table 2.2: Relationships between various imprint parameters.

Viscosity	Structure Density	Temperature	Pressure	Imprint Time
High	Low density and area needed	Temperatures much greater than $T_g$	High pressures	Long imprint times
Low	High densities and areas can be imprinted	Temperatures only slightly higher than $T_g$	Lower pressures possible	Lower imprint times

### 2.5.1 Polymer Resist

The polymer resist for the imprinting process is used to create the structures by deformation caused by heat and pressure. There are some important properties to consider when choosing the resist layer to be used, such as viscosity, film uniformity, adhesion to the substrate, and etch resistance. The viscosity of the resist must be low to ensure good polymer flow when the temperature is higher than the glass transition temperature of the resist. Resists with low molecular weight are therefore needed to ensure good flow. There are numerous types of resists which can be used for the imprint process like PMMA and lift-off resist (LOR). There are also certain resists which have been specifically designed for use in nanoimprint lithography.

The most commonly used resist for NIL is PMMA (polymethylmethacrylate). This resist has a low glass transition temperature of about  $105^\circ\text{C}$ . The  $T_g$  does vary depending upon the molecular weight of the resist (73). This resist has well developed process parameters and it is easy to use. The main disadvantage with using PMMA is that it becomes more resistant to solvents after using an oxygen plasma to etch the residual layer of resist away (74). PMMA is therefore usually used in bilayer imprint processes. Other resists which are

not affected by etching are deposited on the bottom layer to ensure that the resist will be removed more readily.

Another resist which is frequently used in NIL is LOR resists. This resist is a derivative of PMGI (polydimethylglutarimide), and it has a  $T_g$  of about 180°C. Imprints using LOR-based resists are typically carried above 200°C. This resist is usually used for bilayer imprints where PMMA is the top layer of resist (75). Bilayer resists can be extremely useful for nanoimprint lithography as this technique can reduce the need for using an oxygen plasma etch to remove the residual layer (75). The bottom layer resist can be etched using solvents that will not affect the top layer. There are many groups who have used bilayer resists for their processes. Buyukserin *et al.* used a bilayer resist to create polymeric nanorods for uses in biological applications like biomolecular sensing and therapeutic drug delivery (76).

There are also specific resists which have been designed to work for nanoimprint lithography. One such example is the mr-I 8000/9000 series by Microresist Technology (77). These resists have good film uniformity and better plasma etch resistance than other resists such as PMMA. They are also able to achieve feature sizes of sub-50 nm depending upon the stamp resolution being used. The mr-I 8000 polymers will also leave a lower residual layer thickness. This means that the etch time to remove this layer will be drastically reduced.

## 2.5.2 Imprint Parameters

Other factors which influence the imprint yield and can help to reduce the amount of defects are the parameters which are defined by the nanoimprinting system itself. These parameters include the temperature, duration of the imprint, and the pressure applied. The imprint temperature depends upon the type of resist being used since the imprint will not succeed below the glass transition temperature of the resist. The temperature must be at least 70°C above the accepted value of  $T_g$  for the resist being imprinted (78). Increasing the temperature will lower the viscosity of the resist. This will result in

better polymer flow around the structures. Thermal expansion should also be considered when choosing the imprint temperature, but only if the stamp and substrate materials are different from one another (50).

The imprint time and pressure is also determined by the viscosity of the patterning media. Polymer resists with a low viscosity will require less time and less pressure to get a good imprint. Longer imprint times may be required in order to reduce the number of defects that may arise due to the polymer flow. The imprint time should be higher if the structures are highly dense to ensure even polymer flow around all the structures. The pressure being applied is usually much higher than atmospheric pressures. Bender *et al.* has created imprints with sub-atmospheric pressures at 0.8 bar using specially designed resists (79). Typical pressures for imprinting are usually between 200 and 300 psi. Higher pressures are usually used for structures with high density or large areas to ensure good, even polymer flow. It is important that the pressure being applied is evenly distributed over the entire substrate or else a partial imprint will occur (50).

There is always a thin residual layer of resist left behind after imprinting which must be etched through to ensure that the patterns are transferred to the substrate. This etch is usually done using an oxygen plasma. The etch must be optimized for each resist to ensure that only the residual layer is removed. Low pressures and high bias voltages must be used to ensure that there are high quality definitions on the substrate (80). An isotropic or an anisotropic etch can be used depending upon the applications for the devices. An anisotropic etch would ideally be used for any devices with small feature sizes. This will ensure that the widths of the structures will remain consistently close to the widths of the structure on the mask. An isotropic etch is used for this thesis, although the pressures being used are low enough to ensure that any line-widening which occurs is kept to a minimum.

## 2.6 Imprint Behaviour

There is a very strong likelihood that patterns will appear in the resist during the imprint process. The patterns formed are a result of the flow of the resist around the structures. The evolution of the polymer during the imprint process is well-documented (81). These patterns can take the form of pillars, fractal-like patterns, and viscous fingering (39). These patterns have been studied before with possible explanations to their occurrence (46; 82; 83).

The formation of pillars is due to a charged mask being brought in close proximity to the polymer film. There are charges present on both the mask and the polymer which breaks the surface tension on the resist. This allows for the formation of mounds between the stamp and the substrate that reach towards the mask. These mounds are usually formed in surface irregularities on the substrate which can act as nucleation sites. An example of these pillars forming is found in Figure 2.3.

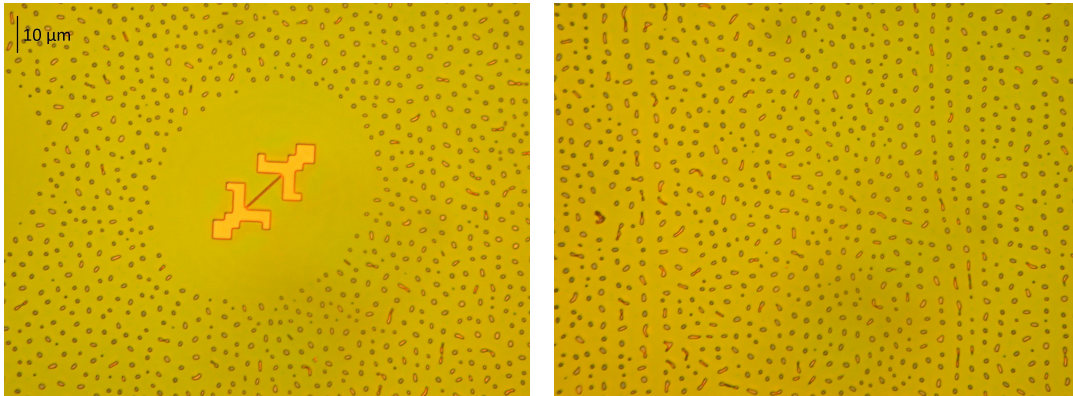


Figure 2.3: Pillar formation occurring due to nucleation sites on the substrate. Due to polymer displacement from the structures, the pillars did not form on top or near the imprinted resonators.

Viscous fingering can also occur on the stamp, which is due to trapped air between the substrate and the stamp. The air rapidly expands when the pressure is released after imprinting is finished but before the substrate is

cooled. This can produce finger-like or fractal patterns on the substrate. These patterns also occur if the initial pressure is applied too rapidly to the substrate (82). There is minimal damage on the substrate due to this occurrence because the air is trapped in a very small volume. An example of viscous fingering is shown in Figure 2.4.

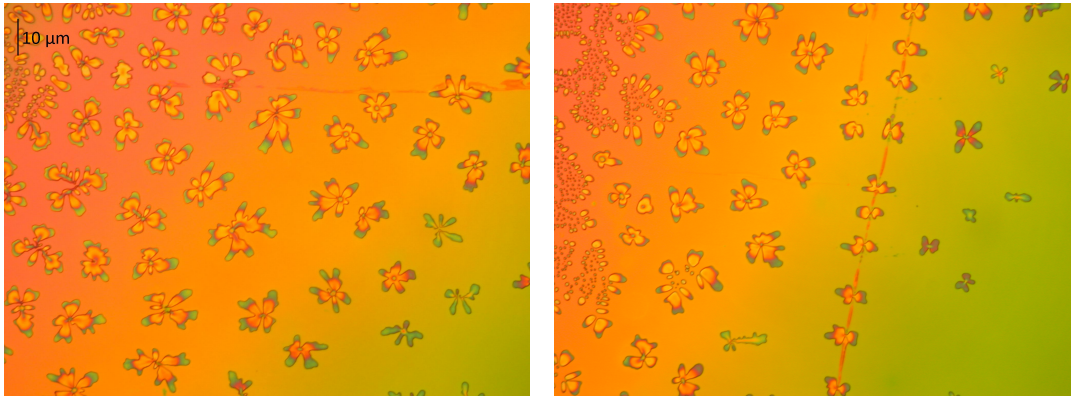


Figure 2.4: Viscous fingering on the substrate, which is caused by rapidly expanding trapped air.

## 2.7 Summary

The process of nanoimprint lithography is elaborated upon within this chapter. The strengths and weaknesses of thermal, UV, and roller NIL were summarized. Thermal NIL is the chosen form of NIL for this project due to the simplicity of making the mask using silicon rather than a transparent mask needed for UV NIL. The materials needed and the different forms of fabrication for the stamp are explained. We discussed why the structure height and density is important relative to the polymer being used for the substrate. Some of the resists which have been used with NIL were shown with their strengths and weaknesses summarized. The importance of the imprint parameters were summarized and the ideal imprint parameters were explained. The behaviour

of the polymer flow during imprinting was described. We also summarized the various defects which can arise during the imprint process.

---

---

## CHAPTER 3

---

### Nanomechanical Resonators

#### 3.1 Introduction

Nanomechanical resonators are devices which can be used for many different sensing applications. The devices consist of a beam with widths less than 1  $\mu\text{m}$  connected by two anchoring pads. These devices are extremely sensitive to shifts in mass and stress upon the beams, and they have been demonstrated to detect masses in the attogram (ag) and zeptogram (zg) range. There are many kinds of applications for mass sensing structures, such as explosives detection (14), bacteria detection (84), as well as other chemical and biological sensing (85). It is important to develop methods of mass fabrication of these sensing structures. There are various applications for these devices such as in hospitals and for national security purposes.

#### 3.2 Mass Detection Capabilities

Nanomechanical resonators are capable of measuring very small masses. One of the smallest sensitivities which has been obtained is approximately  $0.13 \text{ zg/Hz}^{1/2}$  by Zettl *et al.* (86). They were also to determine the mass of a

gold atom (0.327 zg) using resonator devices. Yang *et al.* have also detected small masses of 7 zg ( $10^{-21}$ g) (20). The smallest detectable mass with the resonators we have developed has been approximately 6 ag ( $10^{-18}$ g). Guthy *et al.* developed these devices with SiCN resonator devices measuring 16 nm wide, 50 nm thick, and 10  $\mu$ m long (27). SiCN is the chosen material for resonators for this project due to this ability for detection of small masses. The process flow which we have developed for the deposition of SiCN is shown in Table 3.1. The SiCN layer is annealed after deposition at 500°C and 100 sccm of N<sub>2</sub> for 4 hours. This will cause the SiCN layer to undergo a tensile stress. The anneal must be carefully controlled because stress plays an important factor in determining the mass sensitivity of the resonators.

There are multiple methods of detection to ensure great accuracy when determining the mass sensitivity of these devices. The three most prominent sensing methods include magnetomotive, piezoresistive, and interferometry methods. An interferometry approach is used for this thesis.

Table 3.1: Process Steps for PECVD SiCN Deposition

Process Step	Pressure (mT)	Power (W)	Time (s)	N <sub>2</sub> flow (sccm)	NH <sub>3</sub> flow (sccm)	DES flow (sccm)
Purge	500	0	60	55	40	0
Plasma pre-clean	500	40	60	55	40	0
Deposition (50 nm)	500	40	100	55	20	25
Post-purge	500	0	60	55	40	0

### 3.2.1 Magnetomotive Detection

Magnetomotive detection is one of the ways to measure the resonant frequency of cantilever and resonator devices. This system involves a powerful permanent magnet which produces a magnetic field that runs perpendicular to the

resonator beam (87). Figure 3.1 shows a general schematic diagram for a magnetomotive system. The motion of the devices is induced by introducing an RF (radio frequency) current to the resonator at the fundamental resonant frequency of the device. This current is generally produced using a series of resistors (88). The RF current creates a Lorentz force when it interacts with the magnetic field, which excites the vibration of the resonator. This mechanical displacement of the beam induces an electromotive force (EMF) which is proportional to the displacement of the beam from its equilibrium position (89). The EMF is measured on an analyzer via an impedance buffer. This technique for mass detection can be used both in vacuum and at atmospheric pressures (87). Magnetomotive detection has also been demonstrated at cryogenic temperatures and in water as has been demonstrated by Venstra *et al.* (90).

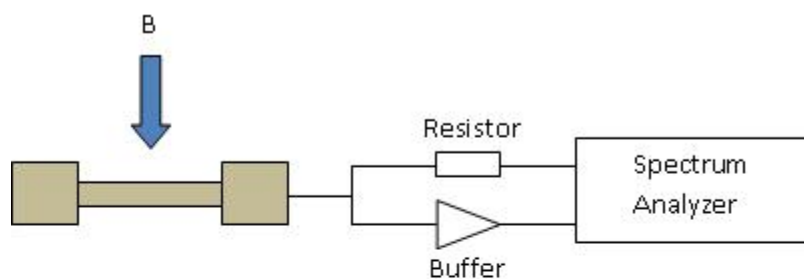


Figure 3.1: Schematic diagram showing a magnetomotive detection system.

### 3.2.2 Piezoresistive Detection

Another approach to measure the resonant frequencies of nanomechanical oscillators is piezoresistive transduction. Piezoresistivity is defined as the change in resistance caused by an applied stress (85). One material which exhibits a strong piezoresistive effect is doped silicon. Silicon is a widely used material when fabricating resonator devices so a piezoresistive approach to transduction will work well. The change in the resistance of the doped region once

it is deformed or stressed reflects the amount of deformation which occurred (85). The resistivity of the oscillator is measured by placing the device within a Wheatstone bridge (91).

There are several advantages to using a piezoresistive system. There is no need for expensive equipment or for any laser alignment to the device. The electronics necessary for read-out can also be integrated onto the same silicon chip as the oscillating devices (91). The optical transduction methods can suffer from some problems. One example are artifacts which are caused by changing optical constants within the media surrounding the device. This can cause the laser to move slightly around the substrate. Piezoresistive detection systems do not encounter this problem since lasers are not necessary. Piezoresistive methods also have the option to vary the temperature on the device to observe its effects on the resonating device. This is accomplished by changing the current flowing through the resonator. This has been shown by Berger *et al.* by analyzing the effects of various temperatures on a cantilever device (92). This heating effect can also cause another bending signal to occur. Further analysis of the device will be needed to remove this signal. Piezoresistive techniques also require design limitations upon the resonator or cantilever device. This means that thin and highly sensitive oscillators may not be used for piezoresistive transduction (91).

### 3.2.3 Interferometry

Another common technique which is used for frequency detection is interferometry. This is an optical method of detection, rather an electrical method like piezoresistive transduction. A laser is used to focus upon a single resonator and the surrounding substrate through a microscope objective lens and a beamsplitter. The beam is reflected by the resonator and the substrate, which returns through the objective lens and through the beamsplitter. The beam is then collected by a photodiode and the resulting data is recorded by a spectrum analyzer. Any deflection of the resonator beam will cause a small

modulation of the light intensity which will be detected by the photodiode. This modulation will be most pronounced when the resonator beam is excited at its resonant frequency. This is shown as a sharp peak upon the readout on the spectrum analyzer. The analyzer can also provide a drive signal to excite the resonator to resonance.

There are a few methods which can be used to excite the oscillator to its resonance frequency. One such method is using a piezo-element used by Sekaric *et al.* (31). A sample is attached to a piezoelectric element and an AC voltage is applied to it. This allows the structure to oscillate at its resonant frequency. Another method to drive the resonator is electrothermal actuation. This method involves depositing an electrical conductor onto the surface of the resonator to be actuated and applying a voltage to heat the structure. This will mechanically strain the resonator causing resonance (93). A material must be chosen which can stand high temperatures and will not break or fracture under strain for this technique to work properly. Silicon carbide (SiC) is a good candidate as it will not fracture under high temperatures (93). Other methods for actuation include electromagnetic (94), capacitive (95), and thermal actuation using a MESFET (metal semiconductor field effect transistor) heater (96).

### 3.3 Mass Sensing

One of the primary advantages of NEMS devices such as cantilevers and resonators is their use for mass sensing. These devices are extremely sensitive and are able to detect bacteria, proteins, and pathogens (97). The material which is being detected is bound to the resonator surface through one of two ways. The first method is through Van-der-Waals interactions. The second method which is more common is through binding with crosslinkers adsorbed onto the surface. Examples of crosslinkers include antibodies and biomarkers which can only bind to certain molecules or bacteria (98). It is possible to measure the shift in resonant frequency when an additional mass is adsorbed

onto the surface of the resonator beam by using one of the detection methods described earlier. This frequency shift can then be used in conjunction with the mass sensitivity of the oscillating beam to determine the adsorbed mass on the beam.

There are two important attributes to consider when running mass detection experiments. The first is the mass sensitivity of the structure. Mass sensitivity is described as the minimum mass which is detectable by the device. The second is the quality (Q) factor of the device. The Q factor characterizes a resonator's bandwidth with its central resonant frequency. This factor measures the stability and strength of the resonant frequency. The Q factor is a determining aspect for mass resolution upon the resonating beam making it a contributing component in any mass calculations. The higher the Q factor, the more stable the resonant frequency and thus the greater the mass sensitivity.

### 3.3.1 Mass Sensitivity

There are a number of factors which influence the mass sensitivity of a resonator. One of these factors is the mass of the resonator itself, which is determined by its length, width, thickness and the material used for fabrication. Other important factors include the resonant frequency of the device and the Q factor of the resonator. There are several different materials which can be used for mass sensing purposes. Some examples of these materials include silicon, gallium nitride (99), carbon nanotubes (100), gold palladium (101), and aluminum nitride (102). Each material will have an effect upon the overall mass sensitivity of the device. An equation which is used to estimate the mass sensitivity of a mechanical resonator is given by Ekinici *et al.* (21):

$$\delta m = 2M_{eff} \sqrt{\frac{\Delta f}{Q\omega_o}} 10^{-DR/20} \quad (3.1)$$

In this equation,  $\delta m$  is the mass sensitivity,  $M_{eff}$  is the effective mass of the resonator,  $\Delta f$  is the frequency bandwidth at the FWHM (full width at

half maximum) of the resonance spectrum,  $Q$  is the quality factor,  $\omega_o$  is the resonant frequency of the device, and DR is the dynamic range. The DR value is determined by the ratio of the amplitude signal and the noise signal as  $DR = 20\log(A_{signal}/A_{noise})$ . These amplitude signals are found through the resonance spectra obtained after each measurement.  $M_{eff}$  is determined by the density of the material used and the dimensions of the beam. The true mass of the resonator must be converted to its effective mass because the resonator behaves like a spring-mass model. The mass of the entire system will oscillate through the same maximum amplitude. However, a large portion of the resonator mass will not undergo the full range of oscillation. Therefore, the effective mass of the system is calculated to be 0.735 times its true mass (21). This means that the material used for the device greatly determines the mass sensitivity of the resonator. Equation 3.1 also shows that the mass sensitivity depends upon the  $Q$  factor of the resonator. Higher  $Q$  factors will lead to much greater sensitivity.

The resonant frequency of the device also factors heavily into the mass sensitivity of the device. The frequency can be calculated based upon the dimensions and material properties of the device. Equation 3.3 describes the resonant frequency for a rectangular cross-section undergoing a tensile stress vibrating in the vertical direction (103). This equation is derived from the Euler-Bernoulli differential formula shown in Equation 3.2, where  $E$  and  $I$  are the Young's modulus and moment of inertia respectively. The values of  $\sigma_0$ ,  $W$ , and  $t$  correspond to the initial stress, width, and thickness of the beam. The variable  $w$  is the vertical displacement of the beam at a certain position,  $x$ , and  $q$  is some external load acting upon the beam.

$$EI \frac{d^4 w}{dx^4} - (\sigma_0 W t) \frac{d^2 w}{dx^2} = q \quad (3.2)$$

$$f_i = \frac{i^2 \pi}{4} \sqrt{\frac{Et^2}{3\rho l^4} + \frac{4\sigma}{i^2 \pi^2 \rho l^2}} \quad (3.3)$$

The variables  $l$  and  $t$  in Equation 3.3 are the length and thickness of the resonator respectively,  $\rho$  is the density of the resonator, and  $\sigma$  is the tensile stress of the resonator. The index  $i$  defines which mode of resonance the resonator currently occupies. This variable must be solved for numerically for each resonance mode. The mode index for the first mode is defined as  $i = 4.73/\pi$  (104). The stress and the dimensions of the resonator greatly affect the resonant frequency of the device. Equation 3.3 can be reduced for low stress resonators to the following equation (27):

$$f_i = \frac{i^2 \pi}{4\sqrt{3}} \sqrt{\frac{E}{\rho}} \frac{t}{l^2} \quad (3.4)$$

The resonant frequency depends heavily upon the length and thickness of the resonator in the low stress limit. Equation 3.3 can be further reduced if the resonator is under high stress to the following equation (27):

$$f_i = \frac{i}{2} \sqrt{\frac{\sigma}{\rho}} \frac{1}{l} \quad (3.5)$$

The resonant frequency depends only upon the length of the resonator when under high stress.

The resonant frequency and mass sensitivity of the resonator will be changed by decreasing the dimensions of the resonator and by using different materials to change the mechanical properties of the device (85). It is important for the resonant device to have a low density to ensure that any molecule which adsorbs onto the device will be much more significant than compared with the mass of the oscillating device. Silicon carbonitride is a good material to use for resonator devices due to its high stiffness and low density. The density generally varies between 2000 kg/m<sup>3</sup> and 2600 kg/m<sup>3</sup> depending upon the deposition and annealing conditions (105).

### 3.3.2 Quality Factor

The quality factor, or Q factor, is a dimensionless quantity which can help to determine where energy losses occur within a resonator. There is always some loss of energy through thermal losses, losses through liquids, and through the atmosphere itself whenever an oscillating device achieves resonance. There are also some losses through the device itself, such as through the clamps on the resonator, dislocations, grains on the substrate or device, and other phenomenon like scattering from phonon-electron interactions and thermoelastic damping (106). It is possible to reduce the effect of some of these losses by using a vacuum to remove the effect of the atmosphere on the device. Lowering the temperature will also help to ensure there are no thermal losses. Changing the mechanical properties of the substrate by using different materials can also have an affect on the losses exhibited. One unique way to reduce dissipation to get a higher Q factor is to create an abacus-style resonator by depositing metal along the beam. Jensen *et al.* showed that this will shorten its effective length and will cause the resonant frequency to increase (107). This method allows for very high frequency resonators and high Q factors by utilizing this resonator design.

The Q factor can be used to determine the amount of lossiness which occurs. Increasing the value of the Q factor will decrease the amount of losses occurring. This will also ensure that the resonant frequency will be more accurate (108). A general equation which can describe the Q factor is as follows:

$$Q = 2\pi \frac{W}{W_o} \quad (3.6)$$

The variable W in Equation 3.6 is the amount of energy stored within the resonating device, and  $W_o$  is the amount of energy which is lost per cycle of oscillation. This equation can also be defined as a fraction of the resonant frequency over the bandwidth of the resonant spectra at the half power mark. The Q factor can thus be calculated by looking at the resonance spectrum

of the desired structure. An example of a resonance spectrum obtained from resonators which we have developed is shown in Figure 3.2.

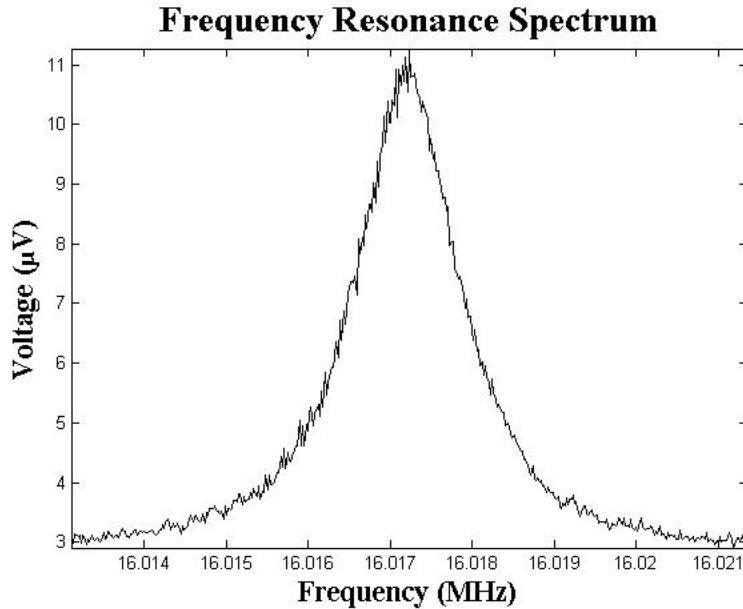


Figure 3.2: Resonance spectrum for a 50 nm thick, 14  $\mu\text{m}$  long and 300 nm wide resonator. The Q factor is obtained by the peak resonant frequency divided by the bandwidth of the overall spectrum.

It is also possible to quantify some of these loss sources which can occur during measurements through theoretical calculations. Examples include thermal losses (24), losses through the volume of the resonator (109), clamping losses for thin resonator supports (110), and surface losses on the resonator (109). It is possible to calculate the total inverse Q factor ( $1/Q$ ) for the device by taking the inverse sum of all forms of the Q factor. Some of these calculated Q values may not apply for all devices depending upon device dimensions or if there are gasses or liquids surrounding the resonator. One source of energy loss which can occur for these resonators is thermoelastic damping (TED). TED is caused by thermal losses from the stretching and compression of the resonator during oscillation. There are other sources of loss which can occur through these devices, such as through the piezoresistive chip which actuates

the resonators. Equation 3.7 shows the parameters which govern  $Q_{TED}$  losses:

$$Q_{TED} = \frac{c_v}{E\alpha^2 T} \left( \frac{6}{\epsilon^2} - \frac{6 \sinh\epsilon + \sin\epsilon}{\epsilon^3 \cosh\epsilon + \cos\epsilon} \right)^{-1} \quad (3.7)$$

$$\epsilon = t \sqrt{\frac{\omega \rho c}{2\kappa}} \quad (3.8)$$

The variable  $c_v$  in Equation 3.7 corresponds to the specific heat per volume,  $E$  is the Young's modulus,  $\alpha$  is the linear coefficient of thermal expansion, and  $T$  is the temperature. The variable  $t$  in Equation 3.8 is the thickness of the resonator,  $\omega$  is the angular resonant frequency,  $\rho$  is the density of the material of the resonator,  $c$  is the specific heat capacity, and  $\kappa$  is the thermal conductivity. The theoretical values for these parameters will be approximate to their real values. This means that the theoretical Q factor will be a magnitude higher than the values calculated from the resonance spectra. The Q factor limited by TED is heavily dependent upon the thickness of the resonator and on the properties of the material being used. Thinner resonator devices and materials with low densities will lead to higher Q factors. These equations show that the material must be chosen very carefully to ensure the highest possible Q factor attainable.

### 3.4 Review of NEMS - Biosensing

There have been numerous works done on the sensing capabilities of NEMS devices for chemical and biological purposes. These sensors can also be used to detect physical phenomenon like sound waves and acoustic vibrations (111). Pressure sensors and temperature sensors are also possible to use for resonator devices (112). The pressure on a cantilever or resonator in a gaseous environment can be detected by the movement of gas particles along the resonating beam as it is vibrating. The number of gas particles will increase when the pressure rises which will result in added mass to the resonating beam. This

will lead to a decreased resonant frequency and Q factor (112). Temperature sensors are also possible by utilizing the thermal expansion which occurs when the resonator material heats up and causes strain in the device. The change in strain will alter the resonant frequency of the device. The change in temperature can then be deduced by an analyzer. Materials which are highly sensitive to small changes in the resonant frequency are required. Examples of such materials include silicon nitride (112) and silicon nanowires (113).

### 3.4.1 Chemical and Biological Sensing

There are a diverse range of chemical and biological materials which have been detected using nanoelectromechanical resonators. It is now possible to detect a wide range of gaseous materials. Some examples include mercury vapor (114) and liquids for humidity sensing (111; 115). There are many potential benefits for detecting chemical and biological compounds. These benefits can involve disease diagnosis and gathering information about what is in a particular environment. Various chemical sensors capable of detecting numerous compounds have also been developed. Examples include hydrogen absorption on palladium/silicon cantilevers (116), chemisorption of mercaptoundecanoic acid (117), and ethanol compounds using gold-coated cantilevers (118). The detection of metal ions like calcium (119) and mercury (120) has also been achieved. Explosives detection is also possible with compounds like pentaerythritol tetranitrate. This compound is detected on silicon cantilevers by using a monolayer of mercaptobenzoic acid to bind to the explosives (121).

Ramos *et al.* have shown that it is now possible to detect strands of DNA on a resonator beam using 100 nm thick silicon nitride beams (122). Gold was deposited on the ends of the beams which were functionalized by thiol chemistries to attract the DNA molecules. Ilic *et al.* have also shown to detect the mass of a single DNA molecule on a resonator with minimal non-specifically bound material from the solution (123).

Other important breakthroughs involve the detection of cancer cells. One

example includes a protein biomarker associated with prostate cancer known as prostate specific antigen (PSA) which has been detected by several groups (124). Waggoner *et al.* have been able to detect small concentrations of PSA as low as 50 fg/ml (1 fg= $10^{-15}$  g) (125). This breakthrough will allow detection of any cancer biomarkers on a lab-on-a-chip systems. Bacterial detection can also be accomplished easily using nanomechanical resonators and cantilevers. Zhang *et al.* used Escherichia coli (E. coli) antibodies to detect E. coli bacteria using silicon cantilevers (16). Ilic *et al.* has detected E. coli bacteria with sensitivity down to a single cell using low-stress silicon nitride cantilevers (126; 17). Weeks *et al.* used silicon nitride cantilevers to detect Salmonella enterica strains of bacteria (13). They showed that only 25 adsorptions of bacteria onto the resonating beam is enough for the change in mass to be detected. Ilic *et al.* have also shown that it is also possible to detect viruses due to the increased sensitivity provided by nanomechanical resonators and cantilevers (97). They recently were able to create resonators with attogram resolution capabilities allowing for detection of certain pathogens (127). Gupta *et al.* were able to detect the mass of a single vaccinia virus which is the basis of the smallpox vaccine. They used silicon cantilever beams and they were able to detect the virus with an average mass of 9.5 fg (128).

### 3.5 Summary

Nanomechanical resonators were described in this chapter along with their potential applications. The forms of mass detection were summarized and their strengths and weaknesses were highlighted. The principles of mass sensing was described, and the calculations were shown to get theoretical values of resonant frequency and minimum detectable mass. These equations highlighted the importance of the material being used and the dimensions of the resonator. The importance of Q factor was summarized, and the many different factors which can contribute to the quality of the resonator were explored. The potential applications of resonator mass sensing was discussed with many examples

shown of current methodologies being used to detect masses of various chemical and biological compounds.

---

---

## CHAPTER 4

---

# Nanomechanical Resonator Imprints

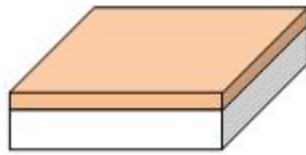
### 4.1 Introduction

This chapter is focussed on the successful imprints which have been completed for nanomechanical resonators. We discuss the steps taken to create the masks needed for these imprints and the rationale for the desired resonator beam widths. The degradation over time of these masks are discussed as well. We will show how the structures become damaged over time which can lead to smaller imprint yields after repeated use. Various resists have been used for experimentation to determine which resists work best for imprinting. The imprint yields after varying the concentrations of these resists are also discussed. The resists used include PMMA, PMMA/LOR, and mr-I 8030 E which is specifically designed for use in nanoimprint lithography. Nearly all of the imprints done for this project involved resonator beam widths of approximately 300 nm. This width was chosen because it provided a high signal-to-noise ratio for resonance measurements. We successfully achieved a lower limit of 120 nm wide, although device yield at these lower limits were degraded. This work was completed at the University of Alberta Nanofab, as well as the cleanroom facilities and electron microscope imaging systems at the National Institute for Nanotechnology (NINT).

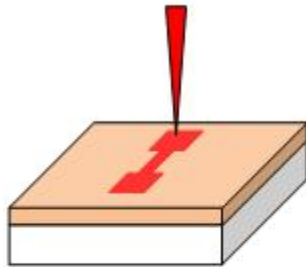
## 4.2 Mask Fabrication for Imprinting

There are several different methods of fabrication to create the masks for nanoimprint lithography. Some examples include electron beam lithography and photolithography. All of the masks which we have developed were silicon based and they were fabricated using EBL due to the need for small structures at or below 300 nm. Several masks were developed over the course of this work. One mask had varying resonator beam widths to see the minimum feature sizes for imprinting and another mask had an optimized resonator width which was used primarily for resonance measurements.

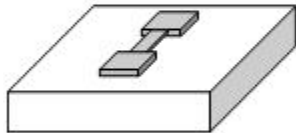
The process for creating the masks involves cleaning a silicon  $\langle 100 \rangle$  wafer with a piranha solution ( $3\text{H}_2\text{SO}_4 : 1\text{H}_2\text{O}_2$ ) and then cleaving the wafer to an area of approximately  $1\text{ cm}^2$ . A bilayer of PMMA 495 and PMMA 950 is spun onto the cleaved silicon chip. The silicon chip is placed into the EBL system and the desired pattern is exposed onto the photoresist. The chip is developed using MIBK:IPA (methyl isobutyl ketone : isopropyl alcohol) to remove the exposed resist. A 30 nm layer of chrome is then deposited onto the silicon mask using a metal evaporation system. Acetone is used to remove any remaining resist on the substrate. A plasma etch is used to remove approximately 300 nm of silicon in an isotropic RIE system. This etch is to ensure that the structures are at the correct height needed for imprinting. A hydrophobic anti-sticking layer is required to be deposited upon the mask after etching to ensure that no photoresist will rip off and stick to the mask during the imprint process. The anti-sticking layer which we have chosen is F13-TCS. This silane material is commonly used for nanoimprint lithography (129). This monolayer is deposited via vapor deposition. A process flow showing the fabrication of the mask is shown in Figure 4.1. A completed resonator on the silicon mask is shown in Figure 4.2.



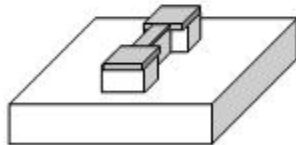
Deposit a bilayer of PMMA 495/950 upon a silicon substrate.



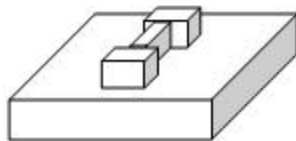
Use EBL to etch the desired resonator patterns into the resist.



After developing the resist using MIBK:IPA, deposit 30 nm of chrome, then remove the remaining resist using acetone.



Etch approximately 300 nm through the silicon substrate to provide enough room for imprinting to occur successfully.



Etch away the chrome layer, and deposit an anti-sticking layer on top of the devices.

Figure 4.1: Process flow for the fabrication of a silicon mask for NIL.

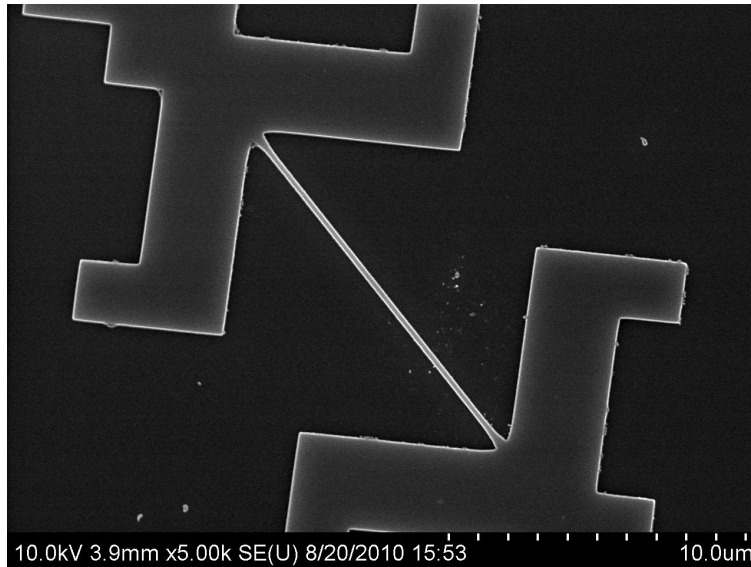


Figure 4.2: A completed resonator pattern on the silicon mask, with a width of approximately 220 nm.

### 4.2.1 Mask Degradation

Some of the devices on the mask became destroyed either through repeated imprints, mechanical failure or other factors. The damage to the structures is most likely caused by particles or resist beginning to stick to the mask after imprints. This caused the imprint yield to decrease rather substantially to about 60% total yield over a 6 month time frame. The mask was occasionally cleaned to ensure that any resist was removed to lessen the effects of degradation. We have already stated that the mask is capable of self-cleaning itself by re-applying any resist it has accumulated onto the substrate over subsequent imprints. The resist does still occasionally stick to the mask most likely due to the anti-sticking layer being slowly degraded over time. The mask for this project has been cleaned every couple of months using a piranha solution. The anti-sticking layer needs to be re-applied after each clean. The SEM (scanning electron microscope) images shown in Figure 4.3 show what happens to the silicon mask after about 6 months of use and several dozen imprints. The

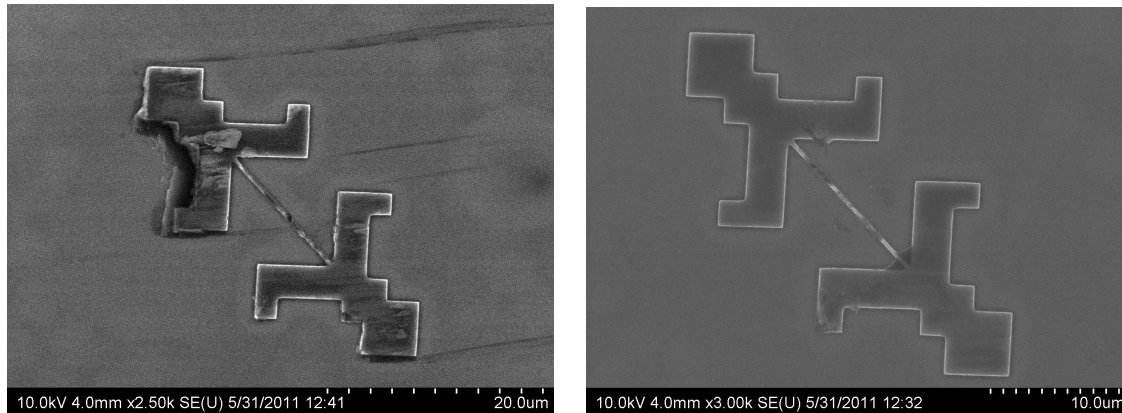


Figure 4.3: Structures on the imprint mask after over 6 months of use and several dozen imprints. Some of the devices become damaged, as shown on the image on the left, while others have resist sticking where the beams meet the anchor pads, as shown on the right image.

mask which is being used here contains 300 nm wide resonator beams.

### 4.3 Resonator Imprint Process

The thermal imprinting process can begin after the mask is fabricated and prepared. The process used is similar to that described in section 2.2.1. The imprinting substrate is larger than the mask to ensure that the resist will have enough room to flow around the structures during imprinting. This will also allow easier access to remove the mask from the substrate after imprinting is finished. The first step for the imprint process is to grow approximately 50 nm of SiCN onto a silicon substrate using PECVD. The substrate is then annealed for 4 hours to create tensile stresses within the SiCN material. The wafers are then cleaved into pieces which are larger than the imprint mask. A resist is then spun onto the cleaved SiCN pieces. Various resists have been used over the course of this project to determine which resists or combinations of resists will allow for the greatest imprint yield. These resists include PMMA, LOR 3A, mr-I 8030 E and SU 8. A bilayer resist consisting of PMMA/LOR 3A was

predominantly used for this project.

There is always a small layer of residual resist left behind after imprinting is completed. This layer can vary in thickness depending upon the height of the resist before imprinting as well as the conditions used during imprinting such as temperature and pressure. An oxygen plasma etch is used to remove the residual resist in an isotropic RIE under low pressure (10 mT, 7 sccm O<sub>2</sub>, 60 W) for approximately 90 s. Lowering the pressure within the reactor has previously been shown to improve the anisotropy of the etch process to produce vertical sidewalls (130). The process used for this project is not entirely anisotropic however, and there will be some line-widening which will occur. The line-widening effect is not noticeable for resonators which are about 300 nm in width. This effect becomes much more pronounced with thinner beams of widths less than 200 nm. These beams become wider by up to 100 nm or more.

A 30 nm layer of chrome is deposited upon the substrate after the plasma etch to fill in the gaps left behind from the imprint to form the structures. This deposition is performed in a metal evaporation system just like the metal deposition step for the mask fabrication. This step is performed under high vacuum to ensure a clean deposition with minimal defects. The remaining resist is then developed using Remover PG solution. A silicon carbide plasma etch is then performed to remove the silicon nitride. The silicon nitride is 50 nm thick meaning a 30 second etch is required using the silicon carbide etch recipe (25 mT, 95 W, 12 sccm O<sub>2</sub>, 48 sccm SF<sub>6</sub>). The remaining chrome on the resonators is etched away for approximately 20 minutes. A 32% solution of KOH is then used to etch the silicon underneath the structures to release them. This etch requires 3 minutes for devices that are 300 nm in width to ensure the devices are fully released. This etch time is reduced for smaller structures or else the smaller devices will most likely be destroyed by the etch process. The process flow for the fabrication of this device is shown in Figure 4.4 with a completed resonator device shown in Figure 4.5.

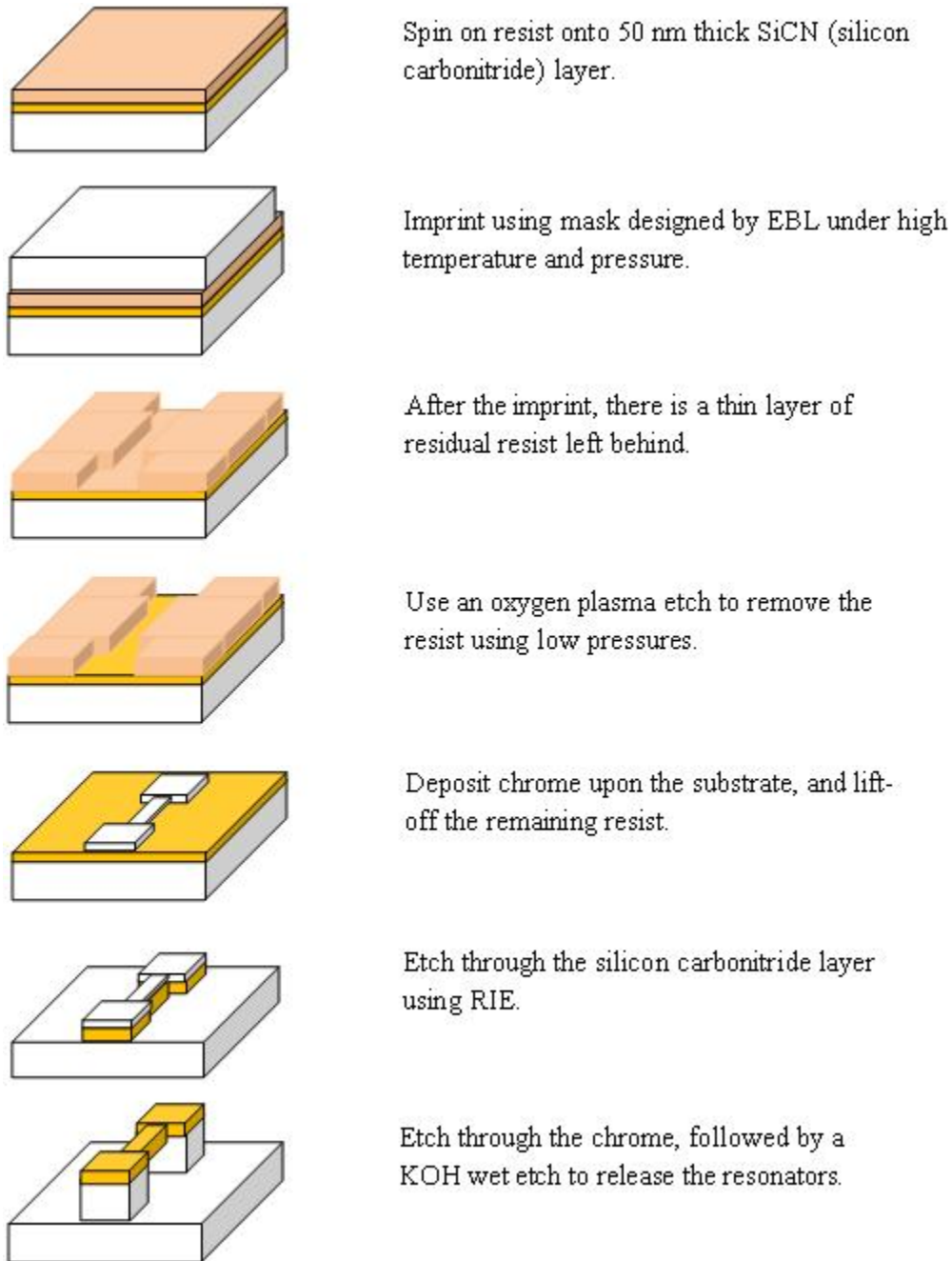


Figure 4.4: Process flow for the imprint and subsequent release of the resonator devices.

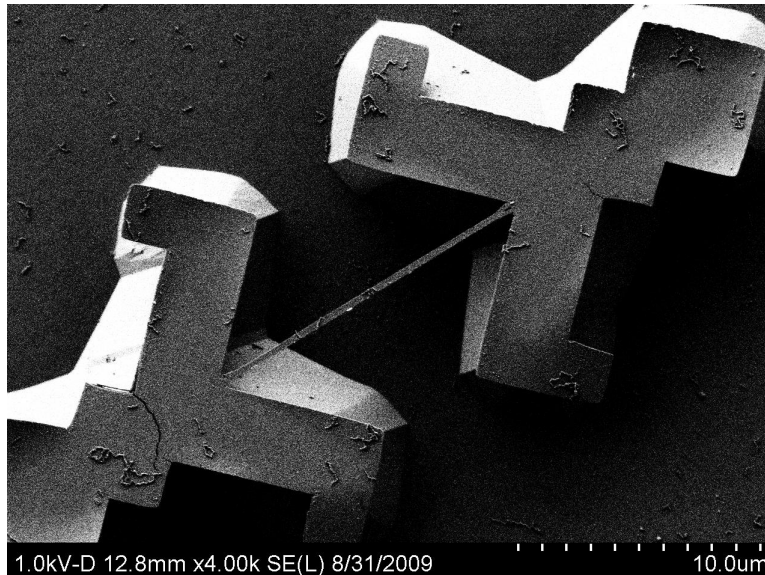


Figure 4.5: A completed resonator device which has been fabricated using nanoimprint lithography. This particular device has a width of approximately 300 nm.

## 4.4 Experiments

Various factors for the imprint process needed to be experimented upon to determine the best possible way to get good imprint yields. These factors include the photoresists used for the substrate and the temperature and holding time during the imprint process. The resists which were chosen have been known to work well for imprinting, such as PMMA (131), PMMA/LOR 3A bilayer (41), and SU 8 (132). Each resist that was used had a drastic effect upon the imprint yield ranging between 10% and 100%. The graph shown in Figure 4.6 shows the imprint yields for the various resists used during the course of this project.

Figure 4.6 shows that the greatest imprint yield is for the bilayer resist of PMMA 495/LOR 3A with a total thickness of approximately 300 nm. This resist was thus chosen for the majority of the experiments done for imprinting

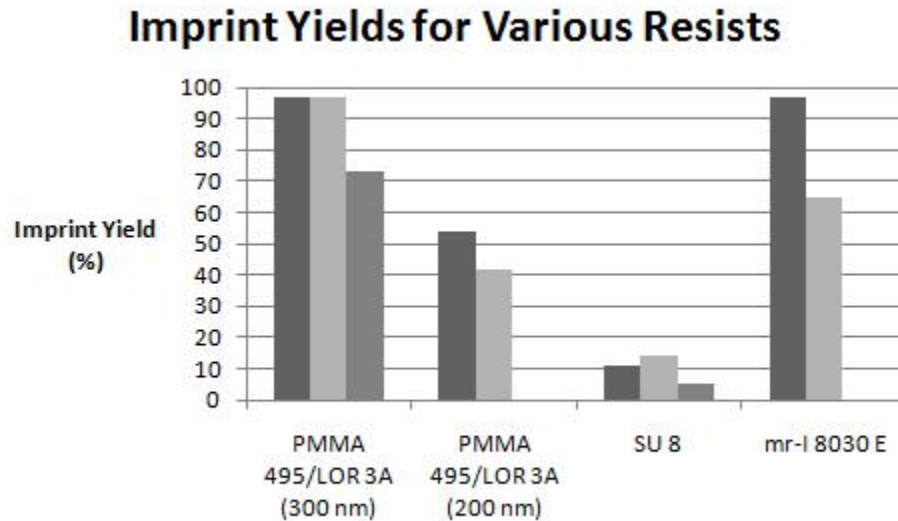


Figure 4.6: Relative imprint yield for different substrates using different resists. Each bar represents separate imprints for each resist. The 300 nm thick PMMA 495/LOR 3A bilayer shows the greatest yield, with the mr-I 8030 E resist showing great yields as well.

due to the very high yield shown. There was not a full 100% imprint yield after the devices were released due to a few damaged structures found on the imprint mask. The lower yields shown for both the 300 nm PMMA/LOR 3A bilayer and mr-I 8030 E resists are because the mask used for these measurements had taken some damage over repeated imprints, leading to lower than normal yields.

The initial experiments were done using PMMA 495 as the only resist layer for imprinting. PMMA 495 has a low molecular weight, so the resist should flow easily once the glass transition temperature is reached. The experiments were done at temperatures of around 180 °C with a pressure of 200 psi (pound per square inch). The images in Figure 4.7 show the resulting imprints after these initial experiments.

Figure 4.7 shows that the resonator beams themselves survived the imprint process. The anchor pads did not retain their original shape. This is most

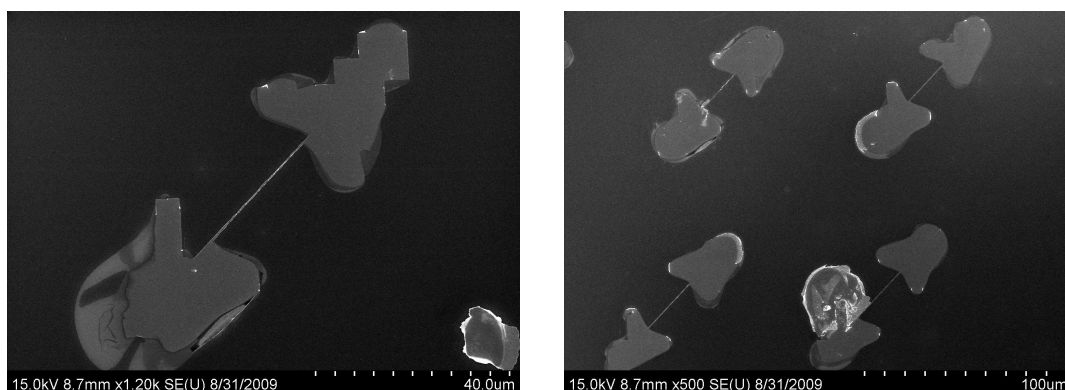


Figure 4.7: Resonator imprints using PMMA 495 as the resist layer. The beam structures remained intact for the imprints, although the anchor pads do not retain their shape.

likely due to the imprint hold time not being long enough. The hold time was for about 30 seconds for these initial experiments. This hold time was not long enough to ensure that the resist could flow around the structures. The images shown in Figure 4.7 were taken after the chrome deposition step because these structures were not released for the initial experiments. We also discovered that after plasma etching away the residual layer of PMMA that the resist became extremely resistant to its usual solvents. It took considerably longer to remove the remaining PMMA after the chrome deposition step for the fabrication process. An alternative resist needed to be found to decrease the length of time needed for the fabrication process.

The resist which was used in its place was a bilayer resist containing PMMA 495 and LOR 3A. A similar process was used by Cui *et al.* for their fabrication of large area nanoprism arrays (74). They used a combination of PMGI and PMMA for their imprint resist. LOR is a derivative of PMGI, and this resist was readily available in the Nanofab facility at the University of Alberta. A bilayer resist containing PMMA 495/LOR 3A was thus proposed to try and get higher imprint yields than that of PMMA 495 alone.

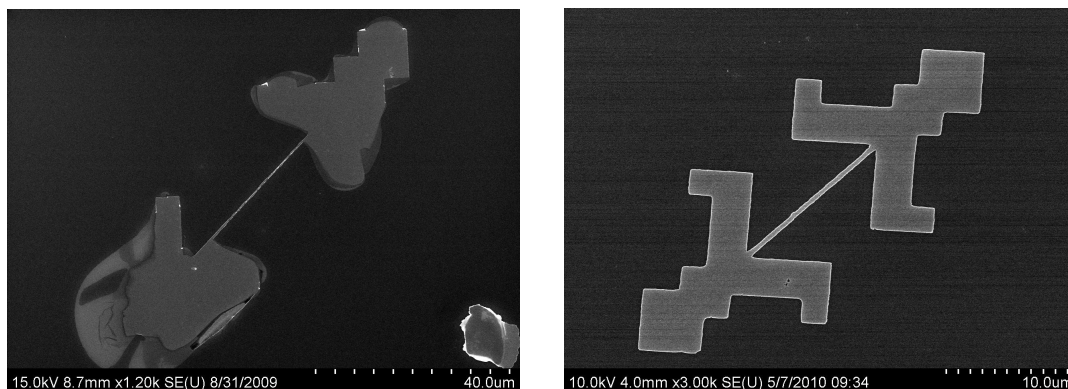


Figure 4.8: Comparison images between PMMA 495 imprints on the left, and imprints using PMMA 495/LOR 3A on the right. Both images were taken after the chrome deposition step during fabrication.

#### 4.4.1 Bilayer Resist Imprints

The initial experiments for using a bilayer resist using PMMA 495/LOR 3A consisted of a diluted LOR 3A resist to get the bottom resist layer much thinner than its undiluted counterpart. The dilution formula consisted of adding approximately 4 mL of ethyl lactate to 15 mL of LOR 3A. This brought the overall thickness of the resist down to about 200 nm. The PMMA 495 added an additional 90 to 100 nm to give a total resist thickness of about 300 nm. This height is close to the structure height of the mask being used for experimentation. The results of the bilayer imprints are compared with the single layer PMMA imprints in Figure 4.8. A fully released structure using the bilayer resist scheme is shown in Figure 4.9.

The same imprint parameters were used for the bilayer resist scheme as for the single layer PMMA 495 imprints. The only critical difference is that the imprint hold time was increased from 30 seconds to 2 minutes. This increase will allow for more time for the resist to flow around all the structures to create a perfect imprint of the mask devices. Figure 4.8 shows that this increase in imprint hold time allows for the anchor pads and the resonator beams themselves to have better uniformity. This resist scheme is used for the majority of

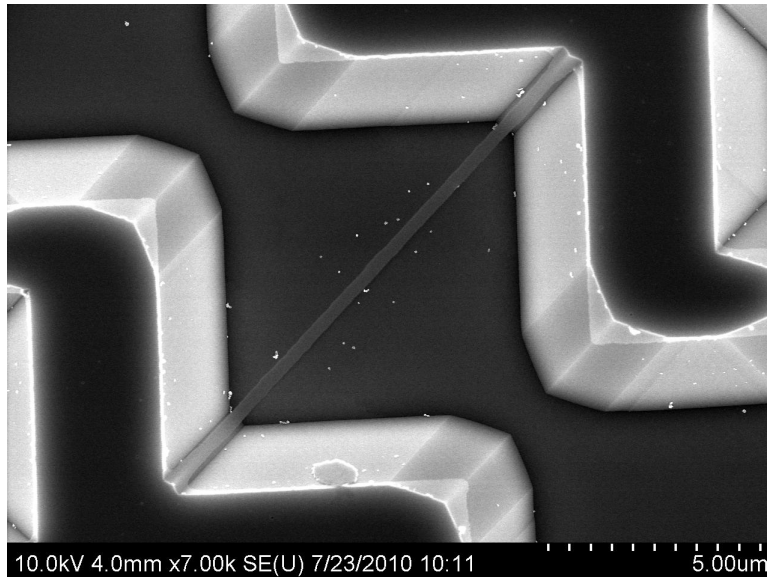


Figure 4.9: This is a released resonator created using the 300 nm thick bilayer resist of PMMA 495/LOR 3A. The resonators produced for this sample have a width between 300 nm and 320 nm.

the resonance data gathered for the imprinted devices, which will be shown in Chapter 5.

We have previously stated that it is ideal for the resist being used to be less than the height of the structures to ensure the best possible imprint. There have been some defects on the substrate even though the 300 nm thick PMMA/LOR bilayer results with good yields. These defects usually surround the structures or are located elsewhere on the chip. They very rarely affect the structures. Occasionally some of these defects protrude into the resonator beams. A thinner resist scheme using the same bilayer technique was proposed to counteract these defects. The LOR 3A layer was further diluted to less than 100 nm. This will ensure that the total resist height will be less than 200 nm, compared with the 300 nm tall structures on the mask being used. The comparison image shown in Figure 4.10 shows the resulting imprints after the residual resist layer etch for a thick resist layer ( $\sim 300$  nm) on the left, and a thinner layer ( $\sim 220$  nm) on the right.

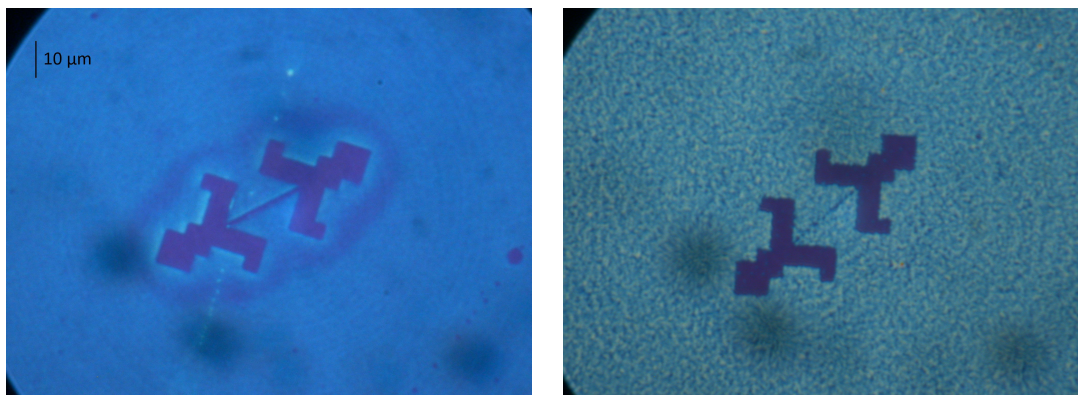


Figure 4.10: Microscope images comparing the imprints of a thicker LOR 3A layer (left) with a thinner layer (right).

It is clear to see that the thicker LOR 3A layer is much smoother than compared with the thinner layer. The resonator beam for the thick layer is clearly more visible and uniform while the beam for the thinner resist is barely visible and in several pieces. The surface defects which were already present upon the substrate were not filled in entirely when the thinner resist was deposited upon the substrate. This would result in the uneven nature of the substrate seen in Figure 4.10. This would cause the resulting imprint to be uneven itself. The average imprint yield for the thinner resist bilayer of around 40%, compared with near 100% yield for the thicker resist bilayer.

We have already discussed that the plasma etch process being used to remove the residual layer after each imprint can cause line-widening effects. The 300 nm wide devices are usually widened by 20 to 30 nm. We proposed a second wet etch to remove the bottom LOR 3A layer of resist to counteract this widening. This would also result in a short plasma etch to only remove the PMMA remaining after the imprint. The wet etch being used is a developer called MF-319 which is used to remove LOR resists. This technique has been shown to work before for bilayer imprint techniques by other groups. Luo *et al.* used PMMA/LOR bilayers with this wet etch technique to produce interdigitated cantilever arrays (41). The wet etch being used does not affect

the top PMMA layer resulting in a near vertical etch to the SiCN layer. The majority of the resonators produced for this project used both etch methods. This process will allow for resonators which will be closer in width to those devices on the imprint mask.

The other imprint resist which resulted in high imprint yields was mr-I 8030 E. This resist was developed by Microresist Technology and it is specifically designed for nanoimprint lithography. It has good film uniformity, low glass transition temperatures of around 115 °C, and better resistance to plasma etching compared with standard PMMA resists (133). The mr-I 8030 E resist proved to be on par with resist yields shown by the PMMA 495/LOR 3A bilayer resist scheme. One major advantage of this resist when compared with the bilayer resist is that the etch time to remove the residual layer is reduced by approximately 30 s. There is only one layer for this resist scheme so no secondary wet etch is needed. One of the disadvantages is that the number of defects surrounding the structures seems to have increased dramatically compared with the bilayer resist imprints. This could be due to the resist not having enough time to flow around the devices during imprinting. These experiments were performed using the same 300 nm resonator width mask as the bilayer PMMA/LOR 3A experiments. The imprint yield was reduced significantly from 97% from the original experiments to 60%. This reduction in yield is due to the fact that there has been degradation over the course of dozens of imprints using the same mask. An example showing the imprints using this resist scheme is shown in Figure 4.11.

Most of the devices survived the imprint process, although unlike the bilayer resist scheme showed earlier, there are numerous defects surrounding the structures. These defects do not interfere with the structures themselves so resonance measurements can still be recorded for these devices. The most likely explanation for the appearance of these defects is due to a short imprint time. The imprint hold time for these devices was 2 minutes just like the bilayer resist. It is possible that the resist will have had enough time to flow around the structures if the imprint time was increased to 5 minutes or longer. This

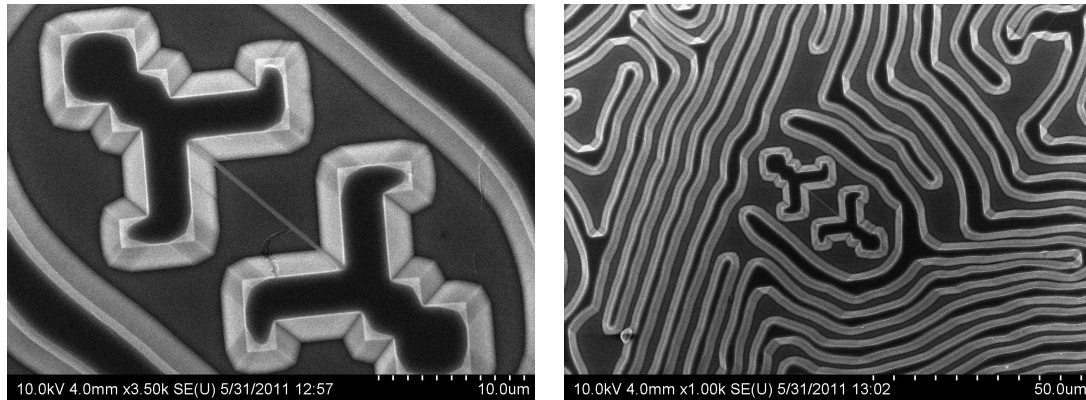


Figure 4.11: Resonator imprints using mr-I 8030 E as the resist layer.

will ensure that there will be minimal defects left behind.

## 4.5 Sub-300 nm Wide Imprint Experiments

Most of the experiments which were conducted for nanoimprint lithography were using structures which had beam widths of approximately 300 nm. This beam width was chosen because it provided an optimal signal-to-noise ratio when taking measurements for mass sensing. We have previously produced these resonators with this approximate beam width by EBL. It was ideal to provide proof that NIL would work for resonators 300 nm in width. It is also beneficial to create resonator devices with even smaller widths as this will make the devices even more sensitive to masses adsorbed onto the structure. A mask was used for these experiments which had varying resonator beam widths ranging from 50 nm up to 500 nm wide. This will show which beams will survive the imprint process using the various resist schemes. One of the resonators being used for the mask is shown in Figure 4.12.

The initial resist scheme we used was the 300 nm thick PMMA 495/LOR 3A bilayer resist scheme. We found that the imprints were only partially successful. Figure 4.13 shows that the smallest resonator we were able to

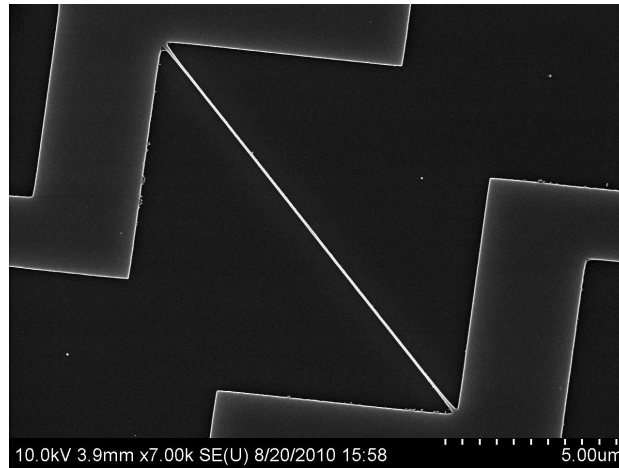


Figure 4.12: This is a resonator used for the imprint mask to create devices with beam widths of less than 300 nm. This particular structure has a beam width of approximately 60 nm.

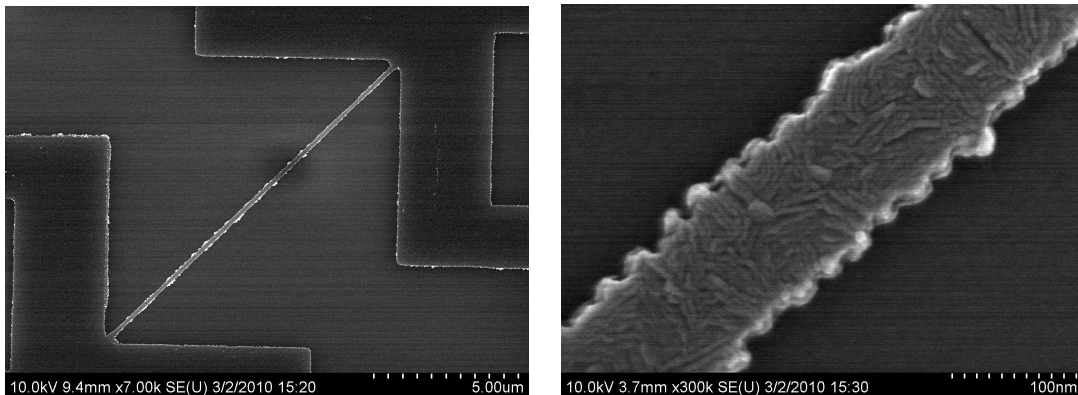


Figure 4.13: SEM images of the smallest resonator beam to be imprinted, with a width of approximately 120 nm. These images were taken after the chrome deposition step during fabrication.

imprint successfully was approximately 120 nm wide.

The resonator shown in Figure 4.13 was not taken past the chrome deposition stage during fabrication. It is clear to see from these images that it is possible to achieve smaller resonator beam widths using nanoimprint lithography. The

beams being shown here were supposed to be approximately 50 nm wide. This width is the smallest fabricated beam on the mask. The beams were widened considerably by a couple of magnitudes at some point during fabrication. We have already stated that line widening effects were observed for the 300 nm wide resonator devices during the plasma etch step. It is clear that this effect caused the widening seen here. Other attempts to imprint thinner resonators included using different resist thicknesses or different imprinting parameters. Temperature increases or increased hold times resulted in the same effect with very few of the imprints surviving. One way to achieve the thinner beams would be to use an anisotropic plasma etch. We could also use the second wet etch step discussed earlier to remove the LOR 3A bottom layer. We were unable to perform either of these steps due to time constraints to try and improve the imprint yield and resonator beam width.

The mr-I 8030 E resist was also used for the sub-300 nm wide imprint experiments in an effort to try and improve the yield and beam width. This resist was specifically designed for NIL and it has already yielded good results for the 300 nm wide resonators. It is possible that this resist may be more effective to create smaller resonator beams. The initial yields for these experiments were between 90 and 100%. Figure 4.14 shows that the line widening effects still occurred for these devices.

The smallest resonator fabricated by imprinting has an approximate width of 320 nm. This is much larger than the smallest resonator beam fabricated by EBL for the mask. The width for the imprint should have been approximately 30 nm. The blurred portions of the resonator shown are most likely due to charging effects from the SEM. The imprinted samples shown were imaged only after the chrome was deposited. The width of these devices would most likely decrease once the chrome is removed, but the overall change would be minimal. The maximum difference in width after the chrome is removed would be approximately 50 nm. A different etch recipe was used for these devices in the isotropic RIE. This process involved a much lower pressure of approximately 10 mT. The lower pressure helps to ensure that the etch is

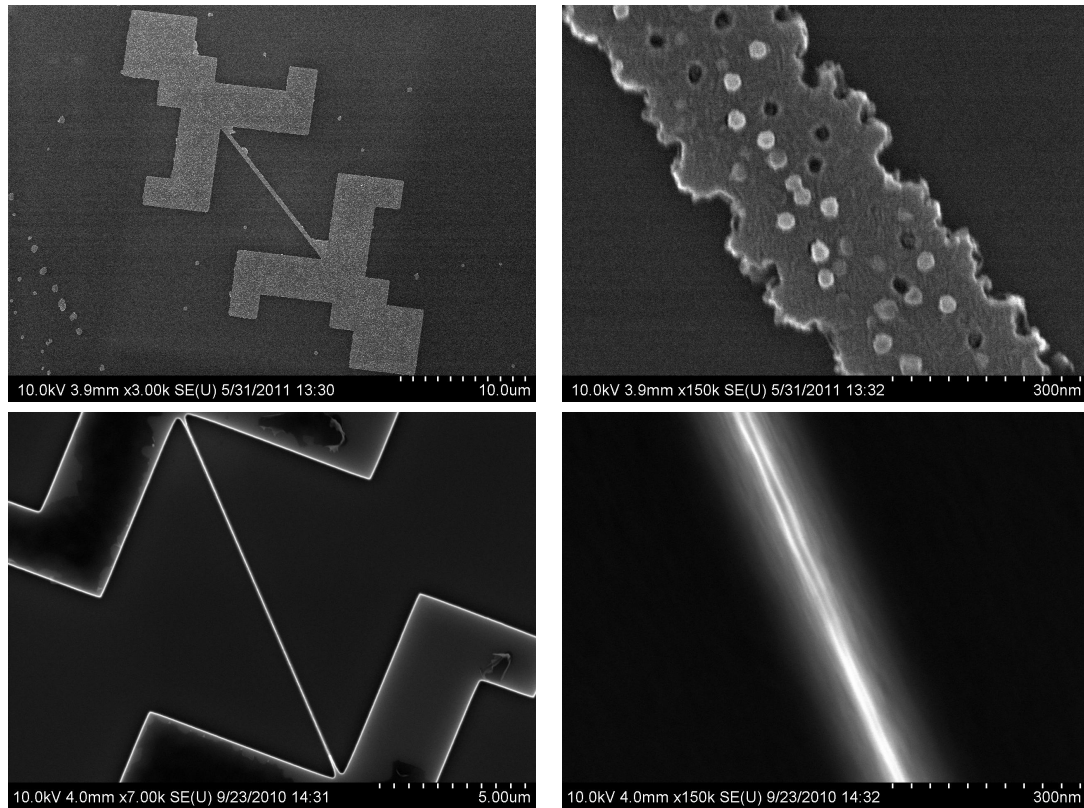


Figure 4.14: These images compare the mr-I 8030 E resist imprints (top) with the corresponding mask devices (bottom). The imprinted structures were imaged after the chrome deposition step.

closer to being anisotropic. It wasn't enough to bring the resonator width equal to the device width on the mask. The imprint yield for these samples was 100% showing that the mr-I 8030 E resist does work for these imprints. Further experiments need to be performed to ensure that the correct resonator width will be imprinted. These experiments can include using an anisotropic etch recipe or a system which has greater etch accuracy. Altering the imprint parameters such as the hold time or the pressure may also affect the imprint yield of the thinner resonators.

## 4.6 Conclusions

The various experiments performed show that it is possible to use nanoimprint lithography to create nanomechanical resonator devices with widths as thin as 120 nm. This process is much quicker to use than the standard fabrication techniques like EBL. These experiments show that it is possible to use this technique for mass fabrication purposes. We have shown that various photoresists can be used for the nanoimprint process with varying degrees of success. The bilayer resist scheme of using PMMA 495/LOR 3A with an overall thickness of 300 nm has been proven to be the best resist to be used for NIL. The ideal imprint parameters include a temperature of 180 °C, pressure of 200 psi, and an imprint hold time of 2 minutes. The specially designed resist mr-I 8030 E was also very effective at imprinting resonators. This resist used the same imprint parameters as for the bilayer resist scheme.

There was only partial success when imprinting resonators with smaller widths below 100 nm. It will be possible to use the above resists if different etch recipes or anisotropic plasma etches are used. We have shown that the imprint masks can be used multiple times before requiring cleaning due to the self-cleaning ability of the nanoimprint process. The PMMA 495/LOR 3A resist scheme is used primarily to create the devices needed for resonance measurements and mass sensing. The mr-I 8030 E resist is also used towards the end of the project to determine if there were any significant differences between the two resists being used.

---

---

## CHAPTER 5

---

### Resonance Measurements

#### 5.1 Introduction

The primary use of nanomechanical resonator devices is for mass sensing due to their increased sensitivity to any mass which lands upon the surface of the device. This chapter will discuss the measurements made for the imprinted resonator devices using 50 nm and 70 nm thick devices. The Q factors for these devices with no additional masses deposited upon them are calculated and compared with the theoretical values. The resonance measurements for the bare SiCN resonators were in close approximation with the predicted resonant frequencies for resonators made by EBL. Biotin and streptavidin were used for mass sensing to show that imprinted resonators can function just as well as the devices made from EBL. A control experiment was run where one sample was oversaturated with biotin and streptavidin and another sample was exposed to normal concentrations of streptavidin. This experiment showed that any changes in resonant frequency was not due to non-specific binding. These experiments help to show that nanoimprint lithography can be used to successfully create resonator devices which can be used for mass sensing purposes. These imprinted resonators are able to perform their functions just as well as those devices made by other fabrication methods.

## 5.2 Surface Functionalization

Nanomechanical resonators are highly susceptible to a wide range of external stimuli (134). Such stimuli include heat causing expansion or contraction in structures or masses attaching onto the devices causing shifts in resonant frequency. These devices will not be useful if it is not possible to determine what is causing the specific stimulus. The surface of the resonator devices must be functionalized with a specific binding agent which can detect certain biological species like proteins, bacteria or viruses. Two commonly used mass sensors are quartz crystal microbalance (QCM) and surface plasmon resonance (SPR). A QCM works by driving a thin slab of quartz crystal to its resonance frequency and measuring the change in frequency when masses are adsorbed to its surface (135). The frequency of the quartz disc is determined by its dimensions, elastic modulus, and its density. An SPR is an optical sensor which works by illuminating a thin metal film usually made of gold. The reflected intensity is then read by a photodetector. The intensity drops when masses are adsorbed onto the surface of the metal film. The material upon the film can thus be determined by this drop in light intensity (136). The surfaces on both of these sensors must be functionalized in order to detect specific biological or chemical components. Some typical uses for functionalization include imprinted nanoparticles (137), polymers like polysaccharides (138) and self-assembled monolayers (SAMs) (139; 140). The specific functionalized surface only allows one specific analyte to attach to the surface of the device. This ensures that any change in resonant frequency or light intensity is due to that particular analyte.

Nanomechanical resonators also need to be functionalized in order to detect specific biological agents. It is not necessary for these sensors to be functionalized as some compounds may adsorb through physical interactions with the resonator. Most applications require resonators to detect specific particles of varying compositions and sizes like proteins, antibodies, viruses and bacteria (141). The surfaces of the resonator beams must be coated with a layer of

material which is capable of attracting the desired molecules. The resonator must also reject any other materials to ensure that the mass being detected is only from the specifically targeted compound. There have been numerous experiments performed on nanomechanical resonators and cantilevers which use different methods of functionalization to immobilize certain molecules. Zhang *et al.* used antibodies on microcantilever sensors to detect *Escherichia coli* cells (16). Waggoner *et al.* also used antibodies for the detection of biomarkers related to prostate cancer (125). Yoo *et al.* used bioluminescent bacteria which were bound to the surface of the sensor to detect specific toxins (142). One key factor which is needed for any detection system is an intermediate chemistry which will attach the binding agent to the surface of the resonator or cantilever. The most commonly used chemistries are self-assembled monolayers, otherwise known as SAMs.

### 5.2.1 Self-Assembled Monolayers

Self-assembled monolayers are defined as a molecular assembly which is formed by an active surfactant that is adsorbed onto a surface (143). These materials are well-documented and understood for the functionalization and formulation onto surfaces (144). The species spontaneously self-organizes itself into a complete monolayer after being adsorbed onto the surface. SAMs are made of three components consisting a head portion which adsorbs onto the surface of the material, a long carbon chain which can vary in length depending upon the species of SAM, and a tail portion, called the functional group, which can bind to other species (145). Figure 5.1 shows a generic diagram showing the structure of a SAM molecule.

There are two types of SAMs which are frequently used for biodetection and immobilization: alkane-thiols and organo-silanes. Alkane-thiols have a S-H group on the head portion of the group which enables strong bonds with many metals, particularly gold (146). Gold is an inexpensive thin film which is easily deposited upon substrates by vapor deposition or other means. It is for this

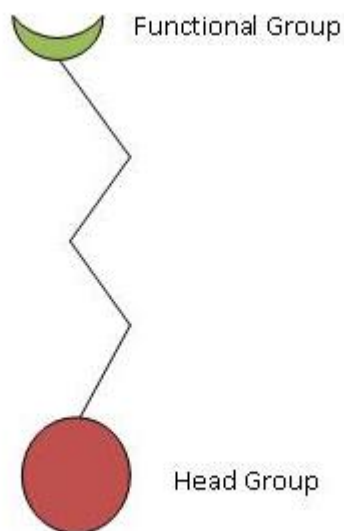


Figure 5.1: A generic diagram of a SAM molecule. The head group attaches itself to the substrate, while the functional group is attached to the binding agent for biodetection.

reason that alkane-thiols (thiols) are often used for functionalizing resonator and cantilever surfaces (147). The addition of gold onto resonator surfaces will also affect the resonant frequency and the  $Q$  factor of the device. Adding gold layers will decrease the  $Q$  factor and the mass sensitivity of the resonating transducer (148). It is possible to deposit gold only on certain sections of the cantilever or resonator where the adsorption of biological agents will affect the resonant frequency the greatest (127). This fabrication process will allow for thiols to work efficiently for NEMS devices. It will also further complicate an extremely delicate process. It is for this reason that thiols are not the ideal SAM to use for biodetection purposes.

Organosilanes are used for this project, which consist of a silicon-based head group. The silicon needs to bind with a hydroxyl group to form siloxane bonds in order to bind with the surface (143). The synthesis of these SAMs and the customization of their tail heads to allow for the binding of specific analytes is well known and developed (149). Organosilanes do not require metals like

gold to bind to the surface like alkane-thiols. They only require the presence of hydroxyl groups which can be provided in a solution. This means that the Q factor of the resonator will not be adversely affected once the SAM is adsorbed to the surface. The organosilane used in this project is aminopropyltriethoxy silane (APTES). Glutaric acid is used to attach the hydroxyl groups to the silane solution. The next step after adsorbing the SAM to the surface is to attach the binding analyte. These analytes are responsible for attracting the specific biological molecule needed for detection.

### 5.2.2 Binding Agents

We have previously mentioned that there are numerous types of binding agents available. They each serve different functions depending upon the type of molecule needed for detection purposes. The binding agent used for this project is biotin which is specifically used to target streptavidin. Streptavidin is a protein purified from the bacterium *Streptomyces avidinii* (150). Streptavidin has a high binding affinity towards biotin which means that no other molecules will attach themselves to the biotin during incubation. The biotin-streptavidin complex has been used many times before (19; 151) and their chemistry is well understood (152). These compounds were therefore chosen for the biosensing portion of this project. Figure 5.2 shows the binding of streptavidin to biotin on a functionalized organosilane surface.

## 5.3 Experiment

There were several experiments performed upon the imprinted resonators created in Chapter 4. The resonators which we created were made out of SiCN and they were all 300 nm wide, 14  $\mu\text{m}$  long, and 50 nm thick. Other sets of devices were created which were 70 nm thick with the same length and width. The devices are placed in an interferometry setup under a high vacuum. Figure 5.3 shows the setup used for the duration of the project. An He-Ne laser

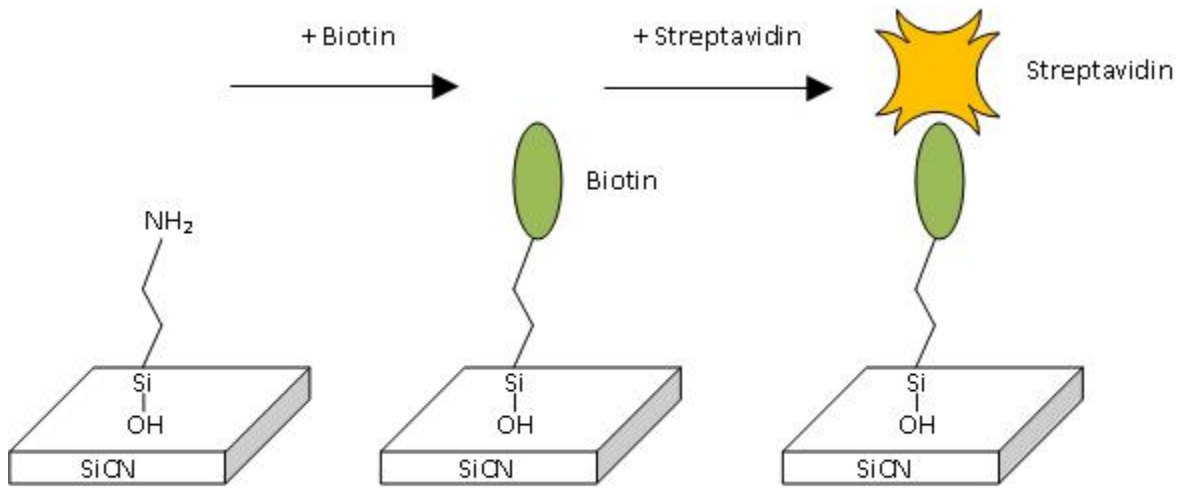


Figure 5.2: A diagram showing the process, from left to right, of functionalization of APTES to the surface, binding biotin to the monolayer, and the attachment of streptavidin to biotin.

is directed onto a beamsplitter, then through a microscope objective and onto the resonator device. The laser beam then reflects off the resonator and the substrate, goes back through the objective lens, and reflects off the beamsplitter where the beam is detected by a photodetector. The reflected laser beam will modulate its frequency through interferometric effects once the resonator is actuated at its resonant frequency. This modulation can be detected and shown on a spectrum analyzer to determine the resonant frequency of the device.

The initial experiments conducted involved resonators which were 40 nm thick, 300 nm wide and 14  $\mu\text{m}$  long. The resonance measurements are calculated for a select number of devices over the full sample size of 100 resonators. The Q factor is also calculated for these beams and is compared with the theoretical resonant frequency and Q factor. Resonators with a thickness of approximately 70 nm were also imprinted and measured. The frequencies and Q factors for these devices are compared with the 40 nm thick devices.

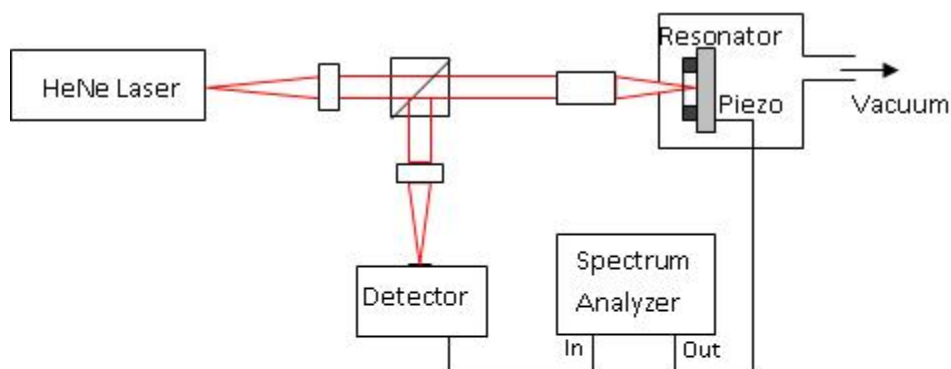


Figure 5.3: Schematic diagram of the interferometry setup for resonance-assaying measurements.

The biotin-streptavidin complex was adsorbed onto the surface of these resonators after the initial measurements. The mass sensitivity and subsequent drop in resonant frequencies were recorded. A negative control experiment was performed where the streptavidin was oversaturated with biotin before adsorbing onto the resonator. This experiment was performed to conclude that no additional masses were adsorbed through non-specific binding.

## 5.4 Results

### 5.4.1 Resonance of 40 nm Thick Beams

The initial tests involved measuring the resonance frequency of bare SiCN resonators 300 nm wide, 14  $\mu\text{m}$  long and 40 nm thick. Figure 5.4 shows the resonance frequency for several devices on one sample. This sample was produced using the bilayer resist scheme of PMMA 495/LOR 3A as the imprint resist.

The frequencies for these devices are fairly close together and range from 15.8 MHz to 16.3 MHz. The average frequency of for this set of devices is 16.1 MHz.

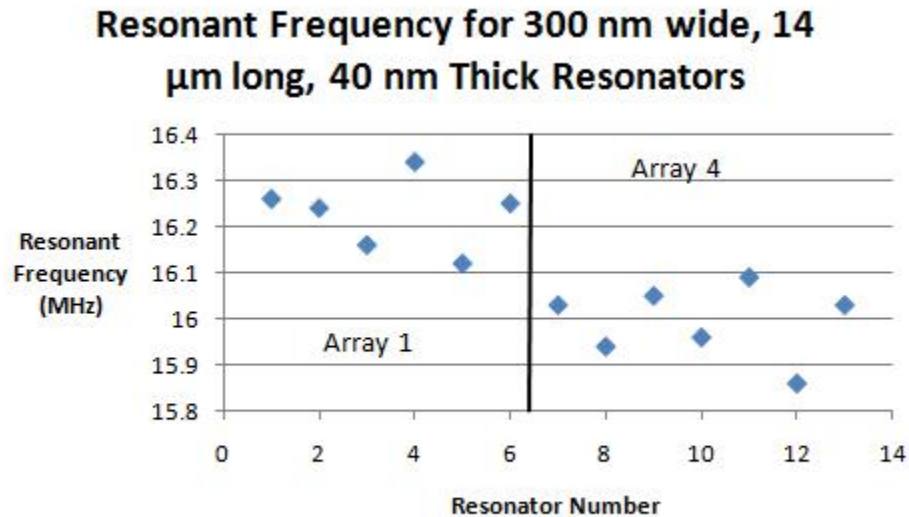


Figure 5.4: The fundamental resonant frequencies for a number of resonators on two arrays are measured. These devices are 40 nm thick, 300 nm wide, and 14  $\mu\text{m}$  long.

This range in frequency is normally caused by slight variations in length of the beam either due to the imprint process or from differences in length on the imprint mask itself. There is also a shift in frequency of approximately 200 kHz between the two arrays for this sample. This shift is most likely caused by slightly varying stress levels throughout the sample or by small variations in thickness. The arrays for all samples produced are approximately 1 mm apart from each other. Any variations in stress or thickness will be very minimal at these distances.

These resonant frequency values have been predicted for devices of these dimensions by Guthy *et al.* (27). Equation 3.3 shows that it is possible to find the theoretical frequency for resonators using the predefined dimensions and measured tensile stress values of approximately 500 MPa. Table 5.1 shows the material properties of SiCN which contribute to the resonant frequency of the resonators. The predicted theoretical frequency for these resonators is approximately 25.67 MHz. This is a fairly close approximation to the actual

values. The change in frequency between the actual and theoretical values is most likely due to differing stress values or Young's modulus values. It is also possible that there were thermomechanical fluctuations which arised during measurements when the laser measured the resonant frequencies. This could have affected the stress of the device.

Table 5.1: Material Properties of Silicon Carbonitride

<b>Parameter</b>	<b>Value</b>
Density	2200 kg/m <sup>3</sup> (27)
Young's Modulus	80 GPa (27)
Stress	500 MPa
Specific Heat per Volume ( $c_v$ )	710 J/m <sup>3</sup> K (153)
Linear Coefficient of Thermal Expansion ( $\alpha$ )	$2.3 \times 10^{-6}$ K <sup>-1</sup> (154)
Specific heat capacity (c)	0.4 J/kgK (155)
Thermal conductivity ( $\kappa$ )	3.2 W/mK (153)

The Q factor of some of these devices was also obtained. We mentioned earlier in Chapter 3 that the Q factor is calculated from the FWHM of the resonant frequency peak obtained by the spectrum analyzer. This value was calculated by fitting the resonance graph to a Lorentzian curve in a program called Origin. This program was able to obtain a rough estimate of the Q factor. Only 5 out of the 14 resonators shown in Figure 5.4 were chosen to calculate the Q factor. The resonant frequency graphs obtained for the remaining resonators were too sharp to obtain an accurate reading. More accurate measurements which would allow for a broader peak were required before the Q factor could be calculated more accurately.

Figure 5.5 shows that the Q factors are fairly consistent between 6000 and 8000. One resonator reached a maximum Q factor of approximately 12,450. The frequency and Q factor products (fQ) can be obtained from these values. Q factor products are important for devices which are dominated by thermoe-lastic dissipation (TED). The resonator is close to its maximum allowable Q factor when the fQ product is high (156). The fQ products for these resonators

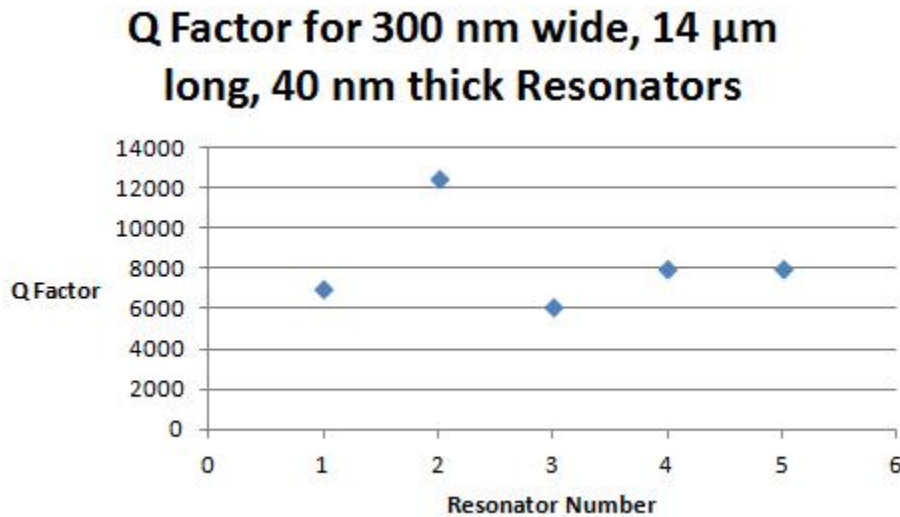


Figure 5.5: The Q factor is calculated for 5 resonators on one array of a sample for the 40 nm thick resonators.

range from  $9.64 \times 10^{10} \text{ s}^{-1}$  to  $2 \times 10^{11} \text{ s}^{-1}$ . There would not be many significant changes over the entire array of resonators fabricated since they are all the same width, thickness, and length. Structures which have much higher Q factors of higher than 100,000 generally have very low resonant frequencies of less than 100 kHz. The  $fQ$  products for these devices will be less than  $10^{10}$  (157; 158).

The theoretical TED Q factor can be calculated for these 40 nm thick resonators using the material parameters in Table 5.1 and the resonant frequencies of the devices using Equation 3.7. The average theoretical TED Q factor for these devices is approximately  $1.3 \times 10^6$ . This value is assuming that the devices are limited entirely by thermal losses. However, there are several different sources of losses which occur for these resonators. Some of these losses can occur through the supports and through the piezoelectric chip used to actuate the devices. This chip would create a large amount of noise which would limit the overall Q factor for these devices. The measured Q factors shown earlier could quite possibly increase by several thousand without this source

of noise. One potential way to remove this source of noise is by actuating the resonator by a laser source. An optical source of actuation will remove these sources of noise and improve the quality factor of the resonators. These additional sources of losses are the primary reason of the discrepancy between the real and theoretical quality factors.

### 5.4.2 Resonance of 70 nm Thick Beams

Another batch of SiCN resonators were made in a similar process to the 40 nm thick beams except the thickness was increased to approximately 70 nm. The resonant frequency and Q factor of the bare resonators were measured. These values were then compared with the 40 nm thick beams to observe if there is any significant difference between the two sets of resonators. The following graph in Figure 5.6 shows the resonant frequency for these 70 nm thick resonators. The peaks shown were taken for nearly all the resonators on one array.

The resonant frequencies for these resonators are clustered together much like the frequencies for 50 nm thick resonators. The average frequency is now at approximately 21.6 MHz. This is about 5 MHz higher than the frequencies for the thinner devices. This is to be expected since increasing the thickness of the beam would lead to slightly higher frequencies according to Equation 3.3, but not the 5 MHz difference seen here. The most likely cause for this huge difference is higher stress values in the SiCN film. An accurate theoretical value of resonant frequency could not be taken because the stress values for these devices were not measured after SiCN deposition. It has been shown by Fischer *et al.* that samples of differing stresses of approximately 120 MPa and the same dimensions will have differing resonant frequencies of 5 MHz or more (159). The difference in resonant frequency for these imprinted resonators is most likely due to varying levels of stress.

The Q factors for some of the devices shown in Figure 5.6 were calculated, and the results are similar to those for resonators with thicknesses of 50 nm.

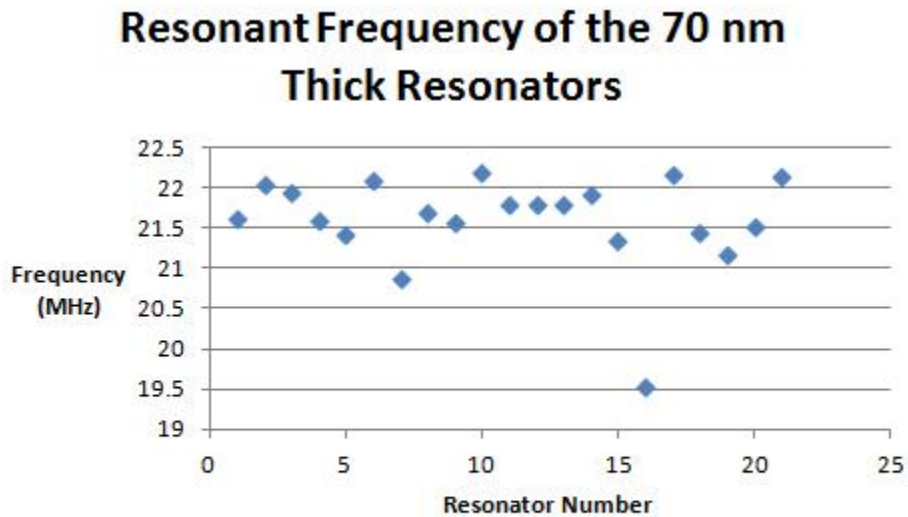


Figure 5.6: The resonant frequency for 70 nm thick beams are measured for an entire array of devices. These devices are 300 nm wide, and 14  $\mu\text{m}$  long.

The Q factors for the 70 nm thick resonators are shown in Figure 5.7. Only a handful of the resonators shown which were measured in Figure 5.6 had their resulting Q factors calculated. The resulting Q factors are within a similar range as the 40 nm thick resonator beams. Several of the 70 nm thick beams have Q factors which are lower than the Q factors for the thinner beams. Some of the peaks which were used for these measurements were quite sharp and not as broad to get an accurate measurement. This could be a reason why the Q factors for these beams are lower. The theoretical Q factor for these devices can be calculated since the stress of the devices does not factor into the equation. The average theoretical  $Q_{TED}$  for the 70 nm thick resonators is 306,610 when using the average frequency of approximately 21.6 MHz. This is much lower than the theoretical Q factor for the 50 nm thick devices which has a value of  $1.3 \times 10^6$ . The overall Q factor will be reduced slightly due to the higher resonant frequencies which were measured. This will result in the sensitivity of these devices being worse than the thinner beams. As mentioned

earlier, the piezoelectric actuation method used for this project would also present other sources of loss which will account for the discrepancies between the real and theoretical values for the 300 nm wide, 14  $\mu$  long and 70 nm thick resonators.

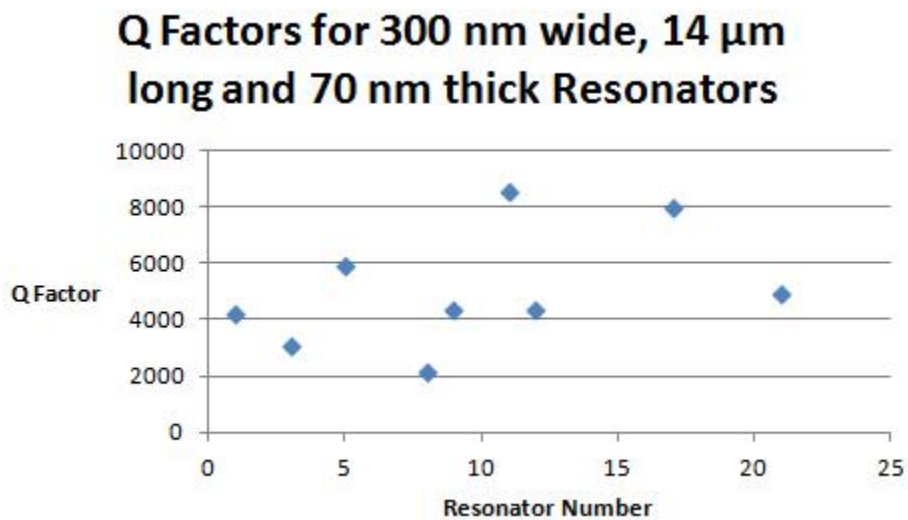


Figure 5.7: The Q factor is calculated for several resonators on one array of a sample for the 70 nm thick resonators.

### 5.4.3 Streptavidin Mass Measurements

The biotin-streptavidin complex was adsorbed onto the surface of the beams after the initial resonance measurements. The samples were treated with bovine serum albumin (BSA) to ensure that no other particles will attach themselves to the beams. BSA acts as a blocker to ensure only streptavidin will bind to the surface. The devices which were tested include the 300 nm wide, 40 nm thick resonators as well as the 70 nm thick resonators. Thinner devices were not tested for these experiments due to the lower imprint yields which were observed. The 300 nm wide resonators have previously been proven to work. The initial tests involved 40 nm thick resonator beams from a different sample

than the ones measured in Figure 5.4. Figure 5.8 shows the bare SiCN resonant frequency measurements which are compared with the resonant frequencies of the beams after both the biotin and streptavidin are adsorbed.

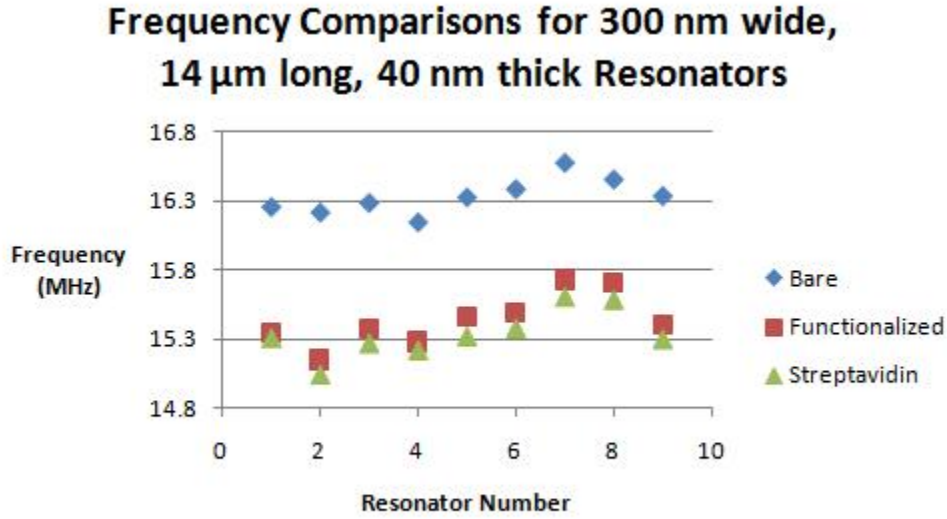


Figure 5.8: Frequency comparisons showing the differences between the bare SiCN resonators, functionalized surface, and streptavidin binding.

The average resonant frequency dropped from 16.4 MHz to approximately 15.3 MHz after streptavidin was attached to the resonators. All of the measured beams showed a consistent decrease in frequency. It is possible to determine the theoretical mass sensitivity of these resonators using Equation 3.1 from the frequency shifts between the streptavidin and functionalized frequencies. This is assuming all the noise is cancelled out from the frequency measurements. The following first-order mass-sensitivity equation is used to determine the masses adsorbed onto the resonators:

$$\frac{\Delta m}{\Delta f} = \frac{2M_{eff}}{f_o} \quad (5.1)$$

The variable  $\Delta m/\Delta f$  is the mass sensitivity, where  $\Delta m$  is the change in mass and  $\Delta f$  is the change in frequency.  $M_{eff}$  is the effective mass of the resonator

and  $f_o$  is the fundamental resonant frequency of the device. Table 5.2 shows the masses for the biotinylated surface and streptavidin for all the resonators in Figure 5.8. The theoretical mass sensitivities calculated using Equation 3.1 are compared with the actual values. The DR values used for the theoretical calculations had approximate values between 9 and 12.

Table 5.2: Mass Sensitivity for 40 nm Thick Resonators

Resonator	Biotin Mass	Streptavidin Mass	Theoretical Sensitivity
1	$30.74 \pm 5.67$ fg	$1.00 \pm 0.38$ fg	$8.37 \pm 3.19$ ag
2	$35.84 \pm 6.61$ fg	$3.68 \pm 0.76$ fg	$4.71 \pm 1.20$ ag
3	$30.68 \pm 5.66$ fg	$3.34 \pm 0.70$ fg	$7.26 \pm 2.33$ ag
4	$29.27 \pm 5.40$ fg	$2.02 \pm 0.50$ fg	$4.03 \pm 1.14$ ag
5	$28.95 \pm 5.34$ fg	$4.66 \pm 0.92$ fg	$14.34 \pm 4.93$ ag
6	$29.83 \pm 5.50$ fg	$3.65 \pm 0.75$ fg	$6.46 \pm 2.13$ ag
7	$27.85 \pm 5.14$ fg	$3.93 \pm 0.79$ fg	$6.42 \pm 2.29$ ag
8	$24.76 \pm 4.57$ fg	$3.96 \pm 0.80$ fg	$15.45 \pm 16.21$ ag
9	$31.26 \pm 5.76$ fg	$3.33 \pm 0.70$ fg	$5.82 \pm 2.14$ ag

These masses which have been detected can also be used to calculate the mass-per-area detected by the beams. The average mass of streptavidin detected for these devices is  $3.28 \pm 1.05$  fg. The mass-per-area for these resonators for the streptavidin detected ranged from  $0.24$  mg/m<sup>2</sup> to  $1.11$  mg/m<sup>2</sup>. The average mass-per-area is  $0.78 \pm 0.25$  mg/m<sup>2</sup> for the streptavidin on the resonators. It is possible to calculate the average surface density of streptavidin the resonators by using the estimated mass density of streptavidin which is  $60,000$  g/mol. The surface density is found to be approximately  $7.83 \times 10^{15}$  m<sup>-2</sup>. This translates to a very sparse monolayer with approximately one streptavidin molecule per  $128$  nm<sup>2</sup>.

A second set of resonators with the same dimensions is exposed to an oversaturated solution of biotin and the normal concentration of streptavidin. This will ensure that the streptavidin will bind with the biotin before it is exposed

to the substrate so that the streptavidin will not bind to the functionalized resonators. The following graph in Figure 5.9 shows the resonant frequencies of this sample for the bare, functionalized, and streptavidin-binding devices.

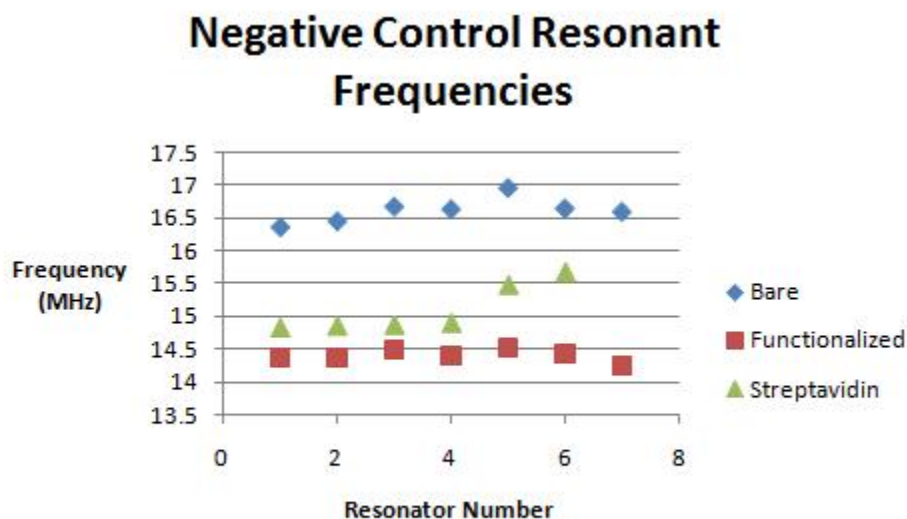


Figure 5.9: A graph showing the frequencies of the 40 nm thick resonators before and after adsorbing the streptavidin with blocked binding sites.

The devices shown in Figure 5.9 were measured a total of three times. The first measurement was after a piranha cleaning. The second measurement was after the initial functionalization and biotin adsorption. The last measurement was after the streptavidin with blocked binding sites was introduced to the resonators. The graph shows that the blocked streptavidin did not attach to the biotin already present on the resonators. The frequencies observed after the streptavidin was introduced are higher than the functionalized resonant frequencies due to the removal of biotin on the surface after the introduction of the streptavidin solution. The overall mass on the resonator will thus have been reduced slightly, so the resonant frequency of the device will have risen.

#### 5.4.4 70 nm Thick Mass Measurements

The 70 nm thick resonators which were fabricated earlier were also used for streptavidin mass measurements to compare with the 40 nm thick beams. This will determine which of the devices are more sensitive to the introduction of biomaterials on the resonators. Figure 5.10 shows the resonant frequencies of these devices before and after the introduction of the biotin-streptavidin complex.

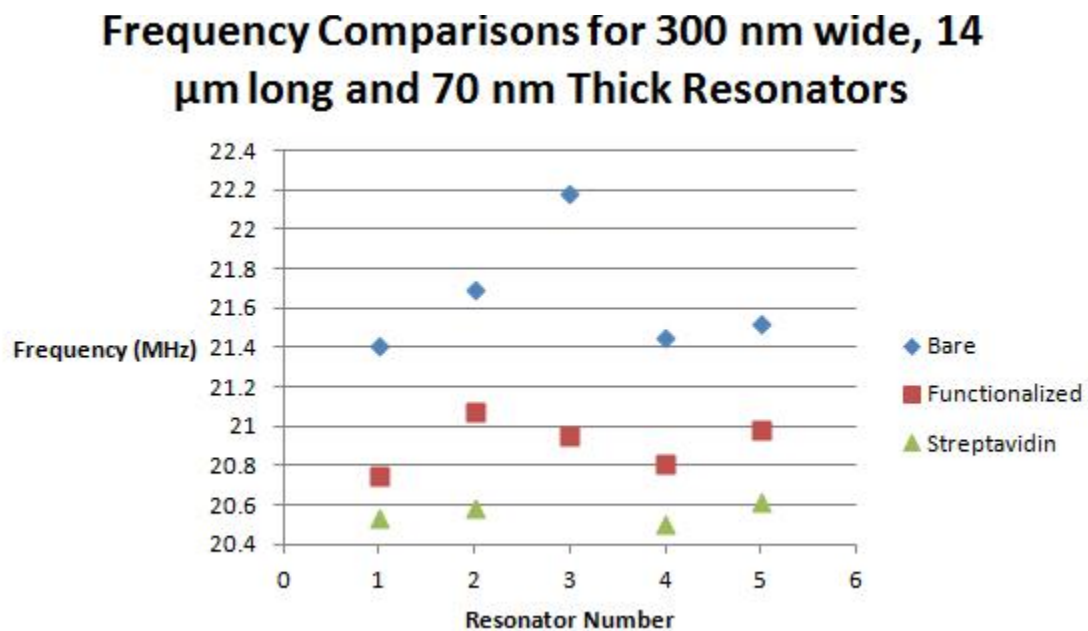


Figure 5.10: A plot showing the frequencies of 70 nm thick resonator devices before and after streptavidin adsorption.

The overall frequency for these devices dropped from an average of 21.65 MHz to 20.56 MHz once the biotin-streptavidin was adsorbed. The overall frequency shift is similar to that of the 40 nm thick devices which is approximately 1 MHz. The mass sensitivity for these devices is shown in Table 5.3. This table shows the masses of biotin and streptavidin detected, as well as the theoretical mass sensitivity. The third resonator which was measured is ignored since we were unable to detect a signal after streptavidin was adsorbed.

Table 5.3: Mass Sensitivity for 70 nm Thick Resonators

Resonator	Biotin Mass	Streptavidin Mass	Theoretical Sensitivity
1	$29.31 \pm 3.21$ fg	$9.33 \pm 1.32$ fg	$22.80 \pm 11.72$ ag
2	$27.18 \pm 2.99$ fg	$21.04 \pm 2.38$ fg	$85.53 \pm 95.78$ ag
4	$28.37 \pm 3.11$ fg	$13.74 \pm 1.70$ fg	—
5	$23.86 \pm 2.66$ fg	$15.91 \pm 1.89$ fg	—

There is a clear difference between the streptavidin masses detected for the different thicknesses in resonators. Nearly triple the amount of streptavidin is found on the 70 nm thick devices than on the 40 nm thick resonators. The theoretical mass sensitivity is much higher as well. This is to be expected since thicker resonators will be less sensitive to masses adsorbed onto the surface. The average mass on these resonators is approximately  $15.0 \pm 4.22$  fg and the average mass-per-area is  $3.57 \pm 1.00$  mg/m<sup>2</sup>. The density of streptavidin molecules on the surface is approximately  $3.58 \times 10^{16}$  m<sup>-2</sup>. This corresponds to one streptavidin molecule per 28 nm<sup>2</sup>. This is approximately one monolayer on the surface of the beams. Figure 5.11 shows that the theoretical sensitivities calculated for the 70 nm thick devices may not be very accurate. This is due to the sharp peaks obtained for the 70 nm thick resonators rather than the broader peaks for the 50 nm thick devices. The 70 nm thick measurements were performed first and only the resonant frequency was observed. The overall bandwidth was not measured so an accurate measurement of the Q factor could not be obtained. The Q factors for these devices were roughly estimated from these graphs. It is for this reason that the theoretical sensitivity for the last two resonators were not measured due to insufficient data to get an accurate Q factor reading.

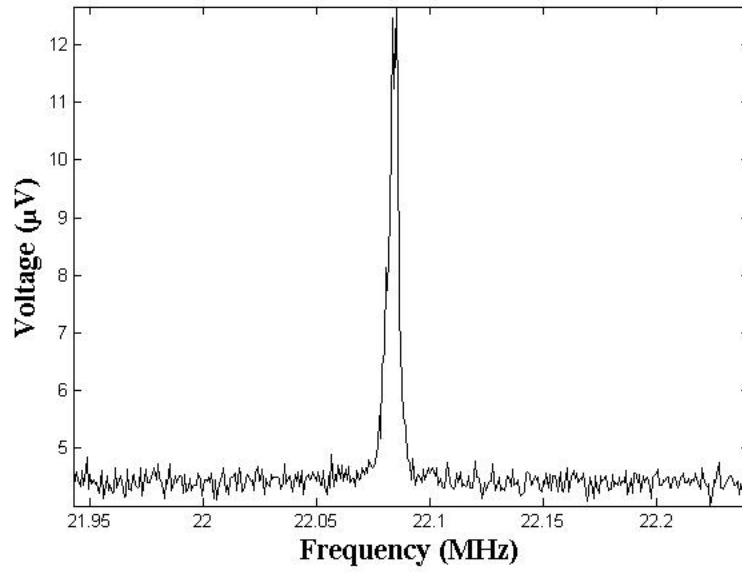
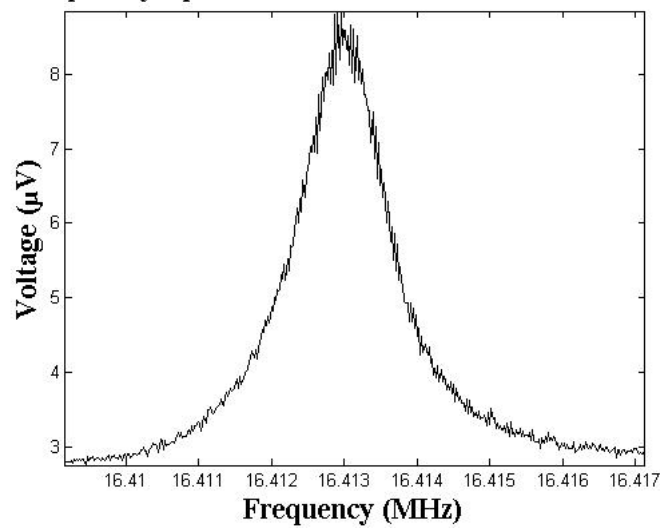
**Frequency Spectrum for a 70 nm Thick Resonator****Frequency Spectrum for a 40 nm Thick Resonator**

Figure 5.11: Frequency spectra for the 70 nm thick (top) and 50 nm thick (bottom) resonators.

## 5.5 Multiple Experiments per Sample

A separate experiment was conducted where a small droplet of streptavidin was deposited upon each of the arrays on the sample instead of submerging the entire sample into a solution of streptavidin. This experiment was to conclude whether multiple experiments could be performed on a single chip rather than on multiple chips. This can save some time and materials when fabricating samples. The devices used for this experiment were 300 nm wide, 14  $\mu\text{m}$  long, and 40 nm thick. The droplets which were chosen contained a normal concentration of streptavidin and a saturated solution of biotin-streptavidin. The resonance measurements for these solutions are predictable so it will be easier to tell if the experiment was successful. The solutions were made in 25  $\mu\text{L}$  drops, but only 2 - 4  $\mu\text{L}$  of the created solution were used because of the close proximity of the arrays to each other. The results of this experiment are shown in Figure 5.12.

It is clear to see that there was extra mass being deposited upon the beams for both the normal concentration and the saturated streptavidin arrays. The frequency difference between the functionalized and the streptavidin measurements is 0.265 MHz for the normal concentration and 0.278 MHz for the saturated concentration. This means that there was streptavidin adsorption for both arrays that were tested. The reason that this experiment did not work correctly is possibly due to the fact that the droplets evaporated quickly in about 10 - 20 minutes. The samples which were submerged in streptavidin were left in the solution for an hour before being removed and washed. It is possible that any material left behind attached itself to the resonator beams once the droplets evaporated which could not be removed by washing. This would explain the similar frequency difference for both samples. Another possibility is that the biotin used in the control experiment was not enough to ensure that the streptavidin was bound to it. We already stated that only 2 - 4  $\mu\text{L}$ 's were drawn from a 25  $\mu\text{L}$  drop and deposited upon each array. The arrays were about 1 mm apart from each other, so larger drops could not be

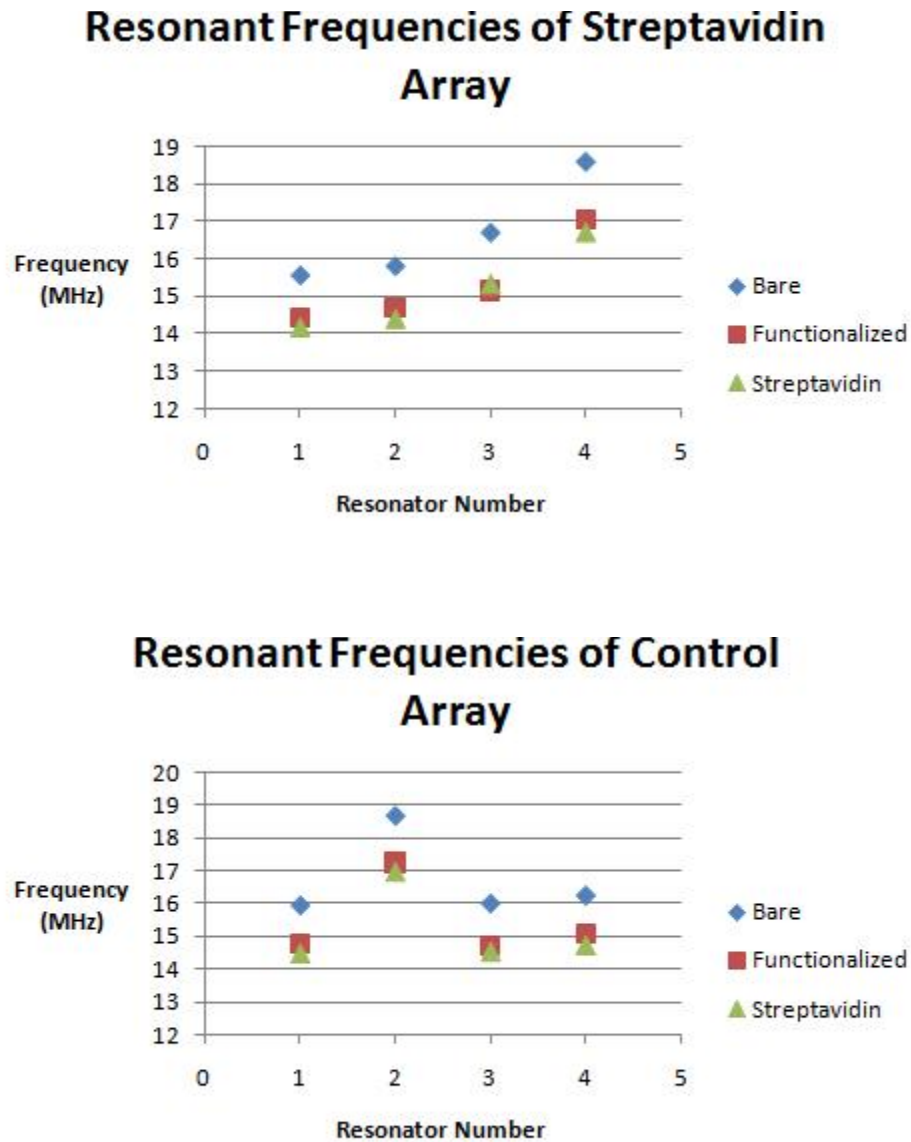


Figure 5.12: Frequency plot showing the positive, normal concentration exposure (top) and the controlled saturation exposure (bottom).

used. We could not create a streptavidin solution using only 2 - 4  $\mu\text{L}$  because it would require using approximately 0.02  $\mu\text{L}$  of streptavidin which is very difficult to measure. It would be possible to use the larger drops if the distance

between the arrays was increased to 1 cm or more. This would ensure that the drops would not evaporate as quickly.

## 5.6 Conclusions

The adsorption of biotin-streptavidin was successfully completed on imprinted resonators with 40 and 70 nm thicknesses. The average resonant frequencies for both devices were measured before and after biotin was adsorbed in an APTES solution. The average frequency for the 40 nm thick devices was measured to be 16.4 MHz. The average frequency for the 70 nm thick resonators was measured to be 21.6 MHz. These frequencies dropped to an average of 15.3 MHz and 20.56 MHz for the 40 nm and 70 nm thick beams respectively after streptavidin was deposited.

The mass of streptavidin upon the 40 nm thick devices was calculated to be approximately  $3.28 \pm 1.05$  fg with an average mass-per-area of  $0.78 \pm 0.25$  mg/m<sup>2</sup>. This corresponds to approximately one streptavidin molecule per 128 nm<sup>2</sup>. A negative control experiment was run which found that there was no additional masses adsorbing onto the surface of the resonators meaning only the streptavidin contributed to the attached masses. The mass of streptavidin upon the 70 nm thick devices was calculated to be approximately  $15.0 \pm 4.22$  fg with an average mass-per-area of  $3.57 \pm 1.00$  mg/m<sup>2</sup>. This corresponds to one streptavidin molecule per 28 nm<sup>2</sup>. These values serve as a good estimate of the masses found on the 70 nm thick resonators even though the peaks obtained for these beams were not ideal.

The experiment to deposit streptavidin upon the resonators via droplets rather than submersion of the entire sample did not work as expected. This experiment did show that this technique will work with further improvements and experimentation. Further experiments can include depositing the droplets in a humid environment to ensure that the droplets will not evaporate as quickly. Increasing the amount of biotin for the control may also work to ensure all of the streptavidin will be blocked.

---

---

## CHAPTER 6

---

### Conclusions

#### 6.1 Summary

Resonator devices have been successfully created over the course of this project using nanoimprint lithography. These devices have been successfully tested for mass sensing purposes down to femtogram detection. It has been proven to be possible to create beams using NIL with widths down to 120 nm using a PMMA 495/LOR 3A bilayer resist technique. The ideal imprint parameters for these devices included a temperature of 190 °C, a pressure of 200 psi, and an imprint hold time of 2 minutes. This resist allowed an imprint yield approaching 100% and the imprinted beams could be utilized for mass sensing purposes. The specially designed resist mr-I 8030 E was also used successfully using the same imprint conditions to create resonator beams with a total yield approaching 100%.

Silicon carbonitride was used for the resonators which were fabricated with thicknesses between 40 and 70 nm. This material has been used previously within our group with great results and the same process was used to create these devices. This process yielded a material with tensile stress values ranging from approximately 300 MPa to 500 MPa. A 32% potassium hydroxide solution was used to release the resonators for resonance measurements. The

resonance frequencies for the 300 nm wide imprinted resonators resulted in average values of 16.4 MHz for the 40 nm thick devices and 21.6 MHz for the 70 nm thick devices. The quality factors for the 40 nm thick devices were measured to have an average of approximately 8,290, with the highest Q factor being 12,500.

A biotin-streptavidin complex was used to determine if the imprinted resonators could successfully detect biological compounds on the surface. An organosilane monolayer called APTES was deposited using wet chemistry to attach biotin to the surface of the resonators. Biotin was used because it is an effective linking molecule for streptavidin detection purposes. The overall resonant frequency dropped from the bare SiCN and functionalized measurements after streptavidin was added for all devices tested. This shows that streptavidin did successfully bind with the resonators. The average mass for the 40 nm wide resonators tested was found to be  $3.28 \pm 1.05$  fg, with a mass-per-area of  $0.78 \pm 0.25$  mg/m<sup>2</sup>. The surface density for these devices was calculated to be  $7.83 \times 10^{15}$  m<sup>-2</sup>. This corresponds to approximately one streptavidin molecule per 128 nm<sup>2</sup> on the surface of the resonators. The average mass for the 70 nm wide resonators was found to be  $15.0 \pm 4.22$  fg, with a mass-per-area of  $3.57 \pm 1.00$  mg/m<sup>2</sup>. This corresponds to a surface density of  $3.57 \times 10^{16}$ . This means there is one streptavidin molecule per 28 nm<sup>2</sup> for these devices. It was also proven through a negative control experiment which was oversaturated with biotin that there was no non-specific binding to the biotin. Only the streptavidin protein was responsible for the decrease in resonant frequency.

It has therefore been shown that nanoimprint lithography is a successful fabrication technique to produce resonating devices. The capabilities for mass detection for imprinted nanomechanical resonators into the femtogram range has been established.

## 6.2 Recommended Work

There are several directions to go to improve upon the work completed in this project. The smallest resonator imprinted was approximately 120 nm. It is possible to imprint smaller features that are below 100 nm. Anisotropic etch recipes should be used to get these smaller imprints instead of the isotropic etches used for this project. Lower pressures should be used to minimize the amount of isotropic etching occurring. It would be ideal to use a system that is capable of purely anisotropic etches. The resists which were used for this project such as mr-I 8030 E are suitable for creating devices which are less than 100 nm in width.

Further improvements must also be made for the multiple experiment per sample sensor mentioned in the previous chapter. This technique can work if the sample is kept in a humid environment to prevent evaporation from occurring. This will allow for the streptavidin to bind to the resonators more naturally. It will also allow for the saturated control experiment to work correctly. Adding more biotin to the saturated biotin-streptavidin solution may also allow for non-specific binding to occur. Using samples which have arrays that are spaced further apart would allow for larger drops to be used which would improve the chances of success for this experiment. Further experiments using this system can include using other proteins which can bind to biotin such as neutravidin. This will prove that multiple biomaterials can be sensed on different resonators on the same chip. Using this technique would be very useful in research involving lab-on-a-chip technologies.

# Bibliography

- [1] R. P. Feynman, “There’s Plenty of Room at the Bottom,” *Engineering Science*, vol. 1, no. 1, pp. 22–36, 1959.
- [2] S. D. Senturia, *Microsystem Design*. Kluwer Academic Publishers, 2001.
- [3] G. Description and F. B. Diagram, “Digital Accelerometer,” *Data Sheet*, 2010.
- [4] G. Description, E. Circuit, and P. Dimensions, “Surface Mount Basic Pressure Sensors,” *Sensors (Peterborough, NH)*, pp. 5–7.
- [5] S. Tadigadapa and S. Massoud-Ansari, “Applications of High-Performance MEMS Pressure Sensors Based on Dissolved Wafer Process,” *Sensors (Peterborough, NH)*.
- [6] S. A. R. Adc, “8-Channel , I 2 C , 12-Bit SAR ADC with Temperature Sensor,” *Data Sheet*, 2011.
- [7] G. Binnig, C. F. Quate, and C. Gerber, “Atomic Force Microscope,” *Physical Review Letters*, vol. 56, no. 9, pp. 930–933, 1986.
- [8] D. Rugar, “Atomic Force Microscopy,” *Physics Today*, vol. 41, no. 1, pp. 3–49, 1990.
- [9] A. Checco, Y. Cai, O. Gang, and B. M. Ocko, “High resolution non-contact AFM imaging of liquids condensed onto chemically nanopatterned surfaces.,” *Ultramicroscopy*, vol. 106, no. 8-9, pp. 703–8, 2006.

- [10] L. Zitzler, S. Herminghaus, and F. Mugele, “Capillary forces in tapping mode atomic force microscopy,” *Applied Physics Letters*, vol. 64, no. 15, pp. 1–8, 1994.
- [11] C. A. J. Putman, K. O. Van Der Werf, B. G. D. Grooth, N. F. V. Hulst, and J. Greve, “Tapping mode atomic force microscopy in liquid,” *Applied Physics Letters*, vol. 64, no. 18, pp. 2454–2456, 1994.
- [12] G. Tosolini, G. Villanueva, F. Perez-Murano, and J. Bausells, “Silicon microcantilevers with MOSFET detection,” *Microelectronic Engineering*, vol. 87, no. 5-8, pp. 1245–1247, 2010.
- [13] B. L. Weeks, J. Camarero, A. Noy, A. E. Miller, L. Stanker, and J. J. De Yoreo, “A microcantilever-based pathogen detector.,” *Scanning*, vol. 25, no. 6, pp. 297–299, 2003.
- [14] I. C. Nelson, D. Banerjee, W. J. Rogers, and M. S. Mannan, “Detection of explosives using heated microcantilever sensors,” *Proceedings of SPIE*, vol. 6223, pp. 62230O–62230O–8, 2006.
- [15] M. Alvarez and L. M. Lechuga, “Microcantilever-based platforms as biosensing tools.,” *The Analyst*, vol. 135, no. 5, pp. 827–836, 2010.
- [16] J. Zhang and H.-F. Ji, “An anti E. coli O157:H7 antibody-immobilized microcantilever for the detection of Escherichia coli (E. coli).,” *Analytical sciences the international journal of the Japan Society for Analytical Chemistry*, vol. 20, no. 4, pp. 585–587, 2004.
- [17] B. Ilic, D. Czaplewski, M. Zalalutdinov, H. G. Craighead, P. Neuzil, C. Campagnolo, and C. Batt, “Single cell detection with micromechanical oscillators,” *Journal of Vacuum Science and Technology B: Microelectronics and Nanometer Structures*, vol. 19, no. 6, p. 2825, 2001.
- [18] K. L. Ekinici, X. M. H. Huang, and M. L. Roukes, “Ultrasensitive nanoelectromechanical mass detection,” *Applied Physics Letters*, vol. 84, no. 22, p. 4469, 2004.

- [19] L. Fischer, V. Wright, C. Guthy, N. Yang, M. McDermott, J. Buriak, and S. Evoy, "Specific detection of proteins using nanomechanical resonators," *Sensors and Actuators B: Chemical*, vol. 134, pp. 613–617, Sept. 2008.
- [20] Y. T. Yang, C. Callegari, X. L. Feng, K. L. Ekinici, and M. L. Roukes, "Zeptogram-scale nanomechanical mass sensing.," *Nano letters*, vol. 6, pp. 583–6, Apr. 2006.
- [21] K. L. Ekinici, "Ultimate limits to inertial mass sensing based upon nanoelectromechanical systems," *Journal of Applied Physics*, vol. 95, no. 5, p. 2682, 2004.
- [22] M. Liu, J. Zhu, S. X. Jia, M. Zhuo, L. Lu, and Q. C. Gong, "Fabrication of Nanomechanical Resonators in Silicon Nitride," *Advanced Materials Research*, vol. 60-61, pp. 228–231, 2009.
- [23] C. Forster, V. Cimalla, K. Bruckner, M. Hein, J. Pezoldt, and O. Ambacher, "Micro-electromechanical systems based on 3C-SiC/Si heterostructures," *Materials Science and Engineering: C*, vol. 25, pp. 804–808, Dec. 2005.
- [24] D. a. Czaplewski, J. P. Sullivan, T. a. Friedmann, D. W. Carr, B. E. N. Keeler, and J. R. Wendt, "Mechanical dissipation in tetrahedral amorphous carbon," *Journal of Applied Physics*, vol. 97, no. 2, p. 023517, 2005.
- [25] B. L. Boyce, J. M. Grazier, T. E. Buchheit, and M. J. Shaw, "Strength Distributions in Polycrystalline Silicon MEMS," *Journal Of Microelectromechanical Systems*, vol. 16, no. 2, pp. 179–190, 2007.
- [26] D. W. Carr, S. Evoy, L. Sekaric, H. G. Craighead, and J. M. Parpia, "Measurement of mechanical resonance and losses in nanometer scale silicon wires," *Applied Physics Letters*, vol. 75, no. 7, pp. 920–922, 1999.

- [27] C. Guthy, R. M. Das, B. Drobot, and S. Evoy, "Resonant characteristics of ultranarrow SiCN nanomechanical resonators," *Journal of Applied Physics*, vol. 108, no. 1, p. 014306, 2010.
- [28] D. C. Miller, K. Gall, and C. R. Stoldt, "Galvanic Corrosion of Miniaturized Polysilicon Structures," *Electrochemical and Solid-State Letters*, vol. 8, no. 9, p. G223, 2005.
- [29] D. C. Miller, B. L. Boyce, K. Gall, and C. R. Stoldt, "Galvanic corrosion induced degradation of tensile properties in micromachined polycrystalline silicon," *Applied Physics Letters*, vol. 90, no. 19, p. 191902, 2007.
- [30] D. C. Miller, B. L. Boyce, P. G. Kotula, and C. R. Stoldt, "Connections between morphological and mechanical evolution during galvanic corrosion of micromachined polycrystalline and monocrystalline silicon," *Journal of Applied Physics*, vol. 103, no. 12, p. 123518, 2008.
- [31] L. Sekaric, D. W. Carr, S. Evoy, J. M. Parpia, and H. G. Craighead, "Nanomechanical resonant structures in silicon nitride : fabrication , operation and dissipation issues," *Sensors And Actuators*, vol. 101, pp. 215–219, 2002.
- [32] L. M. Fischer, N. Wilding, M. Gel, and S. Evoy, "Low-stress silicon carbonitride for the machining of high-frequency nanomechanical resonators," *Journal of Vacuum Science & Technology B: Microelectronics and Nanometer Structures*, vol. 25, no. 1, p. 33, 2007.
- [33] R. Levy, "A comparative study of plasma enhanced chemically vapor deposited Si<sub>3</sub>O<sub>2</sub>H and Si<sub>3</sub>N<sub>2</sub>C<sub>2</sub>H films using the environmentally benign precursor diethylsilane," *Materials Letters*, vol. 54, pp. 102–107, May 2002.
- [34] H. G. Craighead, R. E. Howard, L. D. Jackel, and P. M. Mankiewich, "10-nm linewidth electron beam lithography on GaAs," *Applied Physics Letters*, vol. 42, no. 1, pp. 38–40, 1983.

- [35] I. B. Baek, J. H. Yang, W. J. Cho, C. G. Ahn, K. Im, and S. Lee, "Electron beam lithography patterning of sub-10 nm line using hydrogen silsesquioxane for nanoscale device applications," *Journal of Vacuum Science and Technology B: Microelectronics and Nanometer Structures*, vol. 23, no. 6, pp. 3120–3123, 2005.
- [36] D. Lam, D. Liu, T. Prescop, and W. Drive, "E-beam Direct Write (EBDW) as Complementary Lithography," *Production*, 2010.
- [37] R. D. Piner, J. Zhu, F. Xu, S. Hong, and C. A. Mirkin, "'Dip-Pen' Nanolithography," *Science*, vol. 283, pp. 661–663, 1999.
- [38] C. A. Mirkin, "The power of the pen: development of massively parallel dip-pen nanolithography.," *ACS nano*, vol. 1, no. 2, pp. 79–83, 2007.
- [39] C. Sotomayor Torres, *Nanoimprint lithography: an alternative nanofabrication approach*. PhD thesis, Jan. 2003.
- [40] M. Beck, M. Graczyk, I. Maximov, E.-L. Same, T. Ling, and L. Montelius, "Improving nanoimprint lithography stamps for the 10 nm features," *Proceedings of the 2001 1st IEEE Conference on Nanotechnology. IEEE-NANO 2001 (Cat. No.01EX516)*, pp. 17–22, 2001.
- [41] G. Luo, I. Maximov, D. Adolph, M. Graczyk, P. Carlberg, S. Ghatnekar-Nilsson, D. Hessman, T. Zhu, Z. Liu, H. Q. Xu, and L. Montelius, "Nanoimprint lithography for the fabrication of interdigitated cantilever arrays," *Nanotechnology*, vol. 17, pp. 1906–1910, Apr. 2006.
- [42] C. C. Huang and K. L. Ekinici, "Fabrication of freely suspended nanostructures by nanoimprint lithography," *Applied Physics Letters*, vol. 88, no. 9, p. 093110, 2006.
- [43] P. R. Krauss and S. Y. Chou, "Sub-10 nm imprint lithography and applications," *1997 55th Annual Device Research Conference Digest*, vol. 15, no. June, pp. 90–91, 1997.

- [44] S. Y. Chou, P. R. Krauss, and P. J. Renstrom, "Imprint of sub-25 nm vias and trenches in polymers," *Applied Physics Letters*, vol. 67, no. 21, p. 3114, 1995.
- [45] P. R. Krauss and S. Y. Chou, "Sub-10 nm Imprint Lithography and Applications," vol. 272, no. 612, pp. 90–91, 1996.
- [46] Y. Hirai, S. Yoshida, and N. Takagi, "Defect analysis in thermal nanoimprint lithography," *Journal of Vacuum Science & Technology B: Microelectronics and Nanometer Structures*, vol. 21, no. 6, p. 2765, 2003.
- [47] L. Guo, "Nanoimprint Lithography: Methods and Material Requirements," *Advanced Materials*, vol. 19, pp. 495–513, Feb. 2007.
- [48] C. Gourgon, N. Chaix, H. Schiff, M. Tormen, S. Landis, C. M. Sotomayor Torres, a. Kristensen, R. H. Pedersen, M. B. Christiansen, I. Fernandez-Cuesta, D. Mendels, L. Montelius, and T. Haatainen, "Benchmarking of 50nm features in thermal nanoimprint," *Journal of Vacuum Science & Technology B: Microelectronics and Nanometer Structures*, vol. 25, no. 6, p. 2373, 2007.
- [49] G. Xie, J. Zhang, Y. Zhang, Y. Zhang, T. Zhu, and Z. Liu, "Fabrication of metal suspending nanostructures by nanoimprint lithography (NIL) and isotropic reactive ion etching (RIE)," *Science in China Series E: Technological Sciences*, vol. 52, pp. 1181–1186, Jan. 2009.
- [50] P. Carlberg, *Development of Nanoimprint Lithography for Applications in Electronics , Photonics and Life-sciences*. PhD thesis, 2007.
- [51] M. Fukuhara, H. Ono, T. Hirasawa, M. Otaguchi, N. Sakai, J. Mizuno, and S. Shoji, "UV Nanoimprint Lithography and Its Application for Nanodevices," *Journal of Photopolymer Science and Technology*, vol. 20, no. 4, pp. 549–554, 2007.
- [52] S. Gilles, M. Meier, M. Prömpers, A. V. D. Hart, C. Kügeler, A. Offenhäuser, and D. Mayer, "UV nanoimprint lithography with rigid poly-

- mer molds,” *Microelectronic Engineering*, vol. 86, pp. 661–664, Apr. 2009.
- [53] M. Bender, A. Fuchs, U. Plachetka, and H. Kurz, “Status and prospects of UV-Nanoimprint technology,” *Microelectronic Engineering*, vol. 83, no. 4-9, pp. 827–830, 2006.
- [54] M. Colburn, T. Bailey, B. Choi, and J. Ekerdt, “Development and advantages of step-and-flash lithography,” *Solid State T*, vol. 46, no. 7, pp. 67–76, 2001.
- [55] H. Tan, A. Gilbertson, and S. Y. Chou, “Roller nanoimprint lithography,” *Journal of Vacuum Science and Technology B: Microelectronics and Nanometer Structures*, vol. 16, no. 6, p. 3926, 1998.
- [56] C. Stuart and Y. Chen, “Roll in and roll out: a path to high-throughput nanoimprint lithography,” *ACS nano*, vol. 3, pp. 2062–4, Aug. 2009.
- [57] M. Kurihara, “Status and challenges of template fabrication process for UV nanoimprint lithography,” *Journal Of Photopolymer Science And Technology*, vol. 20, no. 4, pp. 563–567, 2007.
- [58] K. Pfeiffer, M. Fink, G. Ahrens, G. Gruetzner, F. Reuther, J. Seekamp, S. Zankovych, C. M. S. Torres, I. Maximov, M. Beck, M. Graczyk, L. Montelius, H. Schulz, H. C. Scheer, and F. Steingrueber, “Polymer stamps for nanoimprinting,” vol. 61-2, pp. 393–398, 2002.
- [59] S. Park, H. Schiff, C. Padeste, and B. Schnyder, “Anti-adhesive layers on nickel stamps for nanoimprint lithography,” *Microelectronic Engineering*, vol. 74, pp. 196–201, 2004.
- [60] L. Tao, S. Ramachandran, C. T. Nelson, M. Lin, L. J. Overzet, M. Goeckner, G. Lee, C. G. Willson, W. Wu, and W. Hu, “Durable diamond-like carbon templates for UV nanoimprint lithography,” *Nanotechnology*, vol. 19, no. 10, p. 105302, 2008.

- [61] J.-H. Jeong, K.-D. Kim, Y.-S. Sim, D.-G. Choi, E.-S. Lee, S.-H. Park, T.-W. Lim, and D.-Y. Yang, "UV nanoimprint lithography using a diamond-like carbon stamp," *Proceedings of SPIE*, vol. 6151, pp. 61512J–61512J–8, 2006.
- [62] I. Maximov, "Fabrication of Si-based nanoimprint stamps with sub-20 nm features," *Microelectronic Engineering*, vol. 61-62, pp. 449–454, 2002.
- [63] S. Okazaki, "Resolution limits of optical lithography," *Journal of Vacuum Science and Technology B: Microelectronics and Nanometer Structures*, vol. 9, no. 6, pp. 2829–2833, 1991.
- [64] C. Tarrío, S. Grantham, M. B. Squires, R. E. Vest, and T. B. Lucaertorto, "Extreme-Ultraviolet Lithography," *Journal Of Research Of The National Institute Of Standards And Technology*, vol. 108, no. 4, pp. 267–273, 2003.
- [65] B. Wu and A. Kumar, "Extreme ultraviolet lithography: A review," *Journal of Vacuum Science and Technology B: Microelectronics and Nanometer Structures*, vol. 25, no. 6, p. 1743, 2007.
- [66] C. L. Cheung, R. J. Nikolic, C. E. Reinhardt, and T. F. Wang, "Fabrication of nanopillars by nanosphere lithography," *Nanotechnology*, vol. 17, no. 5, pp. 1339–1343, 2006.
- [67] C. W. Kuo, J. Y. Shiu, Y. H. Cho, and P. Chen, "Fabrication of nanoimprint stamps by nanosphere lithography," *Advanced Materials*, vol. 776, no. 20, pp. 67–72 284, 2003.
- [68] M. D. Austin, W. Zhang, H. Ge, D. Wasserman, S. A. Lyon, and S. Y. Chou, "6 Nm Half-Pitch Lines and 0.04 m<sup>2</sup> Static Random Access Memory Patterns By Nanoimprint Lithography," *Nanotechnology*, vol. 16, no. 8, pp. 1058–1061, 2005.
- [69] N. Chaix, C. Gourgon, S. Landis, C. Perret, M. Fink, and F. Reuther, "Influence of the molecular weight and imprint conditions on the forma-

- tion of capillary bridges in nanoimprint lithography,” *Nanotechnology*, vol. 17, no. 16, pp. 4082–4087, 2006.
- [70] C. Gourgon, C. Perret, G. Micouin, F. Lazzarino, J. H. Tortai, and O. Joubert, “Influence of pattern density in nanoimprint lithography,” pp. 98–105, 2003.
- [71] H. Schulz, “Mask fabrication by nanoimprint lithography using antisticking layers,” *Proceedings of SPIE*, vol. 3996, pp. 244–249, 2000.
- [72] C. Finder, “Fluorescence microscopy for quality control in nanoimprint lithography,” *Microelectronic Engineering*, vol. 67-68, pp. 623–628, 2003.
- [73] H.-C. Scheer, N. Bogdanski, M. Wissen, and S. Möllenbeck, “Imprintability of polymers for thermal nanoimprint,” *Microelectronic Engineering*, vol. 85, pp. 890–896, May 2008.
- [74] B. Cui, L. Clime, K. Li, and T. Veres, “Fabrication of large area nanoprism arrays and their application for surface enhanced Raman spectroscopy,” *Nanotechnology*, vol. 19, p. 145302, Apr. 2008.
- [75] P. Carlberg, “Lift-off process for nanoimprint lithography,” *Microelectronic Engineering*, vol. 67-68, pp. 203–207, June 2003.
- [76] F. Buyukserin, M. Aryal, J. Gao, and W. Hu, “Fabrication of polymeric nanorods using bilayer nanoimprint lithography,” *Small (Weinheim an der Bergstrasse, Germany)*, vol. 5, pp. 1632–6, July 2009.
- [77] Microresist Technology, “Thermoplastic Polymers for Nanoimprint Lithography,” *Data Sheet*, pp. 65762192–65762192.
- [78] F. Gottschalch, “Polymer issues in nanoimprinting technique,” *Solid-State Electronics*, vol. 43, pp. 1079–1083, June 1999.
- [79] M. Bender, M. Otto, B. Hadam, B. Vratzov, B. Spangenberg, and H. Kurz, “Fabrication of nanostructures using a UV-based imprint technique,” *Microelectronic Engineering*, vol. 53, pp. 233–236, June 2000.

- [80] D. Lyebedyev, "Mask definition by nanoimprint lithography," *Proceedings of SPIE*, vol. 4349, pp. 82–85, 2001.
- [81] H. Scheer, N. Bogdanski, M. Wissen, T. Konishi, and Y. Hirai, "Profile evolution during thermal nanoimprint," *Microelectronic Engineering*, vol. 83, pp. 843–846, Apr. 2006.
- [82] H. Schiff, L. J. Heyderman, M. A. D. Maur, and J. Gobrecht, "Pattern formation in hot embossing of thin polymer films," *Nanotechnology*, vol. 12, pp. 173–177, 2001.
- [83] K.-S. Kim, J.-H. Kim, H.-J. Lee, and S.-R. Lee, "Tribology issues in nanoimprint lithography," *Journal of Mechanical Science and Technology*, vol. 24, pp. 5–12, Mar. 2010.
- [84] D. Ramos, J. Tamayo, J. Mertens, M. Calleja, and A. Zaballos, "Origin of the response of nanomechanical resonators to bacteria adsorption," *Journal of Applied Physics*, vol. 100, no. 10, p. 106105, 2006.
- [85] N. V. Lavrik, M. J. Sepaniak, and P. G. Datskos, "Cantilever transducers as a platform for chemical and biological sensors," *Review of Scientific Instruments*, vol. 75, no. 7, p. 2229, 2004.
- [86] K. Jensen, K. Kim, and A. Zettl, "An atomic-resolution nanomechanical mass sensor.," 2008.
- [87] W. J. Venstra and H. S. J. Van Der Zant, "Efficient readout of micromechanical resonator arrays in ambient conditions," *Applied Physics Letters*, vol. 93, no. 23, p. 4, 2009.
- [88] S. C. Jun, J. H. Cho, W. K. Kim, Y. M. Jung, S. Hwang, S. Shin, J. Y. Kang, J. Shin, I. Song, J.-Y. Choi, S. Lee, and J. M. Kim, "Resonance Properties of 3C-SiC Nanoelectromechanical Resonator in Room-Temperature Magnetomotive Transduction," *Electron Device Letters*, vol. 30, no. 10, pp. 1042–1044, 2009.

- [89] C. Förster, V. Cimalla, V. Lebedev, J. Pezoldt, K. Brueckner, R. Stephan, M. Hein, E. Aperathitis, and O. Ambacher, “Group III-nitride and SiC based micro- and nanoelectromechanical resonators for sensor applications,” *Physica Status Solidi Applied Research*, vol. 203, no. 7, pp. 1829–1833, 2006.
- [90] W. J. Venstra, H. J. R. Westra, K. B. Gavan, and H. S. J. Van Der Zant, “Magnetomotive drive and detection of clamped-clamped mechanical resonators in water,” *Applied Physics Letters*, vol. 95, no. 26, p. 4, 2010.
- [91] R. Raiteri, “Micromechanical cantilever-based biosensors,” *Sensors and Actuators B: Chemical*, vol. 79, no. 2-3, pp. 115–126, 2001.
- [92] R. Berger, H. P. Lang, C. Gerber, J. K. Gimzewski, J. H. Fabian, L. Scandella, E. Meyer, and H. Guntherodt, “Micromechanical thermogravimetry,” *Chemical Physics Letters*, vol. 294, no. 4-5, pp. 363–369, 1998.
- [93] L. Jiang, R. Cheung, J. Hedley, M. Hassan, A. J. Harris, J. S. Burdess, M. Mehregany, and C. Zorman, “SiC cantilever resonators with electrothermal actuation,” 2006.
- [94] D. Lange, “Electromagnetic actuation and MOS-transistor sensing for CMOS-integrated micromechanical resonators,” *Sensors and Actuators A: Physical*, vol. 103, no. 1-2, pp. 150–155, 2003.
- [95] J. Arcamone, E. Colinet, A. Niel, and E. Ollier, “Efficient capacitive transduction of high-frequency micromechanical resonators by intrinsic cancellation of parasitic feedthrough capacitances,” *Applied Physics Letters*, vol. 97, no. 4, p. 43505, 2010.
- [96] T. Lalinsky, E. Burian, M. Drzik, S. Hascik, Z. Mozolova, and J. Kuzmik, “Thermal actuation of a GaAs cantilever beam,” *Journal of Micromechanics and Microengineering*, vol. 10, no. 2, pp. 293–298, 2000.

- [97] B. Ilic, Y. Yang, and H. G. Craighead, "Virus detection using nanoelectromechanical devices," *Applied Physics Letters*, vol. 85, no. 13, p. 2604, 2004.
- [98] E. Buks and B. Yurke, "Mass Detection with Nonlinear Nanomechanical Resonator," *Physical Review E*, vol. 74, no. 4, pp. 1–9, 2006.
- [99] C.-y. Nam, P. Jaroenapibal, D. Tham, D. E. Luzzi, S. Evoy, and J. E. Fischer, "Diameter-Dependent Electromechanical Properties of GaN Nanowires," *Nano*, no. 001, 2006.
- [100] C. Li and T.-W. Chou, "Mass detection using carbon nanotube-based nanomechanical resonators," *Applied Physics Letters*, vol. 84, no. 25, p. 5246, 2004.
- [101] A. K. Pandey, O. Gottlieb, O. Shtempluck, and E. Buks, "Performance of an AuPd micromechanical resonator as a temperature sensor," *Applied Physics Letters*, vol. 96, no. 20, p. 203105, 2010.
- [102] S. S. Hullavarad, R. D. Vispute, B. Nagaraj, V. N. Kulkarni, S. Dhar, T. Venkatesan, K. A. Jones, M. Derenge, T. Zheleva, M. H. Ervin, A. Lelis, C. J. Scozzie, D. Habersat, A. E. Wickenden, L. J. Currano, and M. Dubey, "Advances in Pulsed-Laser-Deposited AlN Thin Films for High-Temperature Capping , Device Passivation , and Piezoelectric-Based RF MEMS / NEMS Resonator Applications," *Thin Films*, vol. 35, no. 4, pp. 777–794, 2006.
- [103] W. Weaver Jr., S. Timoshenko, and D. Young, "Vibration Problems in Engineering," pp. 374 – 376, 1990.
- [104] W. Weaver Jr., S. Timoshenko, and D. Young, "Vibration Problems in Engineering," pp. 336 – 338, 1990.
- [105] M. Belyansky, M. Chace, O. Gluschenkov, J. Kempisty, N. Klymko, A. Madan, A. Mallikarjunan, S. Molis, P. Ronsheim, Y. Wang, D. Yang,

- and Y. Li, “Methods of producing plasma enhanced chemical vapor deposition silicon nitride thin films with high compressive and tensile stress,” *Journal of Vacuum Science Technology A Vacuum Surfaces and Films*, vol. 26, no. 3, p. 517, 2008.
- [106] R. Lifshitz and M. L. Roukes, “Thermoelastic damping in micro- and nanomechanical systems,” *Physical Review B*, vol. 61, no. 8, pp. 5600–5609, 2000.
- [107] K. Jensen, H. Peng, and A. Zettl, *Limits of Nanomechanical Resonators*. IEEE, 2006.
- [108] P. S. Waggoner and H. G. Craighead, “Micro- and nanomechanical sensors for environmental, chemical, and biological detection,” *Lab on a Chip*, vol. 7, no. 10, pp. 1238–1255, 2007.
- [109] K. Y. Yasumura, T. D. Stowe, E. M. Chow, T. Pfafman, T. W. Kenny, B. C. Stipe, and D. Rugar, “Quality factors in micron- and submicron-thick cantilevers,” *Journal Of Microelectromechanical Systems*, vol. 9, no. 1, pp. 117–125, 2000.
- [110] D. M. Photiadis and J. A. Judge, “Attachment losses of high Q oscillators,” *Applied Physics Letters*, vol. 85, no. 3, p. 482, 2004.
- [111] S. Kumar Vashist, “A Review of Microcantilevers for Sensing Applications,” *Journal of N*, vol. 3, no. June, pp. 1–15, 2007.
- [112] V. Cimalla, F. Niebelschutz, K. Tonisch, C. Foerster, K. Brueckner, I. Cimalla, T. Friedrich, J. Pezoldt, R. Stephan, and M. Hein, “Nanoelectromechanical devices for sensing applications,” *Sensors and Actuators B: Chemical*, vol. 126, no. 1, pp. 24–34, 2007.
- [113] X. L. Feng, R. He, P. Yang, and M. L. Roukes, “Very High Frequency Silicon Nanowire Electromechanical Resonators,” *Nano Letters*, vol. 7, no. 7, pp. 1953–1959, 2007.

- [114] T. Thundat, E. a. Wachter, S. L. Sharp, and R. J. Warmack, "Detection of mercury vapor using resonating microcantilevers," *Applied Physics Letters*, vol. 66, no. 13, p. 1695, 1995.
- [115] P. Kapa, L. Pan, A. Bandhanadham, J. Fang, K. Varahramyan, W. Davis, and H.-F. Ji, "Moisture measurement using porous aluminum oxide coated microcantilevers," *Sensors and Actuators B: Chemical*, vol. 134, no. 2, pp. 390–395, 2008.
- [116] Z. Hu, T. Thundat, and R. J. Warmack, "Investigation of adsorption and absorption-induced stresses using microcantilever sensors," *Journal of Applied Physics*, vol. 90, no. 1, p. 427, 2001.
- [117] N. V. Lavrik and P. G. Datskos, "Femtogram mass detection using photothermally actuated nanomechanical resonators," *Applied Physics Letters*, vol. 82, no. 16, p. 2697, 2003.
- [118] P. Datskos, "Detection of 2-mercaptoethanol using gold-coated micromachined cantilevers," *Sensors and Actuators B: Chemical*, vol. 61, no. 1-3, pp. 75–82, 1999.
- [119] H. F. Ji and T. Thundat, "In situ detection of calcium ions with chemically modified microcantilevers.," *Biosensors and Bioelectronics*, vol. 17, no. 4, pp. 337–343, 2002.
- [120] S. Cherian, R. K. Gupta, B. C. Mullin, and T. Thundat, "Detection of heavy metal ions using protein-functionalized microcantilever sensors.," *Biosensors and Bioelectronics*, vol. 19, no. 5, pp. 411–416, 2003.
- [121] L. a. Pinnaduwege, V. Boiadjev, J. E. Hawk, and T. Thundat, "Sensitive detection of plastic explosives with self-assembled monolayer-coated microcantilevers," *Applied Physics Letters*, vol. 83, no. 7, p. 1471, 2003.
- [122] D. Ramos, M. Arroyo-Hernández, E. Gil-Santos, H. D. Tong, C. Van Rijn, M. Calleja, and J. Tamayo, "Arrays of dual nanomechanical res-

- onators for selective biological detection.,” *Analytical Chemistry*, vol. 81, no. 6, pp. 2274–2279, 2009.
- [123] B. Ilic, Y. Yang, K. Aubin, R. Reichenbach, S. Krylov, and H. G. Craighead, “Enumeration of DNA molecules bound to a nanomechanical oscillator.,” *Nano letters*, vol. 5, pp. 925–9, May 2005.
- [124] K. S. Hwang, J. H. Lee, J. Park, D. S. Yoon, J. H. Park, and T. S. Kim, “In-situ quantitative analysis of a prostate-specific antigen (PSA) using a nanomechanical PZT cantilever.,” *Lab on a Chip*, vol. 4, no. 6, pp. 547–552, 2004.
- [125] P. S. Waggoner, M. Varshney, and H. G. Craighead, “Detection of prostate specific antigen with nanomechanical resonators.,” *Lab on a Chip*, vol. 9, no. 21, pp. 3095–3099, 2009.
- [126] B. Ilic, D. Czaplewski, H. G. Craighead, P. Neuzil, C. Campagnolo, and C. Batt, “Mechanical resonant immunospecific biological detector,” *Applied Physics Letters*, vol. 77, no. 3, pp. 450–452, 2000.
- [127] B. Ilic, “Attogram detection using nanoelectromechanical oscillators,” *Journal of Applied Physics*, vol. 95, no. 7, p. 3694, 2004.
- [128] a. Gupta, D. Akin, and R. Bashir, “Single virus particle mass detection using microresonators with nanoscale thickness,” *Applied Physics Letters*, vol. 84, no. 11, p. 1976, 2004.
- [129] P. Lugli, S. Harrer, S. Strobel, F. Brunetti, G. Scarpa, M. Tornow, and G. Abstreiter, “Advances in Nanoimprint Lithography,” *2007 7th IEEE Conference on Nanotechnology (IEEE NANO)*, pp. 1179–1184, Aug. 2007.
- [130] R. Knizikevičius and V. Kopustinskas, “Anisotropic etching of silicon in SF<sub>6</sub> plasma,” *Vacuum*, vol. 77, no. 1, pp. 1–4, 2004.

- [131] S. Zankovych, T. Hoffmann, J. Seekamp, J.-U. Burch, and C. M. Sotomayor Torres, "Nanoimprint lithography : challenges and," *Materials Science*, vol. 91, 2001.
- [132] S.-q. X. I, B.-r. Lui, W. I, R. Yangi, Y. Chenz, X.-p. Qui, and R. L. I, "Development of novel SU-8 based nanoimprint lithography," *Technology*, pp. 2008–2011, 2008.
- [133] G. Description, "Thermoplastic Polymers for Nanoimprint Lithography," 2010.
- [134] Z. Hu, T. Seeley, S. Kossek, and T. G. Thundat, "Calibration of optical cantilever deflection readers," *Review of Scientific Instruments*, vol. 75, no. 2, p. 400, 2004.
- [135] K. a. Marx, "Quartz crystal microbalance: a useful tool for studying thin polymer films and complex biomolecular systems at the solution-surface interface.," *Biomacromolecules*, vol. 4, no. 5, pp. 1099–120, 2003.
- [136] D. Shankaran, K. Gobi, and N. Miura, "Recent advancements in surface plasmon resonance immunosensors for detection of small molecules of biomedical, food and environmental interest," *Sensors and Actuators B: Chemical*, vol. 121, no. 1, pp. 158–177, 2007.
- [137] K. Reimhult, K. Yoshimatsu, K. Risveden, S. Chen, L. Ye, and A. Krozer, "Characterization of QCM sensor surfaces coated with molecularly imprinted nanoparticles.," *Biosensors and Bioelectronics*, vol. 23, no. 12, pp. 1908–14, 2008.
- [138] J.-F. Masson, T. M. Battaglia, Y.-C. Kim, A. Prakash, S. Beaudoin, and K. S. Booksh, "Preparation of analyte-sensitive polymeric supports for biochemical sensors.," *Talanta*, vol. 64, no. 3, pp. 716–725, 2004.
- [139] K. V. Gobi, K. Matsumoto, K. Toko, H. Ikezaki, and N. Miura, "Enhanced sensitivity of self-assembled-monolayer-based SPR immunosensor for detection of benzaldehyde using a single-step multi-sandwich im-

- monoassay.," *Analytical and Bioanalytical Chemistry*, vol. 387, no. 8, pp. 2727–2735, 2007.
- [140] M. Tominaga, A. Ohira, Y. Yamaguchi, and M. Kunitake, "Electrochemical, AFM and QCM studies on ferritin immobilized onto a self-assembled monolayer-modified gold electrode," *Journal of Electroanalytical Chemistry*, vol. 566, no. 2, pp. 323–329, 2010.
- [141] D. R. Reyes, D. Iossifidis, P.-A. Auroux, and A. Manz, "Micro total analysis systems. 1. Introduction, theory, and technology.," *Analytical Chemistry*, vol. 74, no. 12, pp. 2623–2636, 2002.
- [142] S. K. Yoo, J. H. Lee, S.-S. Yun, M. B. Gu, and J. H. Lee, "Fabrication of a bio-MEMS based cell-chip for toxicity monitoring.," *Biosensors and Bioelectronics*, vol. 22, no. 8, pp. 1586–1592, 2007.
- [143] A. Ulman, "Formation and Structure of Self-Assembled Monolayers.," *Chemical Reviews*, vol. 96, no. 4, pp. 1533–1554, 1996.
- [144] S. Ferretti, S. Paynter, D. A. Russell, K. E. Sapsford, and D. J. Richardson, "Self-assembled monolayers: a versatile tool for the formulation of bio-surfaces," *Trends in Analytical Chemistry*, vol. 19, no. 9, pp. 530–540, 2000.
- [145] R. K. Smith, P. A. Lewis, and P. S. Weiss, "Patterning self-assembled monolayers," *Progress in Surface Science*, vol. 75, no. 1-2, pp. 1–68, 2004.
- [146] J. C. Love, L. A. Estroff, J. K. Kriebel, R. G. Nuzzo, and G. M. Whitesides, "Self-assembled monolayers of thiolates on metals as a form of nanotechnology.," *Chemical Reviews*, vol. 105, no. 4, pp. 1103–1169, 2005.
- [147] S. Susmel, C. O'Sullivan, and G. Guilbault, "Human cytomegalovirus detection by a quartz crystal microbalance immunosensor.," *Enzyme and Microbial Technology*, vol. 27, no. 9, pp. 639–645, 2000.

- [148] R. Sandberg, K. Mø lhave, A. Boisen, and W. Svendsen, “Effect of gold coating on the Q -factor of a resonant cantilever,” *Journal of Micromechanics and Microengineering*, vol. 15, no. 12, pp. 2249–2253, 2005.
- [149] S. F. Thames and K. G. Panjnani, “Organosilane polymer chemistry: A review,” *Journal of Inorganic and Organometallic Polymers*, vol. 6, no. 2, pp. 59–94, 1996.
- [150] M. Suter, J. Cazin, J. E. Butler, and D. M. Mock, “Isolation and characterization of highly purified streptavidin obtained in a two-step purification procedure from *Streptomyces avidinii* grown in a synthetic medium.,” *Journal of Immunological Methods*, vol. 113, no. 1, pp. 83–91, 1988.
- [151] W. Shu, E. D. Laue, and A. A. Seshia, “Investigation of biotin-streptavidin binding interactions using microcantilever sensors.,” *Biosensors and Bioelectronics*, vol. 22, no. 9-10, pp. 2003–2009, 2007.
- [152] A. Holmberg, A. Blomstergren, O. Nord, M. Lukacs, and J. Lundeberg, “The biotin-streptavidin interaction can be reversibly broken using water at elevated temperatures,” *Analysis*, pp. 501–510, 2005.
- [153] S. S. Verbridge, J. M. Parpia, R. B. Reichenbach, L. M. Bellan, and H. G. Craighead, “High quality factor resonance at room temperature with nanostrings under high tensile stress,” *Journal of Applied Physics*, vol. 99, no. 12, p. 124304, 2006.
- [154] W. H. Chuang, T. Luger, R. K. Fettig, and R. Ghodssi, “Mechanical Property Characterization of LPCVD Silicon Nitride Thin Films at Cryogenic Temperatures,” *Journal Of Microelectromechanical Systems*, vol. 13, no. 5, pp. 870–879, 2004.
- [155] B. Zink, “Specific heat and thermal conductivity of low-stress amorphous SiN membranes,” *Solid State Communications*, vol. 129, no. 3, pp. 199–204, 2004.

- [156] S. S. Verbridge, H. G. Craighead, and J. M. Parpia, “A megahertz nanomechanical resonator with room temperature quality factor over a million,” *Applied Physics Letters*, vol. 92, no. 1, p. 013112, 2008.
- [157] R. A. Buser and N. F. De Rooij, “Very high Q-factor resonators in monocrystalline silicon,” *Sensors and Actuators A: Physical*, vol. 21, no. 1-3, pp. 323–327, 1990.
- [158] O. Hahtela, N. Chekurov, and I. Tittonen, “Non-tilting out-of-plane mode high- Q mechanical silicon oscillator,” *Journal of Micromechanics and Microengineering*, vol. 15, no. 10, pp. 1848–1853, 2005.
- [159] L. M. Fischer, *Development of Silicon Carbonitride Nanomechanical Resonators for Biological Detection Applications*. Master’s thesis, University of Alberta, 2007.